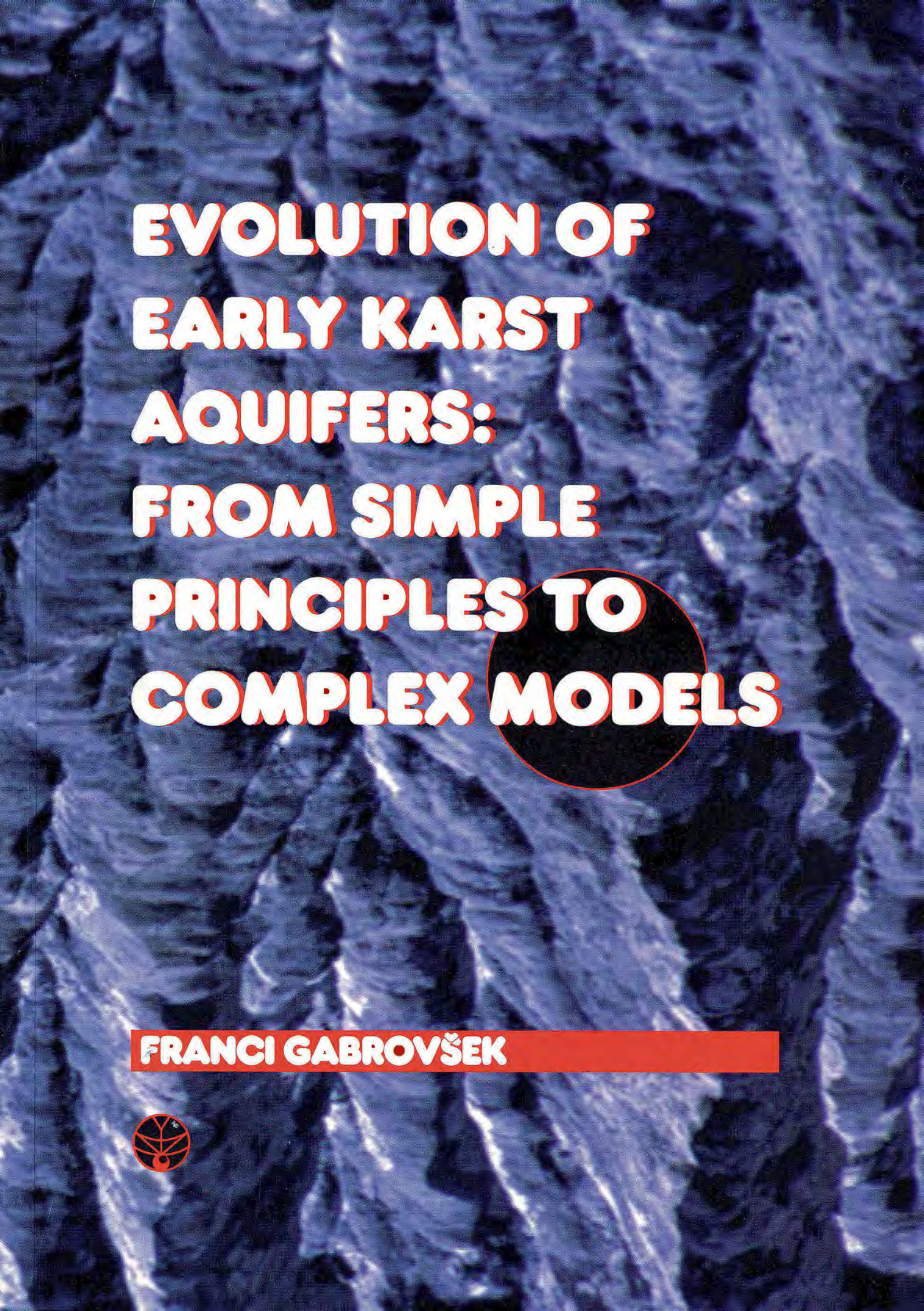
EVOLUTION OF EARLY KARST AQUIFERS: FROM SIMPLE PRINCIPLES TO COMPLEX MODELS
FRANCI GABROVŠEK

Franci Gabrovšek is a researcher at the Karst Research Institute of the Scientific Research Centre of the Slovenian Academy of Sciences and Arts. He graduated at the Department of Physics of the University of Ljubljana in 1995. In 1996 he joined the Karst Research Institute where he worked on several research projects in Slovenia and China.

In March 1997 he joined the group of Prof. Dr. Wolfgang Dreybrodt at the Department of Experimental Physics of the University of Bremen as a doctoral student. There he defended his doctoral dissertation which is presented in this book. His main research interest is the physical and chemical background of the basic karst processes and

Franci Gabrovšek je raziskovalec na Inštitutu za raziskovanje krasa ZRC SAZU. Leta 1995 je diplomiral na oddelku za fiziko Univerze v Ljubljani. Na Inštitutu za raziskovanje krasa se je zaposlil leta 1996. Sodeloval je pri različnih raziskovalnih projektih v Sloveniji in na Kitajskem. Marca 1997 je na Oddelku za fiziko Univerze v Brmenu pričel z doktorskim študijem pod mentorstvom Prof. Dr. Wolfganga Dreybrodta. Tam je v marcu 2000 ubranil doktorsko disertacijo, ki je predstavljena v pričujoči knjigi. Raziskovalno se še naprej ukvarja s fizikalno-kemičnimi osnovami in dinamiko procesov na krasu. Kot jamar sodeluje pri raziskavah velikih jamskih sistemov v slovenskem alpskem krasu.

ZALOŽBA
ZRC

Franci Gabrovšek
Evolution of Early Karst Aquifers: From simple principles to complex models

Uredil/Edited by
Franci Gabrovšek

Oblikovanje/Graphic art and design
Milojka Žalik Huzjan

Izdal in založil/Published by
Inštitut za raziskovanje krasa ZRC SAZU, Založba ZRC

Zanj/Represented by
Tadej Slabe, Oto Luthar

Tisk/Print by
Littera picta, Ljubljana

Izdajo je finančno podprlo/The publication was financialy supported by
Ministrstvo za znanost in tehnologijo/
Ministry of Science and Technology of the Republic of Slovenia

https://doi.org/10.3986/9616358138

CIP - Kataložni zapis o publikaciji
Narodna in univerzitetna knjižnica, Ljubljana

556.3(043.3)
551.44(043.3)

GABROVŠEK, Franci
Evolution of early karst aquifers : from simple principles to complex models / Franci Gabrovšek. - [Postojna] ; Inštitut za raziskovanje krasa ZRC SAZU, Založba ZRC, 2000

ISBN 961-6358-13-8

A dissertation for the degree of Doctor of Natural Science
(Dr.rer.nat) at the Department of Physics/Electrotechnics
University of Bremen
(March 2000)

Acknowledgments

The pathways in the evolving karst aquifers and the pathway leading to this work have a lot in common. They are complex, hard to predict and influenced by many parameters. Behind the parameters of my own pathway there are people and institutions who have contributed directly or indirectly to this work.

The supervising of Prof. Dr. Wolfgang Dreybrodt comprised inspiring daily discussions, flow of ideas, passing the scientific enthusiasm to me and help with all the formalities and problems that a doctoral student meets. The German vocabulary uses a word "Doktorvater" which perfectly describes the role of Prof. Dreybrodt during my last three years.

Thanks to Dr. Tadej Slabe from the Karst Research Institute for seeing a perspectives for a physicist in karstology and supporting my efforts to find a way in this field.

Thanks to the colleagues at the Karst Research Institute in Postojna and at the University of Bremen for a nice working atmosphere, fruitful discussions about all aspects of life (including karst) and for a support at all instances.

Thanks to Nataša. Caves are probably not her favourite environment, neither is physics..., two more reasons to admire her full support and understanding. My parents have been there for me for the last 30+ years (and it was not always easy). Hvala, Nada and France.

My work and staying in Bremen were supported by the Ministry of Science and Technology of the Republic of Slovenia and the University of Bremen. Thanks to both of them.

Publication of the monography was financially supported by the Ministry of Science and technology of the Republic of Slovenia.

A special thanks to the cavers from the Ljubljana caving club. There it has all started.

Evolution of Early Karst Aquifers: From simple principles to complex models

Franci Gabrovšek

Ljubljana 2000

Contents

1 INTRODUCTION

1.1 KARST: UNDERSTANDING IT AND THE AIM OF THIS WORK

Karst[1] is a typical landscape on soluble rocks with a distinctive hydrology, unique landforms and fantastic underground features which attract people to observe and study it. The longest cave systems reach beyond 500km, the deepest approach a vertical distance of 2km ($> 1.6km$ at the time of writing) between their highest and lowest points. A mature karst landscape is characterised by the absence of surface flow. Karst surface covers about 10%-20% of the Earth's land ice-free area (Ford and Williams, 1989).

Study of karst is not only important for its unique features, it has also practical importance: **about 25% of the world population drinks water from karst aquifers (Ford and Williams, 1989).** One should not forget that the fresh water supply is expected to be one of our mayor problems in this century.

The facts quoted above should be sufficient to justify this work which deals with the early evolution of karst.

The main process rendering karst unique is the dissolution of bedrock by water. The most common types of karst rocks are sedimentary carbonates, limestone and dolomite. Gypsum, anhydrite, salt and quartzite karst areas are also known around the world. Typical karst rocks have a low primary porosity, but attain a considerable secondary porosity during the karst evolution.

Most karst features owe their origin to the subsurface drainage of water in karst aquifers. The question how do karst aquifers evolve in time and consequently how do caves develop, has puzzled scientists and observers for a long time. And it still does.

To understand karst and its evolution one has to study and understand the basic processes behind it. Basically there are two approaches to this:

- **Large to small scale, empirical approach** which describes the basic processes mainly due to the observation of the whole.

[1] As a Slovenian I must point out that the term karst originates from the Slovenian region Kras, where these phenomena were objects of scientific studies for the first time.

- **Small to large scale, analytical approach** builds complex systems with simple elements based on the basic principles of physics and chemistry.

Neither is good alone. The empirical approach normally leads to wrong conclusions because the general picture is too complex. The analytical approach uses an extremely simplified model of reality and neglects many parameters which can be important. One or the other concept remains just a concept or a hypotheses if the two do not meet. Once both ways unite a good theory might appear.

The idea of this work is to contribute a few building blocks to the bridge between the empirical and analytical concepts from the side of the analytical approach.

1.2 A KARST AQUIFER AND ITS PROPERTIES

Before we give a review on speleogenetic[2] ideas, we define "our playground": **a karst aquifer**. The term aquifer defines a rock body sufficiently permeable to transmit groundwater (Bear and Verruijt, 1987). What makes karst aquifers specific is that their transmissivity and storage are increasing in time by bedrock dissolution. Typical karst aquifers exhibit a small primary porosity, but attain high secondary porosity due to the circulation of water which dissolves bedrock. In the initial state of a karst aquifer flow of water is limited to fractures and bedding planes. Our study will deal with flow systems which owe their origin to meteoric water circulating within the massif of limestone or other soluble rocks. This way the so-called "common caves" (Ford and Williams, 1989) are formed. In most of the following discussion, we assume limestone fractured aquifers.

Pure water cannot dissolve much limestone. Already in the 18^{th} century it was well accepted that water containing CO_2 is the aggressive agent in karst. Only atmospheric CO_2 was considered at that time. This way the $CO_2 - H_2O$ solutions cannot dissolve much limestone, since the CO_2 represents only about 0.03% of the atmosphere. Later Swinnerton (1932) stressed the importance of soil CO_2. The CO_2 content in the soil "atmosphere" is often above 5% (Ford and Williams, 1989).

Mature karst aquifers exhibit an extreme heterogeneity of hydraulic conductivities. They range from $10^{-10}\,m/s$ up to $10^{-1}\,m/s$ (Worthington, 1999; Halihan et al., 1999). The lowest conductivity is due to the intergranular porosity of the rock matrix, the highest is from the large cave conduits. Therefore the nature of water flow in karst aquifers can be of any type: from laminar (Darcian) to turbulent flow in filled or open channels.

[2]Note that speleogenesis (cave formation) is a part of the "evolution of karst aquifers".

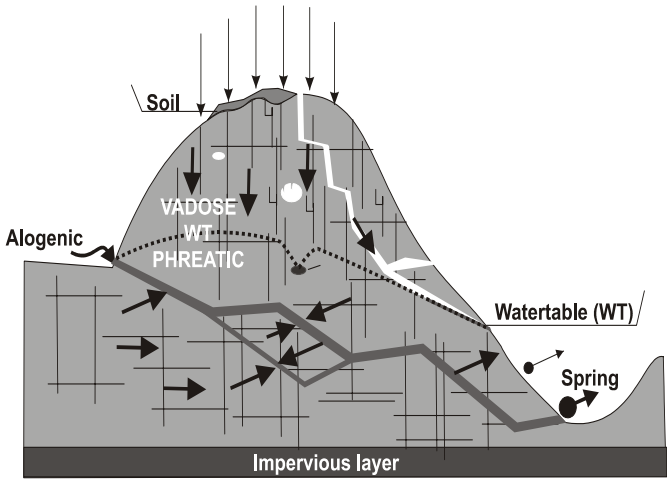

Figure 1.1: A simple conceptual model of a karst hydrological system with its elements and flow systems.

The key question of speleogenesis is how does this secondary porosity evolve? How does a relatively homogeneous aquifer characterised by rock matrix, fractures and bedding planes with aperture widths less than $10^{-2}\,cm$ evolve to such a complex structure like extensive cave systems?

1.3 CONCEPTUAL MODELS OF CAVE DEVELOPMENT IN KARST AQUIFERS

In the 18th and 19th (Ford and Williams, 1989) century big steps were taken once the importance of chemical denudation was stressed and basic equations on fluid flow in porous and fractured rock aquifers were given.

Most of the modern concepts of speleogenesis were put forward between 1900 and 1950. The theories were rather conflicting, since each of them was based on a specific location and tried to be generalised. Three hypotheses were accepted at that time (Ford and Williams, 1989).

1. Vadose hypothesis implies that caves were excavated by open channel cave streams in the vadose zone.
2. Deep phreatic hypothesis assumes that caves develop deep below the water-table in the phreatic zone.
3. Water-table hypotheses (Swinnerton, 1932; Rhoades and Sinacori, 1941) is based on the fact that most of the water movement is along the water-table at the top of the phreatic zone. Therefore, the caves develop there. See Fig.1.2.

Each of these hypothesis was at least partially right. Evidences all around the globe supported them, but none was generally valid. Ford and Ewers (1978) linked these hypotheses into one genetic theory. They proposed a four-state model in which deep phreatic and water-table caves are the end members. In their model the fissure frequency determines what kind of cave develops. See Fig.1.2.

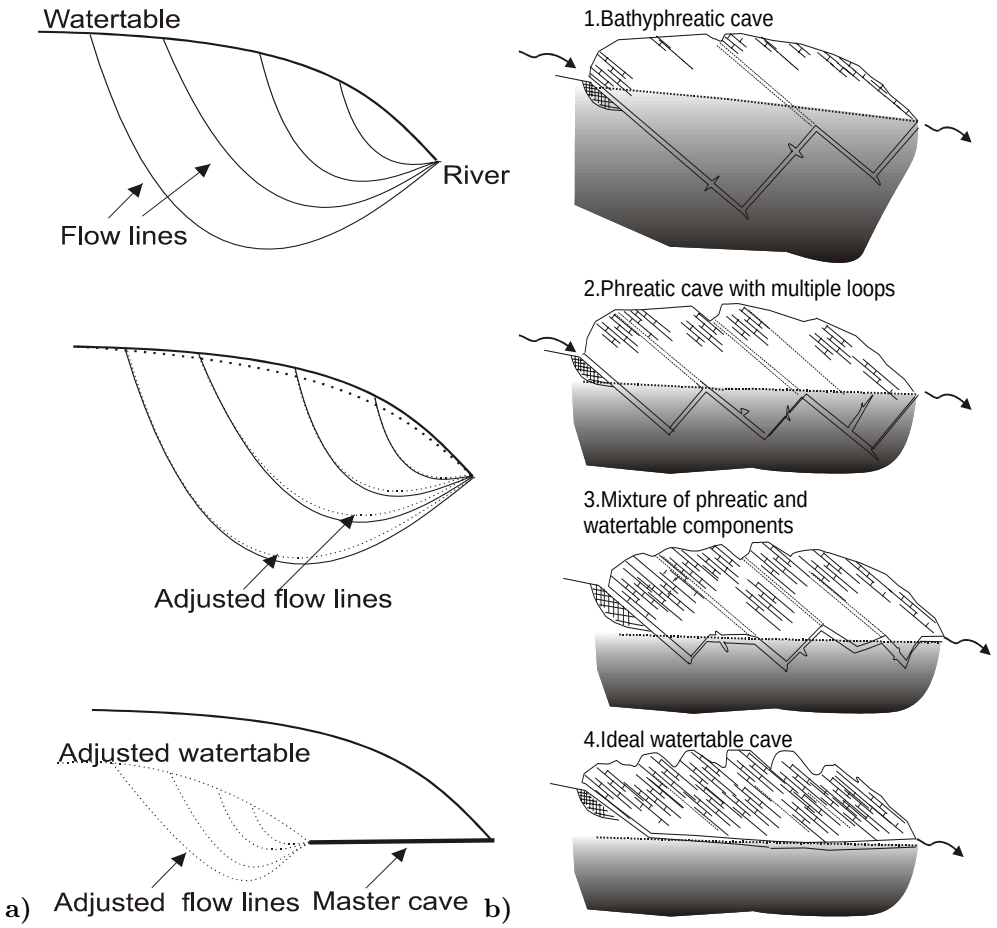

Figure 1.2: **a)** The water-table cave hypothesis proposed by Swinnerton (1932). **b)** Ford and Ewers's (1978) four-state model. Depending on the fissure frequency various types of caves evolve: When fissure frequency is low, bathyphreatic caves (state 1) evolve. With increasing fissure frequency the number of phreatic loops increases (states 2 and 3). High fissure frequency results in the evolution of water-table caves. Extremely low or extremely high fissure frequency do not allow evolution of caves (states 0 and 5, not shown here). Both figures are taken from Ford (1999).

1.4 MODELS DERIVED FROM BASIC PRINCIPLES OF PHYSICS AND CHEMISTRY

The basic knowledge of the properties of karst aquifers and of dissolution kinetics of limestone, as well as access to computational power, enabled another approach towards understanding of the evolution of karst aquifer.

Starting from the basic principles of groundwater chemistry and hydrology and applying parameters and boundary conditions typical for karst, the first numerical models were presented in the late 1980s by Dreybrodt (1990) and Palmer (1991). They presented the evolution of a basic building block of karst aquifers: a single fracture.

Later Lauritzen et all. (1992) and Howard and Groves (1994a; 1994b) presented a model of speleogenesis on two dimensional networks. A further step was made by Siemers and Dreybrodt (1998; 1998; 2000) who presented the evolution of 2D percolation networks and implied various lithological and hydraulic conditions. They also presented the evolution of 2D networks in the vicinity of hydraulic structures; this is the case where the potential of numerical models is of great practical importance.

Recently Clemens et all. (1997a; 1997b; 1999) used a double porosity model to couple the conduit flow with the flow in the surrounding continuum and to calculate the evolution of conduits under constant recharge conditions.

A similar approach was made by Kaufmann and Brown (1999a; 1999b) who simulated the double porosity by incorporating the prominent fractures directly into continuum.

THE CONCEPT OF THIS WORK AND THE PHILOSOPHY BEHIND IT

There are several ways to build up numerical models (of karst aquifer evolution). The first type, let us name them "application oriented", can be a three-dimensional model of an aquifer with multiple porosity and complex boundary conditions applied to it. Such models can be developed nowadays but their interpretation can be as hard as the interpretation of observations in nature. Of course in the model one can envisage many different scenarios and play with the parameters much easier than nature does. Anyway the traps are similar to those in the empirical approach.

What we are after are the basic processes and mechanisms. Therefore we employ the "processes oriented models" and start with the simplest elements of karst aquifers, simplified equations, and build more complex models gradually, not adding another parameter before the effects of all the old ones are fully exploited. This approach is of course time consuming, since the addition of any parameter demands the analyses of its correlation

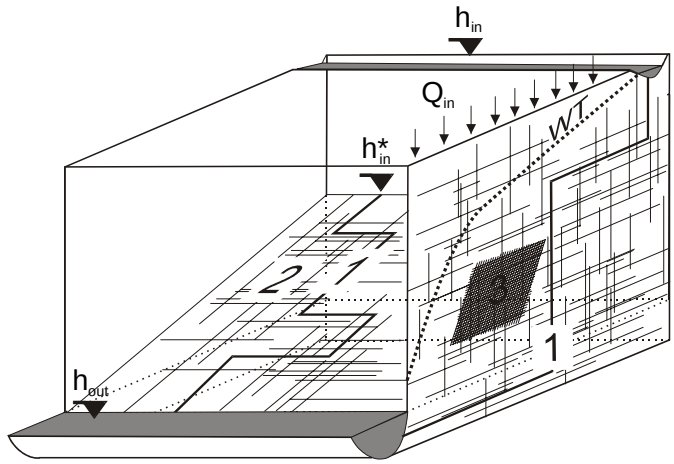

Figure 1.3: The elements of a karst aquifer discussed in this work. **1:** A single fracture under constant head conditions. **2:** 2D fracture network under constant head conditions. **3:** Vertical section of an unconfined aquifer with a constant recharge and constant head conditions applied to it. As shown, a dense network of fine fractures and a coarse network of prominent fractures are superimposed to simulate the multiple porosity character of karst aquifers. The thick dashed line WT represents the position of the water-table. The hydraulic heads at the inputs and outputs are denoted as h_{in}, h^*_{in} and h_{out}.

with all the parameters used before. But according to our experience, one can easily misinterprete the results of more complex models without a deep understanding of simpler ones. The final goal is to make an "application oriented" model and to fully understand its results.

The path of this work starts with simple models and takes us towards more complex ones. It resembles the historical development of the models presented so far. Especially in the simple systems our approach will be partially analytical, i.e. we will try to make analytical approximations to elucidate the obtained numerical results. This way we gain a deeper understanding of the models and more general results.

Fig.1.3 schematically presents the approach we take. In Chap.3 the evolution of a single fracture as a basic element of karst aquifers is discussed. It reviews some of the work presented so far from analytical point of view and introduces new geochemical conditions and hydrological conditions.

Chap.4 discusses the evolution of 2D networks under constant head conditions. We could also define it as the evolution in length and breadth as used by Ford and Ewers (1982; 1989). The presented models correspond to the other 2D models (Siemers and Dreybrodt, 1998). New parameters are added by introducing various geochemical conditions.

Chap.5 presents the evolution of a karst aquifer in length and depth. It somehow resembles the empirical theories of cave genesis quoted above. This is also the most comprehensive model that we will present and is our closest approach to nature.

The mathematics used for the analytical approximation consists mostly of basic calculus and should not distract one from reading the work. The number of cases which we handle analytically drops with the complexity of the model.

2 EQUILIBRIUM CHEMISTRY AND DISSOLUTION RATES OF LIMESTONE IN $H_2O - CO_2$ SOLUTIONS

The understanding of chemical processes is the key for understanding early karst evolution. This chapter gives a quick review on this. To model karst evolution we need to know the dissolution rates of limestone in karst environments. These are a function of the undersaturation of the solution, and therefore knowledge of equilibrium chemistry is required. The first part of this chapter focuses on equilibrium chemistry of the $H_2O - CO_2 - CaCO_3$ system, the second on its chemical kinetics. One has to be aware that the knowledge of equilibrium chemistry alone is not enough to model and understand early karstification. As mentioned in the introduction we only regard the action of $CO_2 - H_2O$ solutions. Note that karstification of limestone might also be caused by other aggressive solutions, such as sulphuric acid in the case of hypogenic karst (Ford and Williams, 1989). These processes will not be discussed in this work.

For further reading on equilibrium chemistry and limestone dissolution rates in karst environments the reader is referred to (Dreybrodt, 1988, 1997; Dreybrodt and Eisenlohr, 2000; Dreybrodt, 2000).

2.1 EQUILIBRIUM CHEMISTRY OF $H_2O - CO_2 - CaCO_3$ SYSTEM

The equilibrium chemistry of the $CaCO_3 - H_2O - CO_2$ system is well known and discussed in the literature (see (Dreybrodt, 1988, 2000) for more details). As mentioned, the most common aggressive agent in karst is CO_2 rich water which percolates through the limestone massif, thus we first focus on pure $CO_2 - H_2O$ solution.

Carbon dioxide dissolves in water. The p_{CO_2} of the surrounding atmo-

sphere and the activity of dissolved CO_2 are related by Henry's law

$$(CO_2^{aq}) = K_H p_{CO_2}. \tag{2.1}$$

K_H is the Henry's constant which is temperature dependent; at $10°C$ $\log(K_H)$ is about -1.27.

CO_2 reacts with water to form H_2CO_3. This dissociates in steps to $H^+ + HCO_3^-$ and further to $H^+ + CO_3^{2-}$. The dissociation steps are governed by mass action law with mass action constants K_1 and K_2 for each step respectively.

The saturation state of the solution with respect to $CaCO_3$ is defined by

$$\Omega = \frac{(Ca^{2+})(CO_3^{2-})}{K_c}, \tag{2.2}$$

where

$$K_c = (Ca^{2+})_{eq}(CO_3^{2-})_{eq}. \tag{2.3}$$

The subscript eq denotes the state of equilibrium and K_c is the solubility constant. Round brackets denote the activity of ionic species. At $10°C$ the logarithm of K_c is -8.41.

Protons produced by dissociation of H_2CO_3 react with carbonate ions released from the mineral:

$$CO_3^{2-} + H^+ \rightarrow HCO_3^-. \tag{2.4}$$

This reaction keeps the ion activity product $(Ca^{2+})(CO_3^{2-})$ sufficiently low and enables the dissolution of calcitep.

The reaction mechanisms at the calcitep surface in the presence of carbonic acid were first described by Plummer et al. (1978). They proposed three surface reactions which can be summarised by the following overall reaction:

$$CaCO_3 + CO_2 + H_2O \rightarrow Ca^{2+} + 2HCO_3^-. \tag{2.5}$$

From Eq.2.5 an important conclusion follows: for each Ca^{2+} ion that enters the solution one molecule of CO_2 is consumed and converted into HCO_3^- .

Further derivation of equilibrium equations will be omitted here and only results important for the following chapters will be presented. For details the reader is referred to (Dreybrodt, 1988).

The basic result of the equilibrium chemistry is the equation describing the equilibrium concentration of Ca^{2+} as a function of[1] p_{CO_2} :

$$[Ca^{2+}]_{eq} = \left(p_{CO_2} \cdot \frac{K_1 K_2 K_H}{4 K_2 \gamma_{Ca} \gamma_{HCO_3}} \right)^{1/3}. \tag{2.6}$$

γ_{Ca} and γ_{HCO_3} are the activity coefficients of Ca^{2+} and HCO_3^- at equilibrium. K_1 and K_2 are the mass action constants for the both dissociation steps.

[1]The equation given is obtained by using the approximation $2[Ca^{2+}] = [HCO_3^-]$. Otherwise a numerical procedure is required to obtain the solution.

BOUNDARY CONDITIONS FOR ACHIEVING EQUILIBRIUM

Dissolution of calcite by CO_2 containing water proceeds under various boundary conditions:

- **Open system conditions:** the solution is in contact with limestone and a CO_2 containing gas phase. The flux of CO_2 between the liquid-gas interface replaces the CO_2 consumed by dissolution of calcite.
- **Closed system conditions:** there is no interface between an atmosphere and the solution. CO_2 consumed by dissolution of calcite is not replaced, therefore its concentration decreases with increasing Ca^{2+} concentration.

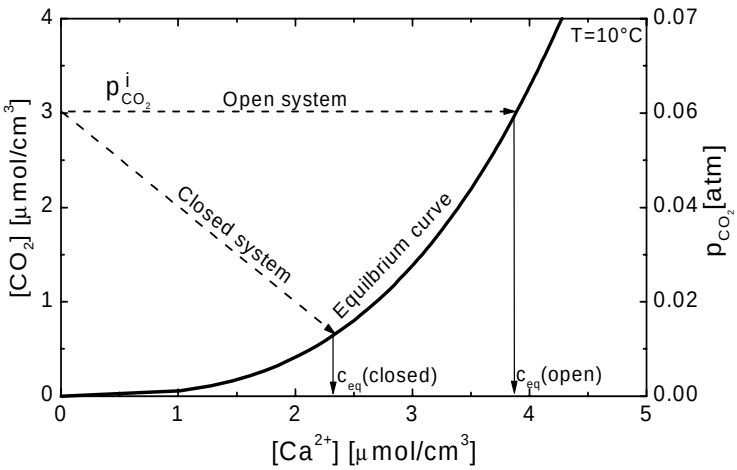

Figure 2.1: Chemical pathways of the solutions in the open and closed system. The thick line represents the $CO_2 - Ca^{2+}$ equilibrium curve as given in Eq.2.6. Dashed lines represent the pathway of solutions in the open and closed system. In the case of a closed system one CO_2 molecule is consumed for each Ca^{2+} ion entering the solution. At the cross-sections between the pathways and equilibrium curves, the equilibrium concentration can be read. The thin solid lines point to the calcium equilibrium concentration.

For the open system the equilibrium concentration is given by Eq.2.6. In the phreatic zone of karst aquifer which is the domain of our models, dissolution proceeds under closed system conditions. In this case one has to consider that p_{CO_2} in the solution decreases as dissolution proceeds. Thus Eq.2.6 cannot be directly applied. If $p^i_{CO_2}$ is the partial pressure of CO_2 prior to any dissolution of calcite, than the p_{CO_2} at the closed system equilibrium is given by:

$$p_{CO_2} \approx p^i_{CO_2} - \frac{[Ca^{2+}]_{eq}}{K_H}. \tag{2.7}$$

Inserting this into Eq.2.6 a cubic equation for $[Ca^{2+}]_{eq}$ is obtained. Its solution gives the $[Ca^{2+}]_{eq}$ for the closed system.

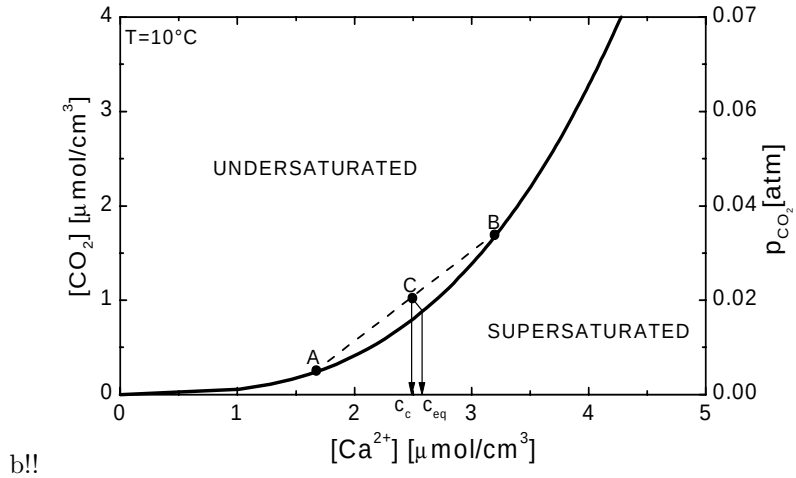

b!!

Figure 2.2: Equilibrium curve and the regions of supersturated and undersaturated solutions. Mixing of saturated solutions A and B, produces an undersaturated solution C. The arrows point to the calcium concentration of solution C and its equilibrium calcium concentration. See text for details.

See (Dreybrodt, 1988) for the intermediate cases where the solution is in contact with a limited amount of CO_2 rich gas and for the cases where boundary conditions change during dissolution.

Fig.2.1 shows the pathways of the solution when dissolving under open and closed system conditions. The thick solid line represents the equilibrium curve as given by Eq.2.6. The dashed lines show the pathways of the solutions in open and closed system as denoted. The intersections between dashed lines and equilibrium curve are the equilibrium points. The solid arrows point to the equilibrium Ca^{2+} concentration for the open and closed system, respectively.

MIXING OF SATURATED SOLUTIONS IN THE CLOSED SYSTEM

The non-linearity of the $CO_2 - Ca^{2+}$ equilibrium curve has an important consequence shown in Fig.2.2. The equilibrium curve divides the regions of undersaturated and supersaturated solutions. If the $([CO_2], [Ca^{2+}])$ coordinate of the solution is above the equilibrium curve it is undersaturated, if it is below, the solution is supersaturated. For convenience, to avoid to many brackets, we will write (CO_2, Ca^{2+}) instead of $([CO_2], [Ca^{2+}])$. Fig.2.2 shows the mixing of two solutions A and B, saturated with respect to calcite. The (CO_2, Ca^{2+}) pair of the resulting solution C is on the line connecting A and B and is in the undersaturated region due to the non-linearity of the equilibrium curve. The arrows point to the Ca^{2+} concentration c_C of the mixed solution C and its equilibrium concentration

c_{eq}. The importance of this phenomenon to the karst evolution was stressed by Bögli (1964). "Mischungkorrosion"[2] is not a crucial cave forming mechanism, although it enhances early karst evolution as presented recently by Gabrovšek and Dreybrodt (1999b). This is discussed in Sec.3.5.

2.2 CHEMICAL KINETICS OF THE $H_2O - CO_2 - CaCO_3$ SYSTEM

So far we discussed the chemical pathways of karst waters with respect to Ca^{2+} and CO_2. The question remains, how fast do the solutions "move" along these pathways in karst environments.

The knowledge of the chemical kinetics of limestone is crucial to gauge the models presented in the following sections. How fast $CaCO_3$ is removed from the surface of the mineral depends on three mutually-operating rate controlling mechanisms:

- The surface reaction, which depends on the chemical composition of the solution at the mineral surface and on the concentration of impurities in the mineral.
- The diffusional flux of ions released from the mineral surface, which depends on the concentration gradient and diffusion constant.
- The conversion of CO_2 into HCO_3^- and H^+. The process can be rate-limiting when the ratio between the volume of the solution and and the reactive surface of the mineral (V/A ratio) is small (Dreybrodt et al., 1996).

Generally, all three mechanisms have to be considered. On the other hand the specific settings can favour one or two mechanisms such that these exhibit much higher rates than the rest. In this case the fast mechanisms can be excluded and the rates can be calculated by considering only slow processes. When only one mechanism is slow we say that the rates are either surface, transport or CO_2 controlled.

SURFACE RATES

The surface rates far from equilibrium are well defined by the Plummer-Wigley-Parkhurst (PWP) equation (Plummer et al., 1978) which relates the rate to the chemical composition of the solution at the surface.

Close to equilibrium natural limestones exhibit much lower rates than predicted by the PWP equation. Based on the experimental data of Plum-

[2] A German expression for mixing corrosion, which is commonly used in literature.

mer et al., Palmer (1984) showed that the surface rates can be described by an empirical rate law given by:

$$F_s(c) = \begin{cases} k_{n_1}(1 - c/c_{eq})^{n_1} & , \quad c \leq c_s \\ k_{n_2}(1 - c/c_{eq})^{n_2} & , \quad c > c_s \end{cases} \tag{2.8}$$

where n_1 is in the range between 1.5 and 2.2, $n_2 \approx 4$ and a switch concentration $c_s \approx 0.8 c_{eq}$. This rate law was experimentally verified for natural calcite by Svensson and Dreybrodt (1992) for the open system and later by Eisenlohr et al. (1997; 1999; 2000) for the closed system. Eisenlohr et al. obtained values of n_2 between 4 and 11. They also showed that the drop of the rates with respect to PWP is due to impurities in natural limestones which accumulate on the surface and inhibit dissolution.

TRANSPORT AND CO_2 CONTROLLED DISSOLUTION

To obtain the actual dissolution rate one has to consider the combined action of surface reaction, diffusion and CO_2 conversion. Buhmann and Dreybrodt (1985a; 1985b) suggested a model for the open and closed system with all three processes involved. They assumed the PWP equation for the surface rates. Their results can be summarised by the following approximation:

$$F(c) = \alpha(c_{eq} - c) = k_1(1 - c/c_{eq}). \tag{2.9}$$

The parameter α depends on the temperature, CO_2 content of the solution, the V/A ratio and the type of flow, i.e. laminar or turbulent (refer to (Dreybrodt, 1988) for more details). Typical values of α are several $10^{-5}\, cm/s$. This was also experimentally verified by Dreybrodt et al.(1996).

2.2.1 THE RATE EQUATION USED IN THE MODELS

In the initial stage of the evolution of a karst aquifer, the water is flowing through fractures with aperture widths between $0.005\, cm$ and $0.1\, cm$. In these conditions, the rate determining mechanisms are transport and CO_2 control if the concentration is below some switch concentration c_s . The rates follow a linear rate law given by Eq. 2.9. The kinetic constant k_1 is almost constant for aperture widths between $0.005\, cm < a < 0.1\, cm$. For larger aperture widths rates are increasingly transport controlled and the rate constant k_1 has to be replaced by (Dreybrodt, 1988):

$$k_D = k_1 \left[1 + \frac{k_1 a}{6 D c_{eq}}\right]^{-1} . \tag{2.10}$$

As the solution approaches equilibrium, the surface rates become rate controlling and the rates follow a non-linear dissolution rate given in Eq.2.8.

Combining Eqs.2.8 and 2.9 one obtains the rate law which will be used throughout this work:

$$F(c) = \begin{cases} k_1(1 - c/c_{eq}) & , \quad c \leq c_s \\ k_n(1 - c/c_{eq})^n & , \quad c > c_s \end{cases} \tag{2.11}$$

where $k_n = k_1(1-c_s/c_{eq})^{1-n}$. Typical values of k_1 are a few $10^{-11}\, mol/cm^2 s$, values of n are between 4 and 11. The switch concentration c_s is between $0.7\, c_{eq}$-$0.9\, c_{eq}$. See also Tab.3.1 for the typical parameters used in the following models.

3 THE EVOLUTION OF A SINGLE FRACTURE

3.1 EVOLUTION UNDER CONSTANT HEAD CONDITIONS: THE FEEDBACK MECHANISM AND BREAKTHROUGH

The evolution of a basic element of a karst aquifer - a single fracture - is of the utmost importance for understanding the evolution of more complex structures like fracture networks. The term "single fracture" in our case does not only imply straight fractures like that in Fig.3.1; a sequence of fractures forming a pathway between input and output can also be discussed in this context (see elements "1" in Fig.1.3).

This chapter presents the evolution of a single fracture in various settings which are implied in physical and chemical parameters used in the presented models. Reaction-transport mechanisms in tubes and fractures are well known and discussed also in the other fields of science (Beek and

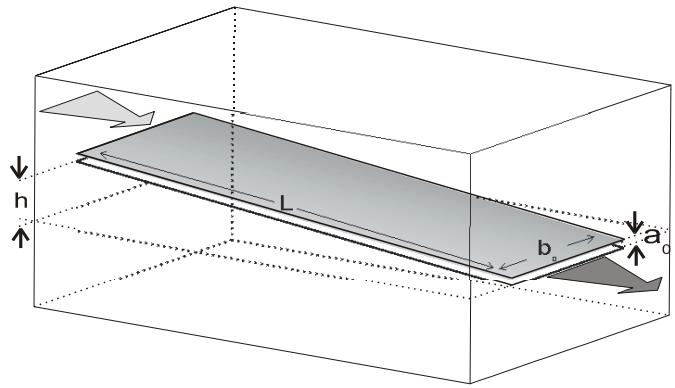

Figure 3.1: Uniform fracture with aperture width a_0, width b_0 and length L. Calcite aggressive water is driven through it by the time-independent hydraulic head h. The goal is to calculate how do the aperture widths and flow rates evolve in time due to the dissolutional widening.

Mutzall, 1975; Bird et al., 1960). Weyl (1958) was the first who applied them to the fractures and tubes in calcite. His experiments and those of Erga and Terjesen (1956) revealed a linear rate law for calcite dissolution in $CO_2 - H_2O - CaCO_3$ solutions. These results caused some trouble to researchers as discussed by White and Longyear (1992), since large conduits in the natural hydrogeochemical conditions do not evolve in geologically relevant timescales if only linear kinetics is operative. Non-linear rate laws as pointed out by White (1977) and Palmer (1984) were first introduced into the model of single fracture evolution by Dreybrodt (1988; 1990) and Palmer (1991). A detailed mathematical analysis of the problem was later done by Dreybrodt (1996) and Dreybrodt and Gabrovšek (2000).

3.1.1 BASIC RELATIONS AND NUMERICAL RESULTS

This section presents the basic mechanisms acting when water driven by a time-independent hydraulic head h flows through an initially uniform fracture in soluble rock . The scenario is shown in Fig.3.1.

The flow rate $Q[cm^3/s]$ depends on the flow resistance R and on the hydraulic head h. The resistance is a function of the fracture aperture width a, fracture width b, fracture length L and the dynamic viscosity of the water η/ρ (η is viscosity in g/cms and ρ is the density in g/cm^3). For laminar flow, the flow rate through the fracture is given by the Hagen-Poisseuille equation (Beek and Mutzall, 1975),

$$Q = h/R = iL/R, \tag{3.1}$$

where i is hydraulic gradient defined as h/L and

$$R = \frac{12\eta}{\rho g} \int_0^L \frac{dx}{a^3(x,t)b(x,t)M(x,t)}. \tag{3.2}$$

M is geometrical factor and depends on the value a/b:

$$M = 0.6 - 0.3a/b \quad \text{elipsoidal shape,} \tag{3.3}$$

$$M = 1 - 0.6a/b \quad \text{rectangular shape.} \tag{3.4}$$

This would be the end of the story if the system were non-reactive. The CO_2 containing water is aggressive with respect to the karst rocks, therefore it widens the fracture by dissolving limestone from the walls.

The widening rate at any point in fracture is proportional to the dissolution rate there. This is given by Eq.2.11 and depends on the undersaturation of the solution. Therefore we need to know the concentration of calcium ions along fracture to calculate its widening in time and space. This can be calculated by coupling the flow and dissolution rates by the mass conservation law. It requires that the amount of calcite dissolved from

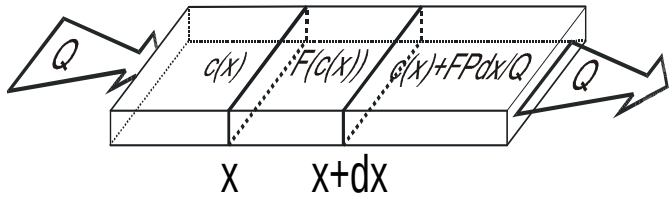

Figure 3.2: Mass conservation in the part of the fracture between x and $x + dx$.

the walls within any part of the fracture (e.g. x and $x + dx$) is equal to the difference between the amount of calcium leaving out and the amount of calcium entering the selected part (c.f. Fig 3.2). Writing this down we obtain

$$F(c(x))P(x)\,dx = v(x)A(x)\,dc = Q dc. \tag{3.5}$$

$v(x)$ is the velocity of the solution at the position x and $A(x)$ the cross-section of the fracture there. In the integral form, taking $c(x = 0) = c_0$, we get:

$$Q\int_{c_0}^{c(x)} \frac{dc}{F(c)} = \int_0^x P(x)\,dx. \tag{3.6}$$

To obtain the dissolution rates along the fracture we have to solve Eqs.3.5 or 3.6. The aperture width $a(x, T)$ at some position x at time T is given by the time integral of the dissolution rate:

$$a(x, T) = 2\gamma \int_0^T F(x, t)\,dt + a_0. \tag{3.7}$$

$F(x, t)$ is obtained from Eq.3.6 and the factor γ (value of γ for the limestone is $1.7 \cdot 10^9$) converts the dissolution rates from mol/cm^2s to the retreat of the wall in $cm/year$.

We cannot obtain a general analytical solution of the Eqs.3.5-3.7. To solve the problem numerically, we discretize time and spatial variables t and x into suitable Δt and Δx increments and do the following procedure:

1. Calculate $Q(t)$ from Eqs. 3.1 and 3.2
2. Calculate $F(x)$ from Eqs. 2.11 and 3.5
3. Calculate the new profile assuming a constant rate in the time interval Δt according to

$$\begin{aligned} a(x, t + \Delta t) &= a(x, t) + 2\gamma F(c(x), t)\Delta t, \\ b(x, t + \Delta t) &= b(x, t) + 2\gamma F(c(x), t)\Delta t. \end{aligned} \tag{3.8}$$

4. If the flow is laminar go back to step 1. If the flow is turbulent, exit.

THE RANGE OF THE PARAMETERS RELEVANT FOR NATURAL KARSTIFICATION

There are two types of parameters defining the evolution of a fracture: physical parameters and chemical parameters. Chemical parameters were discussed in Chap.2. Once we define the geochemical settings at the site of karstification, the values of the chemical parameters can be calculated from thermodynamical data (c_{eq}) or measured in the laboratory (rate law and its constants).

Physical parameters depend on the particular hydrogeological setting in which karstification proceeds. Typical aperture widths of fractures in nature are in the order of several tenths of a millimetre (Motyka and Wilk, 1984; Wilk et al., 1984). In natural systems hydraulic gradients are usually smaller than 0.1. Typical lengths of pathways connecting inputs and outputs are in the order of several hundred metres to several kilometres. In man-made hydraulic conditions, such as at dam sites, hydraulic gradients can be greater than 1 and the lengths of pathways less than 200m.

Although the models of karstification in man-made conditions can be of great practical importance (Palmer, 1988; Dreybrodt, 1990, 1996; Siemers, 1998), we will focus on the natural karstification. Typical values of parameters for natural settings are given in Tab.3.1. This set of parameters will be used throughout this work and referred as a **standard fracture**.

DISCRETISATION OF x AND t

As pointed out by Dreybrodt (1996), discretisation of the spatial variable x has to be done with care. The change of concentration Δc within the

Name	Sign	Standard value	Units
Initial aperture width	a_0	0.02	cm
Initial width	b_0	100	cm
Length	L	10^5	cm
Hydraulic head	h	$5 \cdot 10^3$	cm
Ca^{2+} equilibrium concentration	c_{eq}	$2 \cdot 10^{-6}$	mol/cm^3
Linear rate constant	k_1	$4 \cdot 10^{-11}$	mol/cm^2s
Non-linear kinetics order	n	4	
Non-linear rate constant	k_n	$4 \cdot 10^{-8}$	mol/cm^2s

Table 3.1: Basic chemical and physical parameters. The "standard" values relevant for natural karstification are given in the third column. These values will be used in the following model runs when not noted otherwise.

interval Δx (see Eq.3.5) is given by:

$$\Delta c(x,t) = \frac{F(x,t)P(x,t)}{Q(t)}\Delta x. \tag{3.9}$$

When taking constant Δx increments, Δc increments are large at the entrance and then decrease rapidly.

At the entrance of the "standard" fracture (see Tab.3.1) $\Delta c(x{=}0)[\mu mol/cm^3] \approx 0.003 \cdot \Delta x$. In this case the solution would already attain equilibrium within the first Δx if $\Delta x > 60\,cm$. To avoid such a numerical saturation one has to use sufficiently small Δx increments. It is more convenient to use fixed Δc increments and calculate suitable Δx. We will use $\Delta c = c_s/i_1$ for $c < c_s$ and $\Delta c = (c_e q - c_s)/i_2$ for $c > c_s$. Parameters i_1 and i_2 are in the order of $100 - 1000$. Note that in this case Δx varies in time which has to be considered in a numerical algorithm. See also (Dreybrodt, 1996) for more details.

Time discretisation is done so, that a further decrease of Δt increments does not considerably affect the time scale of the evolution. Time increments can be either fixed or they can be calculated for each time step such that the maximal widening rate does not exceed some prescribed value.

NUMERICAL RESULTS FOR "STANDARD" FRACTURE

Fig. 3.3 shows the numerical results for the evolution of the standard fracture (Tab.3.1). Initially, the increase of flow rate is slow. High dissolution rates are restricted close to the entrance of the fracture. There the dissolution rates are linear and (we will show this later) drop exponentially with distance x. At some point x_s, the switch concentration c_s is reached and from there on the dissolution rates follow a non-linear relation and drop hyperbolically (this will be also shown later).

The mutual dependence of flow and dissolution rates results in a positive feedback mechanism; due to the dissolutional widening of the fracture the flow rate increases, consequently the dissolution rates along the entire fracture increase and so on, until finally a dramatic increase of flow and dissolution rates terminates the initial karstifiation state. This can be seen on Fig.3.3a. This event, called **breakthrough**, terminates the initial state of conduit evolution.

The breakthrough time, i.e. the time when breakthrough occurs, can be defined in several ways:

- When the linear kinetics reaches the exit of the fracture
- At the onset of turbulent flow, according to the Reynolds number
- At the time when the ratio $Q(t)/Q(t{=}0)$ reaches some value; e.g. 10^3

All these criteria give similar results for most cases of interest. The

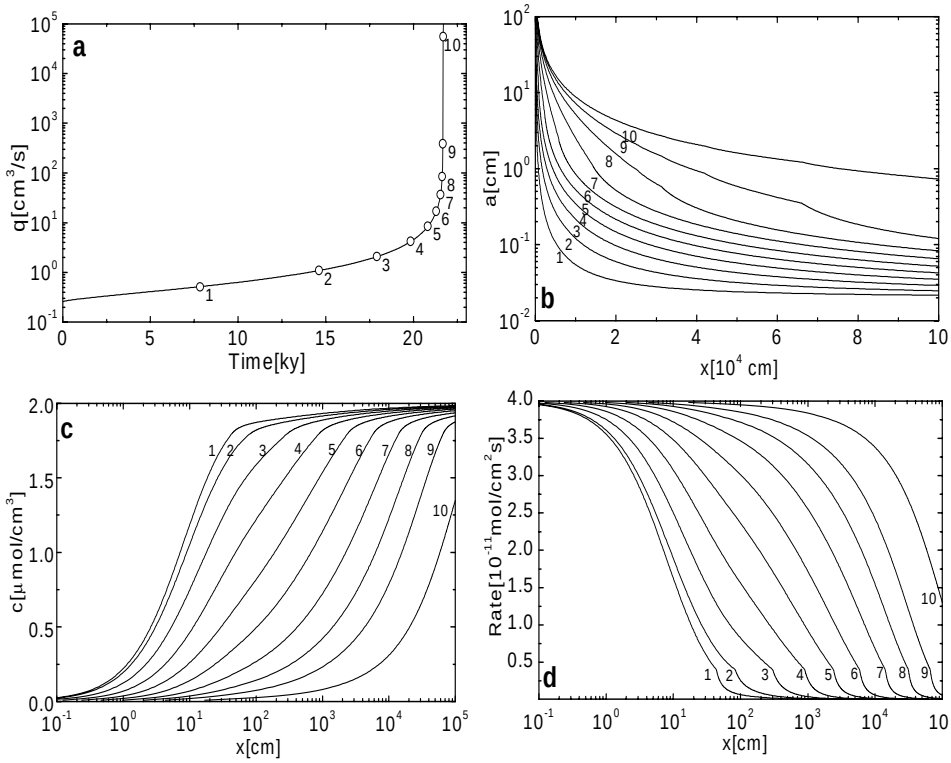

Figure 3.3: Evolution of a single fracture in time and space: numerical results. **a)** Evolution of the flow rate in time. Open circles denote the times when profiles in figures b,c and d were recorded. **b)** Evolution of aperture widths. Note the logarithmic scale for a. **c)** Evolution of concentration. **d)** Evolution of dissolution rates. Note the logarithmic scale for x in figures b and c. Profiles are recorded each time the flow rate doubles. Parameters used in the model run are given in Tab. 3.1

breakthrough event terminates the initial state of speleogenesis and can thus be taken as a measure for the intensity of a subsurface karstification.

As time progresses, the region with linear kinetics penetrates deeper into the fracture. After breakthrough the entire fracture is widened uniformly by the first order dissolution kinetics. By sensitivity analysis we find that the dependence of breakthrough time on the basic parameters can be expressed in the form of power law:

$$T_B = \tau \cdot (L/i)^{\frac{n}{n-1}} \cdot a_0^{\frac{-2n+1}{n-1}} \cdot k_n^{\frac{1}{n-1}} \cdot c_{eq}^{\frac{-n}{n-1}}. \tag{3.10}$$

The value of τ is $9 \cdot 10^{-14} \pm 10^{-14}$ for square and circular cross-sections, and about an order of magnitude smaller for wide fractures, i.e. $b_0 \gg a_0$ (Dreybrodt, 1996). Error is less than 15% for $T_B > 10^4$ years.

3.1.2 AN ANALYTICAL APPROXIMATION FOR THE BREAKTHROUGH TIME

Fig.3.3 shows that during 90% of the evolution time, fast dissolution rates are restricted only close to the entrance. The rest of the fracture is widened almost uniformly by slow dissolution rates, not much higher than that at the exit. This enables an approximation which assumes that the dissolution rates along the fracture are constant and equal to that at the exit. Explicitly the approximation yields:

$$a(x,t) = a(L,t), \tag{3.11}$$

$$F(x,t) = F(L,t). \tag{3.12}$$

Fig.3.4 illustrates this approximation. The evolving funnel shape of the fracture is neglected and the fracture is kept parallel during the evolution. For the uniform fracture Eq.3.6 can be solved analytically.

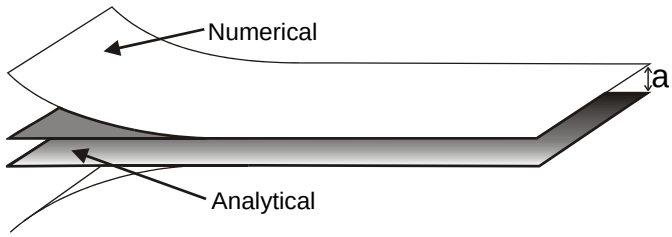

Figure 3.4: The evolving funnel shaped fracture is approximated by a fracture of uniform width widened evenly by the dissolution rates at the fracture's end. This enables an analytical treatment of its evolution.

To obtain the concentrations $c(x)$ and rates $F(x)$ for the uniform fracture, we insert the expressions for the dissolution rate (Eq.2.11) into Eq.3.6 and obtain:

$$\frac{1}{k_1}\int_{c_0}^{c<c_s}\frac{dc}{1-c(x)/c_{eq}} = \int_0^x \frac{P}{Q}\,dx, \quad x \le x_s, \tag{3.13}$$

$$\frac{1}{k_n}\int_{c_s}^{c(x)}\frac{dc}{(1-c(x)/c_{eq})^n} = \int_{x_s}^x \frac{P}{Q}\,dx, \quad x > x_s. \tag{3.14}$$

Integrating [1] the upper equations we obtain:

$$1-c(x)/c_{eq} = (1-c_0/c_{eq})\exp\left(-\frac{Pk_1x}{Qc_{eq}}\right),\ x \le x_s, \tag{3.15}$$

$$(1-c(x)/c_{eq})^{-n+1} = (1-c_s/c_{eq})^{-n+1} + \frac{Pk_n(n-1)(x-x_s)}{Qc_{eq}},\ x > x_s. \tag{3.16}$$

[1] The integrals are basic integrals of power functions

Inserting $x = x_s$ and $c(x) = c_s$ in Eq.3.15 we get:

$$x_s = \frac{Qc_{eq}}{Pk_1} \ln\left(\frac{1 - c_0/c_{eq}}{1 - c_s/c_{eq}}\right). \tag{3.17}$$

Using Eq.2.11 we write the term $(1-c(x)/c_{eq})$ as a function of $F(x)$ and reorder the upper expressions to obtain the explicit form for the dissolution rates:

$$F(x) = F(x=0)\exp\left(-\frac{Pk_1}{Qc_{eq}}x\right),\ x \le x_s, \tag{3.18}$$

$$F(x) = F(x_s)\left[1 + \frac{Pk_n(n-1)(x-x_s)}{Qc_{eq}(1-c_s/c_{eq})^{1-n}}\right]^{n/1-n}, x > x_s. \tag{3.19}$$

More generally, if the rate at some point x_1 is known and the non-linear rate law with constant c_{eq}, k_n and n describes the dissolution between the point x_1 and some other arbitrary point x_2, the rate at x_2 is given by

$$F(x_2) = F(x_1)\left[1 + \frac{Pk_n(n-1)(x_2-x_1)}{Qc_{eq}(1-c(x_1)/c_{eq})^{1-n}}\right]^{n/1-n} \tag{3.20}$$

for $\quad x_2 > x_1$.

The problem is further simplified by taking a wide fracture, i.e. $b \gg a$. In this case

$$\frac{a+b}{a^3 b} \approx \frac{1}{a^3} \quad \text{so that} \quad P/Q = \frac{24\eta}{\rho g}\frac{L}{a^3 h}. \tag{3.21}$$

For more transparency we define new parameters λ_1 and $\lambda_n(x)$ with the dimension of length

$$\lambda_1 = \frac{Qc_{eq}}{Pk_1}, \tag{3.22}$$

$$\lambda_1 = \frac{\rho g}{24\eta}\frac{a^3 h}{L}\frac{c_{eq}}{k_1}\ ,\ b \gg a, \tag{3.23}$$

$$\lambda_n(x) = \frac{Qc_{eq}(1-c(x)/c_{eq})^{1-n}}{Pk_n(n-1)}, \tag{3.24}$$

$$\lambda_n(x) = \frac{\rho g}{24\eta}\frac{a^3 h}{L}\frac{c_{eq}(1-c(x)/c_{eq})^{1-n}}{k_n(n-1)}\ ,\ b \gg a. \tag{3.25}$$

Note that $\lambda_n(x_s) = \lambda_1/(n-1)$ since $k_n = k_1(1-c_s/c_{eq})^{1-n}$. Eqs.3.18-3.20 now take the forms:

$$F(x) = F(0)\exp\left(-\frac{x}{\lambda_1}\right)\ ,\ x \le x_s, \tag{3.26}$$

$$F(x) = F(x_s)\left[1 + \frac{x-x_s}{\lambda_n(x_s)}\right]^{\frac{n}{1-n}}\ ,\ x > x_s, \tag{3.27}$$

$$F(x_2) = F(x_1)\left[1 + \frac{x_2-x_1}{\lambda_n(x_1)}\right]^{\frac{n}{1-n}},\ x_2 > x_1 > x_s. \tag{3.28}$$

These equations will be the "bread and butter" for the later discussions. Parameters λ_1 and $\lambda_n(x)$ define how fast the dissolution rates decrease along the fracture or how far first order dissolution rates penetrate into the fracture. The expression **penetration lengths** will be used to refer to them. For non-linear kinetics, the penetration length $\lambda_n(x)$ increases along the fracture due to increasing concentration. This is not the case for λ_1 which does not depend on the x coordinate.

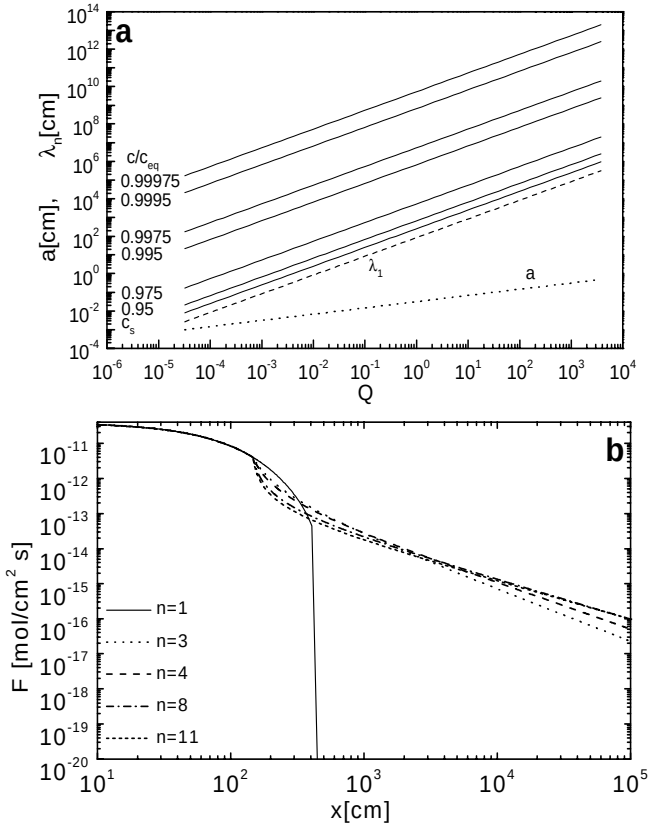

Figure 3.5: **a)** Dependence of penetration lengths λ_n (solid lines) and λ_1 (dashed line) on Q. λ_n is shown for various values of c/c_{eq} as denoted at the lines. The dotted line shows the aperture width for the uniform "standard" fracture (see Tab.3.1) which corresponds to the values of Q at the abscissa. **b)** Dissolution rates along the uniform "standard" fracture for various order n of the rate equation as denoted in the figure.

Fig.3.5a gives the dependence of λ_n on the flow rate for various values of saturation ratios c/c_{eq} (given in the figure). The dashed line gives the dependence of λ_1. This does not depend on c/c_{eq}. The dotted line presents the aperture widths corresponding to the flow rate Q for the uniform fracture. Other parameters are those given in Tab.3.1.

Figure 3.5b shows the dissolution rates along the uniform fracture. The

solid lines present the case where only linear kinetics acts along the fracture. The other lines (see figure) present the cases where the rate law switches higher order at $c > c_s$. The "standard" fracture parameters given in Tab.3.1 were used to calculate the rates, except for the varying parameters n and k_n. If only linear kinetics acts, the rates drop exponentially and are reduced by 13 orders of magnitude within a short distance. In contrast when non-linear kinetics is active the rates are reduced only moderately by about 3 orders of magnitude .

In our approximation we have assumed a plane parallel uniform fracture ($a_0 \ll b_0$), widened uniformly by the rate at its exit. Its widening is described by:

$$\frac{da}{dt} = 2\gamma F(L,t). \tag{3.29}$$

where $F(L,T)$ is given in Eq.3.27. For natural karstification the relations $L \gg x_s$ and $L/\lambda_n(x_s) \gg 1$ are valid. This can be verified by Eqs.3.17 and 3.25 and also be seen on Fig.3.5. Therefore we neglect the terms "1" and x_s in Eq.3.27.

For a uniform fracture the time dependence of $\lambda_n(x_s)$ can be written as

$$\lambda_n(x_s,t) = \lambda_n^0(x_s)\left(\frac{a(t)}{a_0}\right)^3. \tag{3.30}$$

We introduce $\lambda_n^0(x_s)$ to denote $\lambda_n(x_s, t=0)$. Inserting $\lambda_n(x_s,t)$ into Eq.3.27 we obtain:

$$F(L,t) = F(c_s)\left[\frac{L}{\lambda_n^0(x_s)}\frac{a_0^3}{a(t)^3}\right]^{\frac{-n}{n-1}}. \tag{3.31}$$

Applying the obtained $F(L,t)$ in Eq.3.29 gives an easy integrable widening equation:

$$\frac{da}{dt} = 2\gamma F(c_s)\left(\frac{\lambda_n^0(x_s)}{L}\right)^{\frac{n}{n-1}}\left(\frac{a(t)}{a_0}\right)^{\frac{3n}{n-1}}. \tag{3.32}$$

The widening rate is proportional to the power $3n/(n-1)$ of the actual aperture width. This explains the strong feedback mechanism seen in the numerical results. The integral of Eq.3.32 gives the time dependence of the aperture width:

$$a(t) = a_0\left(1 - t/T_B\right)^{\frac{1-n}{2n+1}}, \tag{3.33}$$

where

$$T_B = \frac{1}{\gamma}\cdot\frac{n-1}{2n+1}\left(\frac{1}{a_0}\right)^{\frac{2n+1}{n-1}}\left(\frac{24\eta L^2(n-1)}{\rho g h c_{eq}}\right)^{\frac{n}{n-1}} k_n^{\frac{1}{n-1}} \tag{3.34}$$
$$= \frac{1}{2\gamma}\frac{(n-1)}{(2n+1)}\frac{a_0}{F(L,0)}.$$

T_B is the pole of $a(t)$ and represents an estimation for the breakthrough time. It is inversely proportional to the inital widening rate at the exit. It has the same functional dependence on the basic parameters as the numerically obtained expression for T_B given in Eq.3.10. In the following chapters additional parameters will be added to the model. Then the the symbol T_B^0 will be used to refer to the breakthrough time given in Eq.3.34. Fig.3.6a shows the evolution of fracture aperture widths as calculated from the Eq.3.33. Note, that the T_B given in Eq.3.34 is an upper limit, since

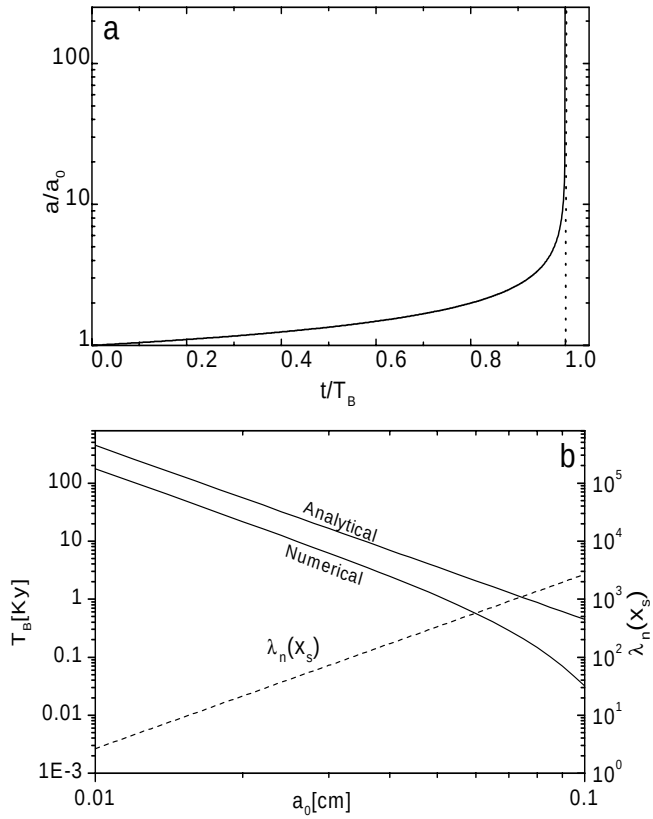

Figure 3.6: **a)** Evolution of fracture aperture width at the exit as given by Eq.3.33. The dotted vertical line represents the pole of the function $a(t)$. **b)** Dependence of breakthrough time on a_0 for otherwise standard fracture. The upper line gives the T_B from Eq.3.34, the lower line is obtained by the finite difference model. The dotted line gives the value of $\lambda_n^0(x_s)$. Note the logarithmic scale on both axes. Analytical approximation and numerical solution follow the same power law for $a_0 < 0.06\,cm$. The assumptions which lead to the approximation fail at higher a_0 and higher initial penetration lengths. Then the both curves start to deviate from each other.

the minimal rates were taken along the entire fracture to calculate its evolution. This is shown on Fig.3.6b. The upper solid line represents Eq.3.34, the lower one the results of a numerical run. The initial width is varied

between $0.01\,cm$ and $0.1\,cm$, all the other parameters are kept constant (see Tab.3.1). Up to $a_0 \approx 0.06\,cm$, the ratio between the analytically and numerically obtained breakthrough times is practically constant. For $a_0 > 0.06\,cm$ the numerical breakthrough behaviour starts to deviate from the power law ant the approximation fails. There the assumptions $L \gg x_s$ and $L \gg \lambda_n^0(x_s)$ are no longer valid.

The dashed line and the scale at the right vertical axis show the initial $\lambda_n^0(x_s)$. Using Eq.3.25, the variation of any parameter can be expressed as the variation of $\lambda_n^0(x_s)$. It shows out that regardless of which parameter we vary, the approximation given in Eq.3.34 fails if $L/\lambda_n^0(x_s) < 100$.

AN IMPORTANT CONCLUSION

The keystone of the presented approximation is that the breakthrough time is determined by the initial dissolution rates at the "bottleneck" part where the resistance to flow is maximal and the dissolution rates are minimal. Here the bottleneck is at the fracture's end. When hydrogeochemical conditions favour the formation of bottleneck somewhere else in the fracture one should focus on the initial rates there to estimate the behaviour of the breakthrough time. We will benefit from this fact also when adding further parameters to the basic settings presented in this chapter.

3.1.3 SOLUTIONS WITH HIGH INITIAL SATURATION RATIOS. "SWITCH OFF" OF THE FEEDBACK MECHANISM

Before entering the closed system, karst water normally dissolves limestone under open system conditions. Therefore it enters the fractures with the saturation ratio $c_0/c_{eq} > 0$. The question is how does this affect the evolution of a single fracture.

Fig.3.7a shows the evolution of flow rates for the standard fracture for several ratios c_0/c_{eq} as denoted in the figure. Flow rates beyond turbulence, i.e. above the dotted line, are unrealistic and are given for completeness and support to the later discussion. As long as the initial concentration is below the switch concentration (lines 1-4), no considerable change of T_B is observed. Line 4 shows the case when $c_0 = c_s$. If c_0 is higher than c_s, T_B starts to increase and as c_0 approaches c_{eq} (lines 6-8) breakthrough no longer occurs in the sense of an abrupt jump in flow rates. In these cases the fracture widens uniformly in time from the onset of karstification.

A more general picture of the behaviour of T_B on c_0/c_{eq} is given in Fig.3.7b. The solid line denotes the dependence of T_B on c_0/c_{eq}. The

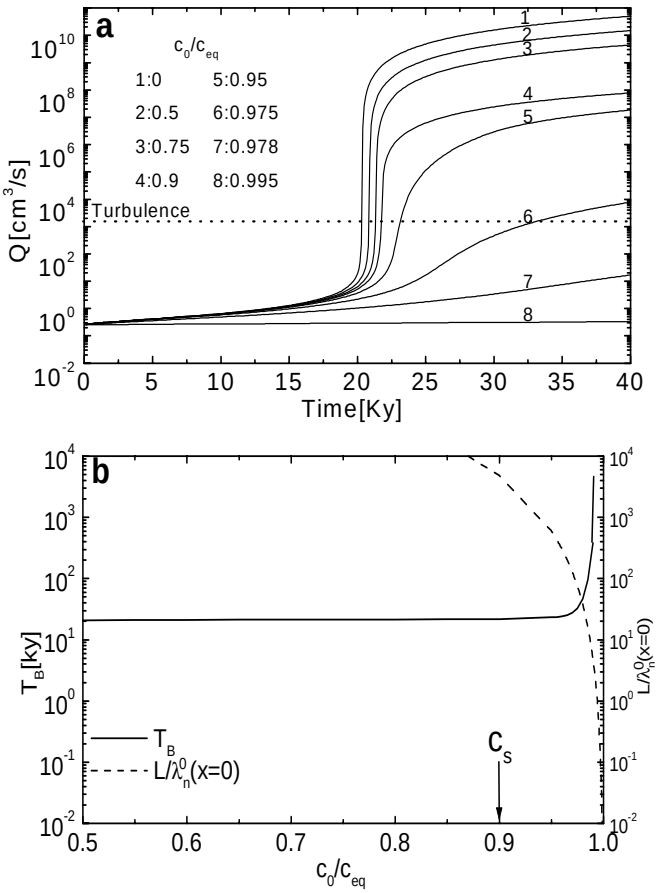

Figure 3.7: **a)** The evolution of flow rate in standard fracture for various values of c_0/c_{eq} as denoted in figure. **b)** The dependence of breakthrough time (solid line) and parameter $L/\lambda_n(x=0,t=0)$ (dashed line) on c_0/c_{eq}. Arrow indicates the value of c_s. No considerable change is observed if $c_0/c_{eq} < 0.97$.

dashed line shows the dependence of $L/\lambda_n^0(x=0)$ on c/c_{eq}, both for the standard fracture. The same scale is used for both variables. As stated above, no effect on T_B is observed if $c_0 < c_s$. A considerable increase of T_B is observed once the ratio L/λ_n^0 drops to 10, where $c_0/c_{eq} \approx 0.97$. From thereon T_B increases steeply. No breakthrough occurs if $L/\lambda_n^0 < 0.1$.

The feedback mechanism is active as long as $L/\lambda_n(0,t) \gg 1$. Once this ratio becomes close or even smaller than one the dissolution rates along the entire fracture are almost equal to that at the entrance (see Eq.3.27). The entire fracture is then widened linearly in time as shown by Fig.3.7a. For very high initial saturation ratio (curves 7 and 8 on Fig.3.7a) this happens already at the onset of widening.

The presented discussion is not only valid for fractures dissolved by autogenic waters flowing from the surface, but also holds for fractures situated

deep in the phreatic zone where the parameter $\lambda_n^0(x=0)$ can take a value of several kilometres and even widening in the order of $10^{-9}\,cm/year$ can enlarge these fractures in a time scale of several millions of years. When the hydrogeological conditions change, these fractures can become preferential pathways for later karstification. This can provide an explanation for the concept of inception horizons, without assuming other mechanisms as discussed by Lowe (1997).

3.1.4 EVOLUTION OF A SINGLE FRACTURE UNDER LINEAR DISSOLUTION KINETICS

We stressed the importance of the higher order ($n > 1$) dissolution kinetics for the conduit development. The non-linear rate equation close to equilibrium is valid for natural limestones and dolomites and according to the latest results (Jeschke et al., 2000) also for gypsum. Nevertheless, for historical reasons, for completeness, and for "what if ?" we will discuss the conduit evolution under the action of linear dissolution kinetics only. We therefore assume that the linear part of of Eq.2.11 is valid until c_{eq}:

$$F(c) = k(1 - c/c_{eq}). \tag{3.35}$$

So far we did not consider the diffusion control of dissolution rates. Numerical results show that for karstification with a non-linear rate law, diffusion plays a minor role and does not much alter the breakthrough time. In contrary we will see that for the case with linear kinetics diffusion plays a crucial role.

Now we consider the combined action of surface reaction and diffusional transport of dissolved ionic species. As shown by Buhman and Dreybrodt (1985a; 1985b; 1988) this can be done by using a modified rate constant which yields:

$$k = k_D = k_1 \left[1 + \frac{k_1 a}{6 D c_{eq}}\right]^{-1}. \tag{3.36}$$

From this equation one can deduce three regions of dissolution.
If $k_1 a/6Dc_{eq} \ll 1$ we obtain $k \approx k_1$, such that the dissolution is purely surface controlled. The dissolution is purely diffusion controlled when $k_1 a/6Dc_{eq} \gg 1$. Between the two extremes is the region where the dissolution is controlled by both (mixed kinetics). Suppose that the diffusion is not important for the evolution of a fracture, so that $k = k_1$. Fig.3.8a shows the evolution of flow rates for two fractures with different hydraulic gradients. All the other parameters are the same for both cases (see the figure caption). T_B for $i = 0.25$ is $1.2\,ky$ and there is no breakthrough for $i = 0.2$. Fig.3.8b shows dependence of T_B on λ_1^0/L (see Eq.3.23). The full line denotes the case where λ_1^0 is varied by varying a_0 and keeping the

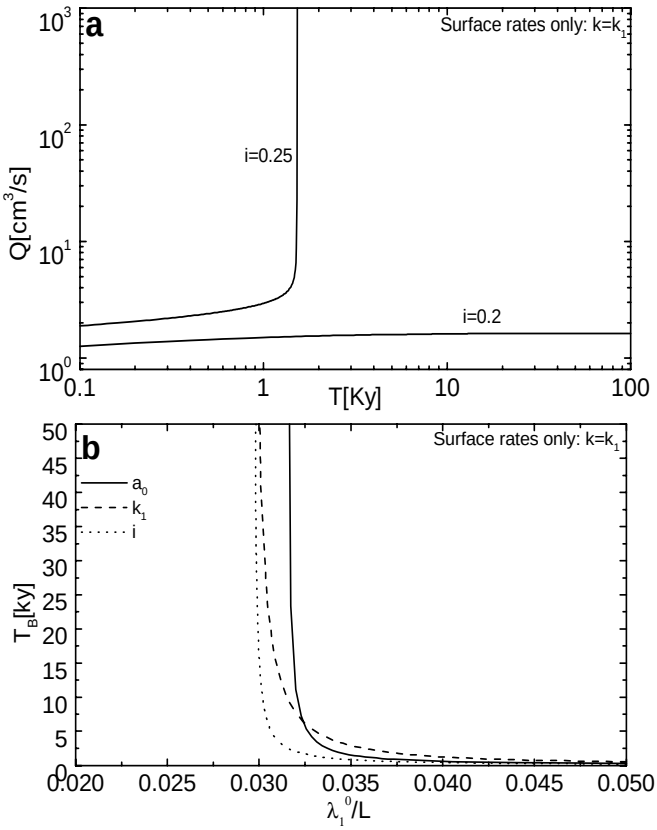

Figure 3.8: **a)** Evolution of the flow rate for the case of linear kinetics when only surface rates are considered. $a_0 = 0.02cm$, $b_0 = 100cm$, $L = 10^4 cm$, $k_1 = 4 \cdot 10^{-11} mol/cm^2 s$, $c_{eq} = 2 \cdot 10^{-6} mol/cm^3$, $i = 0.2$ and $i = 0.25$ as denoted at the lines. **b)** The dependence of T_B on λ_1^0/L. This is varied by varying a_0, k_1 and i presented by the solid, dashed and dotted lines respectively. Other parameters are the same as in figure a.

other parameters constant. The dashed and dotted lines present the cases where k_1 and i are the varying parameters. There is a sharp limit between the region of parameters where breakthrough occurs and the region without breakthrough. All three curves show the same behaviour. Therefore we can take λ_1^0/L as a master parameter determining the breakthrough behaviour.

Now we include diffusion by using Eq.3.36 as the rate equation. Fig.3.9 presents the evolution of flow rates for the same fracture as in Fig.3.8a but with diffusion included. Now the breakthrough time for $i = 0.2$ is below $1\,ky$. As shown by Fig.3.8b, there is no sharp boundary dividing the region of parameters with and without breakthrough. In this case we obtain geologically relevant breakthrough times for much smaller values of λ_1^0/L.

Another example is shown on Fig.3.10a, which gives a wide range dependence of T_B on k_1 for the cases with $k = k_1$ and $k = k_D$. Other parameters

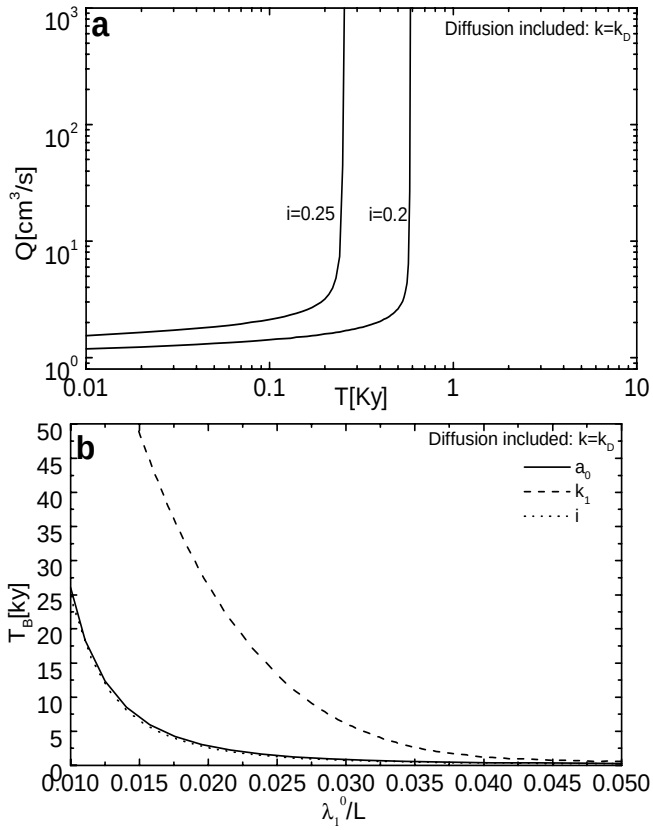

Figure 3.9: **a)** Evolution of the flow rate for the case of linear kinetics. Diffusion is included in the rate equation. Parameters are the same as in Fig.3.8. **b)** The dependence of T_B on λ_1^0/L. See also Fig.3.8b

are the same as in Fig.3.8. As long as $k_1 < 8 \cdot 10^{-12}$, the surface reaction determines the rates and the both cases coincide. For larger values of k_1 no breakthrough occurs if only surface rates are considered.

The question arises whether we can treat the problem with the approximation for the widening rate at the exit. From Eq.3.26 we get the exit dissolution rate. Introducing it into Eq.3.29 we obtain:

$$\frac{da}{dt} = 2\gamma k_1 \exp\left(-\frac{La_0^3}{\lambda_1^0 a^3}\right). \tag{3.37}$$

If the rates are mixed controlled we obtain:

$$\frac{da}{dt} = 2\gamma \frac{k_1}{1+\frac{k_1 a}{6Dc_{eq}}} \exp\left(-\frac{La_0^3}{\lambda_1^0 a^3\left(1+\frac{k_1 a}{6Dc_{eq}}\right)}\right). \tag{3.38}$$

The results of the integration are given in Fig.3.10b. T_B rises beyond any relevant value at higher values of λ_1^0/L than in Fig.3.8b. However it does

not show the asymptotic behaviour for $\lambda_1^0/L > 0$. There is practically no difference between case with and without diffusion, since the aperture width at the exit is small. Therefore the difference between Eqs.3.37 and 3.38 is negliable. We see that the approximation with the exit rate does not

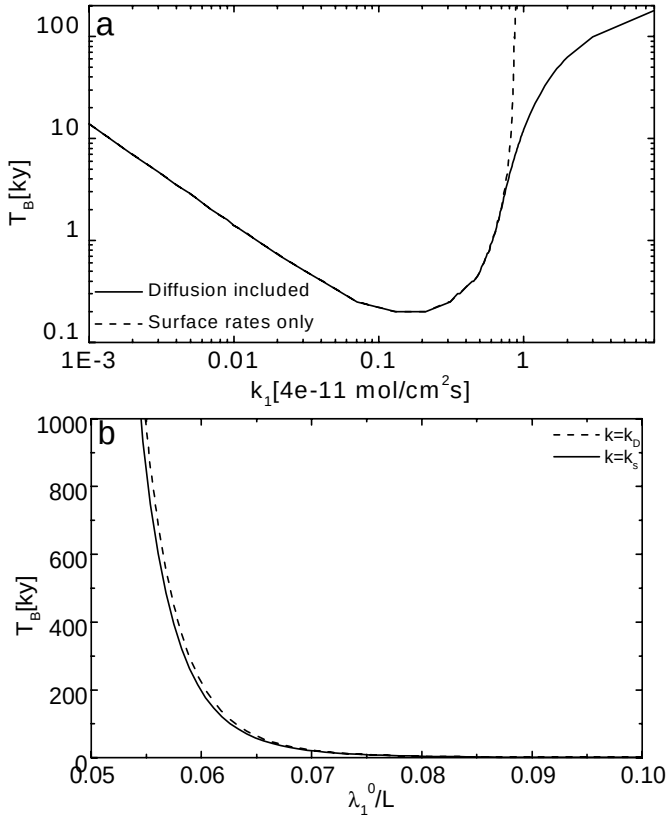

Figure 3.10: **a)**The dependence of T_B on k_1. The other parameters are as in Fig.3.8. The solid line presents the case when only surface controlled rates were included to the model, dashed line give the case where diffusion is considered. **b)** T_B dependence on λ_1^0/L obtained by solving Eqs.3.37 and 3.38.

explain the difference observed in numerical runs. To explain this difference we have to focus on the entrance part of the fracture. Fig.3.11a shows the evolution of aperture widths for the case with $i = 0.2$ from Fig.3.8a. The small graph shows the aperture widths in the first 10m of the fracture. This part exhibits extremely high aperture widths. Then the aperture widths drop fast such that more than half of the fracture keeps its initial flow resistance. High apertures at the entrance and almost constant resistance of the rest of the fracture cause the decrease of dissolution rates in time. For more on this see the discussion in (Dreybrodt, 1996) and in the following section.

Fig.3.11b shows the aperture widths if the diffusion is included in the rate calculation. Diffusion becomes rate limiting once the aperture widths are large (see Eq.3.36). For mixed control, the penetration length can be written as

$$\lambda_D = \lambda_1 \left(1 + \frac{k_1 a}{6 D c_{eq}}\right). \tag{3.39}$$

Since $\lambda_M > \lambda_1$ widening progresses deeper into the fracture. Furthermore, the diffusion prevents the uncontrolled widening at the entrance which causes the retreat of dissolution rates if only surface rates are assumed.

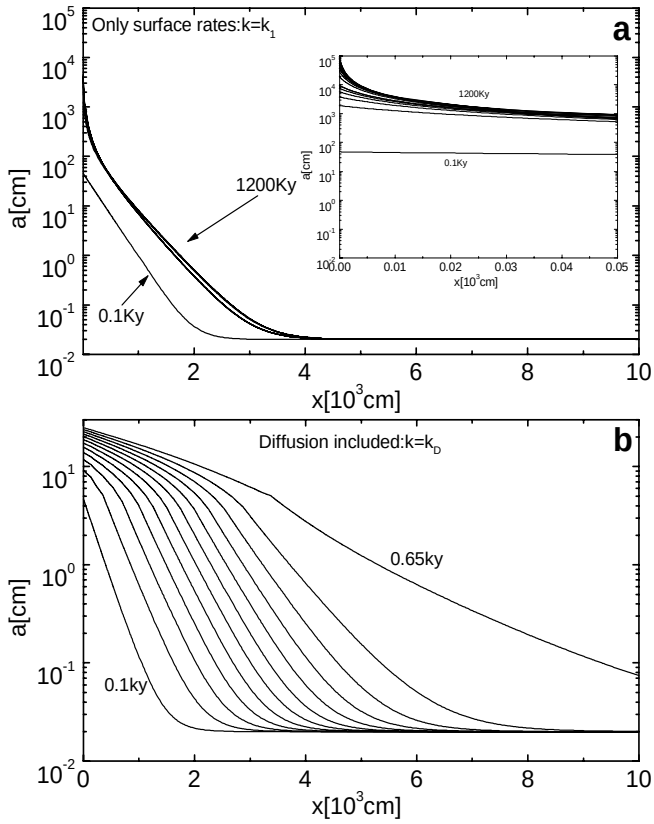

Figure 3.11: **a)** The profiles of the aperture widths for the case with $i = 0.2$ from Fig. 3.8. Only surface rates are considered. The excerpt shows the entrance part, $x < 500cm$. **b)** Same as in the figure a, but diffusion is considered. Profiles are taken each 100y, starting at 50y.

3.1.5 THE DIFFERENCE BETWEEN THE EVOLUTION OF DISSOLUTION RATES IN WIDE FRACTURES AND IN TUBES

We have discussed only the evolution of wide fractures. This enabled us to obtain analytical results due to the approximation given in Eq.3.21. Although the obtained results are conceptionally valid also for the tubes, one should be aware of an important difference between the two cases.

To clarify this difference we consider the dissolution rates along a fracture of general shape. This can be obtained the same way as for the parallel fracture, except that the right hand side of Eq.3.6 is left in the integral form :

$$F(x,t) = F(x=0)\exp\left(-\frac{k_1\int_0^{x_s} P(x,t)\,dx}{Q(t)c_{eq}}\right),\quad x < x_s \tag{3.40}$$

$$F(x,t) = F(x_s)\left[1+\frac{k_n(n-1)\int_{x_s}^{x} P(x,t)\,dx}{Q(t)c_{eq}(1-c_s/c_{eq})^{1-n}}\right]^{\frac{n}{1-n}},\ x > x_s \tag{3.41}$$

The ratio $\int_0^x P(x,t)/Q(t)dx$ includes the whole time dependence. Therefore it determines whether the dissolution rates along the fracture increase or decrease in time. If the ratio increases, the rate decreases and vice versa.

In wide fractures the relative change of perimeter in time is small, such that the dissolution rates increase in time with increasing flow rate.

This is not always true for tubes. In this case the time variation of perimeter and its integral along the fracture might exceed the time variation of flow rate. This is particularly important at the entrance of the fracture, where dissolution rates are high and fast widening occurs. As shown, if linear kinetics with surface controlled rates is assumed this might prevent the breakthrough also for the initially wide fractures ($a_0/b_0 = 0.01$).

3.1.6 SOME GENERAL CONCLUSIONS ON THE EVOLUTION OF A SINGLE FRACTURE

We have calculated the evolution of a single fracture by combining the basic flow equations, the knowledge on dissolution rates and the mass conservation law for the dissolved ionic species. The evolution is determined by chemical and physical parameters which define the flow through the fracture and dissolution rates along it. These parameters are given in Tab.3.1.

The evolution of a fracture is governed by a feed-back mechanism where an increase of flow rates causes an increase of dissolution rates and vice versa. This mechanism ends in an abrupt jump of flow and dissolution rates, termed as breakthrough. The breakthrough time can be expressed as a function of basic chemical and physical parameters (Eq.3.34). The

dependence of breakthrough time on these parameters follows the power law. Once the breakthrough occurs and turbulent flow sets in, the fracture is widened evenly with high dissolution rates.

The problem of the evolution of a single fracture is normally handled numerically. We presented an analytical approximation which gives the right dependence of breakthrough time on the basic parameters. The approximation assumes an even widening of the fracture with the dissolution rates at the exit.

The initial saturation ratio c_0/c_{eq} does not affect the feedback mechanism if the initial concentration is below the switch concentration. If the ratio c_0/c_{eq} is close to 1, i.e. $c_0/c_{eq} > 0.97$, the evolution is significantly affected and the feedback mechanism is switched off.

If only a linear rate law is assumed, one must consider the diffusional flux of dissolved ionic species as a rate controlling mechanism. If only surface controlled rates are assumed we observe a sharp boundary between the region of parameters where the breakthrough occurs and the region with no breakthrough. This might lead to wrong conclusions.

3.1.7 A TIME VARIATION OF THE HYDRAULIC HEAD

In nature the boundary conditions and the parameters defining karstification change during karst evolution. For reasons of clarity, most of the discussion in this work does not assume any time variation of the parameters given in Tab.3.1.

To get some insight into scenarios with time-varying parameters we present the case with a time dependent hydraulic head. One can envisage many scenarios where the hydraulic head changes: e.g. the downcutting of an erosional base, the change of precipitation rate or the change of hydraulic properties of an aquifer.

We assume some explicit time dependence of the hydraulic head $h = h(t)$. To obtain the breakthrough behaviour we can apply the same procedure as for the constant head conditions (Eqs.3.30-3.33). If the head variation is explicitly known it can be included into Eqs.3.30, 3.29 and 3.33. This gives the following relations:

$$\lambda_n(x_s,t) = \lambda_n^0(x_s)\left(\frac{a(t)}{a_0}\right)^3\left(\frac{h(t)}{h_0}\right), \tag{3.42}$$

$$\frac{da}{dt} = 2\gamma F(L,t) = 2\gamma F(c_s)\cdot\left(\frac{\lambda_n^0(x_s)}{L}\right)^{\frac{n}{n-1}}\cdot\left(\frac{a(t)}{a_0}\right)^{\frac{3n}{n-1}}\cdot\left(\frac{h(t)}{h_0}\right)^{\frac{n}{n-1}} \tag{3.43}$$

and

$$a(t) = a_0\left(1 - H(t)/T_B^0\right)^{\frac{1-n}{2n+1}}, \tag{3.44}$$

$$\text{where } H(t) = h_0^{\frac{n}{1-n}} \int_0^t h(t)^{\frac{n}{n-1}}\, dt\ . \tag{3.45}$$

T_B^0 is the breakthrough time as given in Eq.3.34 for the non-varying hydraulic head $h_0 = h(t = 0)$. Breakthrough time is obtained from the condition for the pole of the function $a(t)$ which yields:

$$h_0^{n/n-1} T_B^0 = \int_0^{T_B} h(t)^{n/n-1}\, dt. \tag{3.46}$$

The hydraulic head can increase or decrease in time. Depending on the particular situation various forms of its time-dependence can be assumed. As an example we assume a simple case where the hydraulic head drops

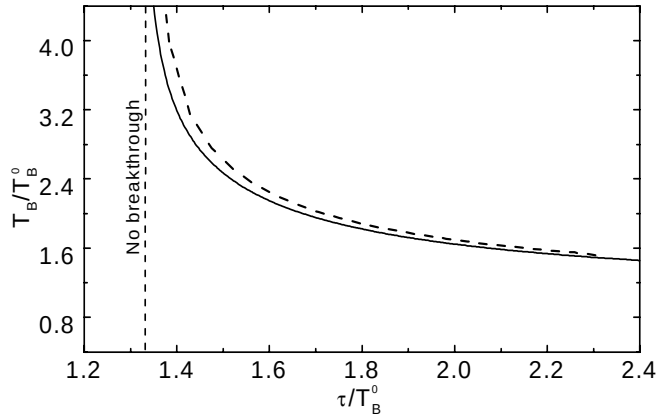

Figure 3.12: Dependence of T_B/T_B^0 on τ/T_B^0 in the case where the hydraulic head drops exponentially with time constant τ. The solid line represents Eq.3.47, the dashed one the results of finite differences model. The parameters for standard fracture are used. The vertical dashed line divides the regions of τ with and without breakthrough.

exponentially in time as $h = h_0 \exp(-t/\tau)$. We take this dependence for didactical reasons because it gives clear-cut results which can be easily obtained and interpreted. Integrating Eq.3.46 using this dependence and a bit of reordering gives:

$$T_B = T\frac{n-1}{n} \ln\left(\frac{1}{1 - \frac{T_B^0 n}{\tau(n-1)}}\right)\ . \tag{3.47}$$

The solid line in Fig.3.12 shows the dependence of T_B/T_B^0 on τ/T_B^0 as given by Eq.3.47, the dashed line the dependence calculated by the finite differences model. The vertical dashed line divides the regions of breakthrough and no breakthrough. The condition for the breakthrough is $\tau > \frac{n}{n-1} T_B^0$.

When assuming a time dependence of other parameters, a similar treatment can be done. One has to bear in mind that these parameters are time dependent when karstification proceeds in nature and that further work on this topic is needed.

3.2 THE INFLUENCE OF FRACTURE ROUGHNESS ON KARSTIFICATION TIMES

Natural fractures exhibit various degrees of roughness. This section investigates the influence of fracture roughness on the breakthrough time of the karst conduits. First estimations on the influence of roughness on cave evolution were performed by Groves and Howard (1994a) on two-dimensional fracture network. They replaced the uniform aperture widths of the initial pathways by statistically distributed apertures and found breakthrough behaviour similar to that in smooth fractures. A more realistic approach is that of Hanna and Rajaram (1998) who performed simulations on a single two dimensional fracture with statistically distributed aperture width. We will discuss this model at the end of this section.

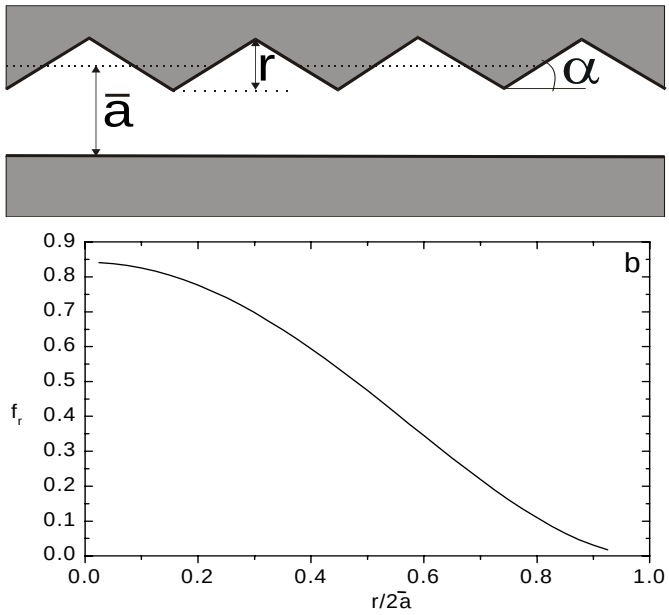

Figure 3.13: **a)** Geometry of an ideally rough fracture with a saw-toothed upper plane. r is the roughness amplitude. Initial relative roughness is $r/2\overline{a}_0$. **b)** The factor f_r which represents the effect of roughness on the flow rate, as a function of relative roughness $r/2\overline{a}$ for $\alpha = 35°$.

Using statistically distributed aperture widths along a single onedimensional fracture we have found that the breakthrough times do not change significantly provided that the standard deviation does not exceed $0.3a_0$. If σ however becomes close to a_0 it is highly probable that the fracture becomes blocked and its flow resistance becomes high enough to increase the breakthrough time dramatically. This approach needs many calculations with different distributions of initial aperture widths, and is thus not well

suited. It is also inconvenient for yielding clear-cut results on the influence of roughness to breakthrough times.

A more convenient approximation can be taken by replacing an irregular roughness by a regular one, which allows us to calculate the hydrodynamic resistance analytically. This was done recently by Ge (1997). He investigated the validity of the cubic law, i.e. the dependence of the flow rate on the third power of the average fracture width $\overline{a}$, for a general wide ($b \gg a$) rough fracture . He gives analytical results for a fracture consisting of one confining ideal plane and the other plane shaped by periodical triangles, as is illustrated in Fig. 3.13a.

Ge (1997) showed that the flow rate for such a fracture can be expressed as

$$Q_r = f_r \cdot Q_s, \tag{3.48}$$

where Q_s is the flow rate of the smooth fracture with aperture $\overline{a}$, given by:

$$Q_s = \frac{\rho g}{12\eta}\overline{a}^3 \cdot \frac{dh}{dx}. \tag{3.49}$$

The factor f_r is a function of the relative roughness $r/2\overline{a}$:

$$f_r\,(r/2\overline{a}) = \left(2\frac{r/2\overline{a}}{1 - r/2\overline{a}} + 1\right)^2 \cdot \left(\frac{r/2\overline{a}}{1 - r/2\overline{a}}\right)^{-4} \cdot \Phi(\alpha). \tag{3.50}$$

The parameter α is the angle of inclination as depicted in Fig.3.13a. $\Phi(\alpha)$ is a function of this angle (See Ge (1997)). Note from Fig.3.13a that $\alpha \to 0$ if $r \to 0$, such that $\Phi(\alpha) \to 1$ (See Ge (1997)). If $30^o < \alpha < 60^o$ then $\Phi(\alpha)$ varies between 0.7 and 0.9. In our calculations we used $\alpha = 35^o$ where $\Phi(\alpha) \approx 0.84$.

The factor f_r is a measure of the flow reduction due to the roughness of the fracture. For a completely rough surface when $r/2\overline{a} = 1$, f_r becomes zero since the fracture is blocked to flow. Fig. 3.13b depicts f_r as a function of $r/2\overline{a}$.

The roughness factor can be easily incorporated into the algorithm for single fracture evolution. Again, a typical breakthrough behaviour (e.g. as that in Fig.3.3) is observed in all cases, but the breakthrough time increases with relative roughness.

The breakthrough curves for various degrees of roughness are shown on Fig.3.14a. Fig.3.14b presents the ratio between the breakthrough times of the rough and the corresponding smooth fracture[2] versus initial relative roughness.

Results of the finite difference model are presented by the symbols. Various symbols denote various initial aperture widths and lengths as denoted in the figure. Curves present approximations which we discuss latter.

[2] T_B^s is equal to T_B^0 as given in Sec.3.1. In this section we use superscripts s and r to denote smooth or rough fractures, respectively.

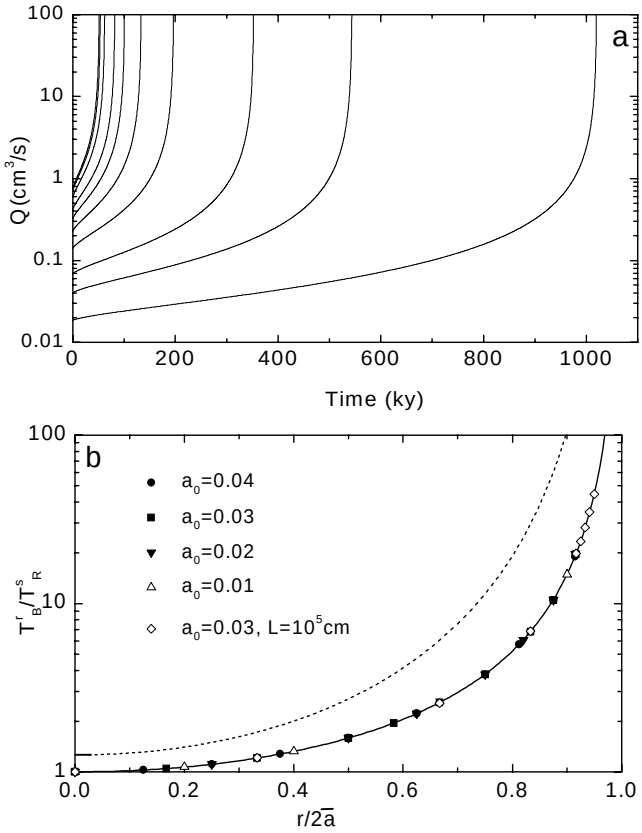

Figure 3.14: **a)** Breakthrough curves for the rough fractures with various degrees of roughness: $r/2\overline{a}_0 = 0$, 0.166, 0.333, 0.5, 0.583, 0.66, 0.833, 0.875, 0.916 from left to right respectively. $\alpha = 35°$, $L = 4{\cdot}10^5$, $\overline{a}_0 = 0.03\,cm$, other parameters as for standard fracture (see Tab.3.1) **b)** Dependence of the ratio between breakthrough time of rough fracture with the initial relative roughness $r/2\overline{a}_0$ and initially smooth fracture. The symbols represent results of the finite difference model for various initial widths and lengths. The full line shows the result obtained by integrating Eq.3.29 using Eq.3.51 for the exit rates. The dotted line represents the crude approximation given by Eq.3.52.

In the calculations the following assumptions are made:

- The roughness amplitude r is maintained during the dissolutional widening.
- Only the widths $a(x)$ change by dissolutional widening.

During the evolution of the conduit the roughness $r/2\overline{a}$ decreases continuously and the correction factor f_r looses its influence. Once $r/2\overline{a}$ has decreased to 0.2, which still is significant, the fracture develops almost like a smooth one. However, to get the upper estimation for the breakthrough time of the rough fracture, we assume that the relative roughness $(r/2\overline{a})$ is kept constant. We justify this assumption by the fact, that the aperture

width at the bottleneck is widened only a few times until breakthrough. To obtain the exit dissolution rate for the rough fracture we insert Eq.3.48 into Eq.3.19:

$$F_r(L) = F(x_s)\left[\frac{LPk_n(n-1)(1-c_s/c_{eq})^{n-1}}{f_r Q_s}\right]^{\frac{n}{1-n}} = F_s(L)\cdot f_r^{\frac{n}{n-1}}. \quad (3.51)$$

As in Sec.3.1 we neglected terms x_s and 1 in expression for dissolution rates. $F_s(L)$ denotes the exit dissolution rate for the corresponding smooth fracture. Inserting the obtained rate into Eq.3.34 we get an estimation for the breakthrough time:

$$T_B^r = T_B^s \cdot f_r^{\frac{-n}{n-1}}. \quad (3.52)$$

This is depicted by the dotted line in Fig.3.14.

To improve the analytical result, we consider the decrease of relative roughness in time . Including the widening rate from Eq3.51 into Eq.3.29 we get an integral for the T_B^r, which has to be solved numerically. The results obtained are presented by the full line in Fig.3.14b. The ratio T_B^r/T_B^s is in complete accordance with the results of the finite difference model. As can be seen from Fig. 3.14b extreme roughness is necessary to exert significant influence to the breakthrough times.

It is difficult to estimate the roughness factor for natural fractures, which exhibit roughness on both confining sides. Nevertheless the idealized rough fracture as depicted by Fig.3.13 can be regarded as a first approach, and it is reasonable to generalize the result in the following way. As long as the initial ratio $Q_0^r/Q_0^s \geq 0.3$ the influence of roughness does not increase the T_B for more than a factor of 2. To increase the breakthrough time by one order of magnitude, a $Q_0^r/Q_0^s = 0.02$ is needed. Therefore an extreme roughness is necessary for a drastic change and it seems that in most natural cases its influence is not very significant. Although this result might appear qualitative it gives a first estimation on the reliability of smooth fracture models of conduit evolution. Eqs.3.51 and 3.52 can be generally applied for any type of roughness provided that the function f_r is known.

It is more realistic to consider the fracture as a two-dimensional medium. This was done by Hanna and Rayaram (1998). Their results seem to be in conflict with ours, since they obtained that the breakthrough time decreases with roughness.

In rough two-dimensional fractures flow is channelled along the pathways (Tsang and Tsang, 1989) which exhibit lowest flow resistance. These channels are preferential for the breakthrough. Suppose that the roughness is varied in the way that the initial flow rate through the fracture is kept constant (Hanna and Rajaram, 1998). Then the flow velocities along the preferential channels increase with the roughness. Also the lengths of these channels increase with the roughness. With respect to the widening rates these two effects oppose each other. Still the effect of flow velocities is stronger so that the breakthrough time is decreasing with roughness.

3.3 EVOLUTION OF A SINGLE FRACTURE WITH VARYING LITHOLOGY

As stated in Chap.2.2, the kinetic order n depends on the type of limestone. According to Eisenlohr et al. (1999) it takes values between 3 and 11. The breakthrough time depends on the kinetic order, as can be seen from Eq.3.34. Fig.3.15a shows this dependence for the standard fracture (see Tab.3.1).

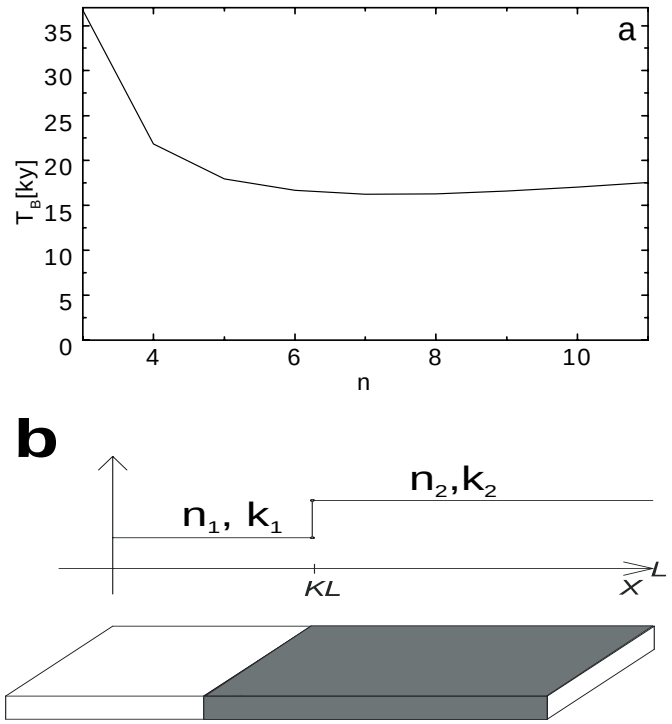

Figure 3.15: **a)** The dependence of the breakthrough time on the order of reaction for the standard fracture (see Tab.3.1). **b)** Fracture extending through the boundary between limestones with different kinetic properties.

Conduits often extend through several limestone formations with different kinetic properties. The concept of a single boundary is shown on Fig.3.15b. The dissolution rates are governed by the kinetic constant k_1 and order n_1 for $x < KL$ and k_2 and n_2 for $x \geq KL$.

How such kinetic boundaries do affect the dissolution rates is shown on Fig.3.16. This graph presents the dependence of the logarithm of dissolution rates on the logarithm of undersaturation $(1 - c/c_{eq})$. The full line illustrates the chemical evolution of a solution in a setting with two kinetic boundaries between the orders $n = 8$ and $n = 4$. Up to point A

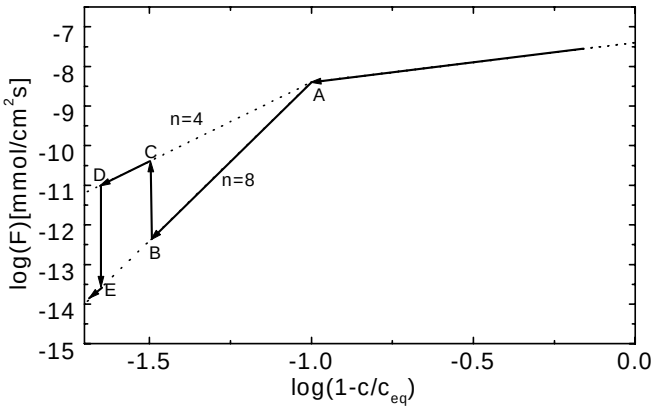

Figure 3.16: Dissolution rates in system with varying lithology. See text.

($c = c_s = 0.9c_{eq}$) the linear rate law acts. Then the non-linear rate law with $n = 8$ is active until point B. At point B the boundary to the fourth order kinetics boosts the dissolution rate for two orders of magnitude to point C. Between points C and D the dissolution proceeds with the fourth order kinetics. At point D another boundary to the eighth order is faced and the rates drop down to point E, which is more than two orders of magnitude lower than point D. Note from the figure, that the closer to saturation the solution is, the higher is the shift of the dissolution rate.

3.3.1 NUMERICAL RESULTS

Introducing varying lithology does not require many changes in the numerical algorithm for the evolution of a single fracture. Basically, the calculation procedure is the same as described in Sec.3.1. Additionally, one has to enter the parameters describing the positions of the boundaries and the rate orders for each lithology.

Let us first assume two different lithologies: n_1, k_{n_1} for $x \leq KL$ and n_2, k_{n2} for $x > KL$. We take the switch concentration for both lithologies equal; in this case the rate constants are related by $k_{n2} = k_{n1}(1 - c_s/c_{eq})^{n_1 - n_2}$. This gives only two additional parameters to the basic model presented in Sec.3.1: n_2 and K.

Fig.3.17 presents the numerical results for the standard fracture, with $n_1 = 4$, $n_2 = 6$ and $K = 0.5$ (a,b,c) and for the reverse case where $n_1 = 6$ and $n_2 = 4$ (d,e,f). The T_B for the first case (Fig.3.17a) is almost two orders of magnitude higher. Figures b,c,e and f confirm the discussion on Fig.3.16. Dissolution rates and aperture widths at the lithology boundaries face a step change either in the positive ($n_2 < n_1$) or negative directions

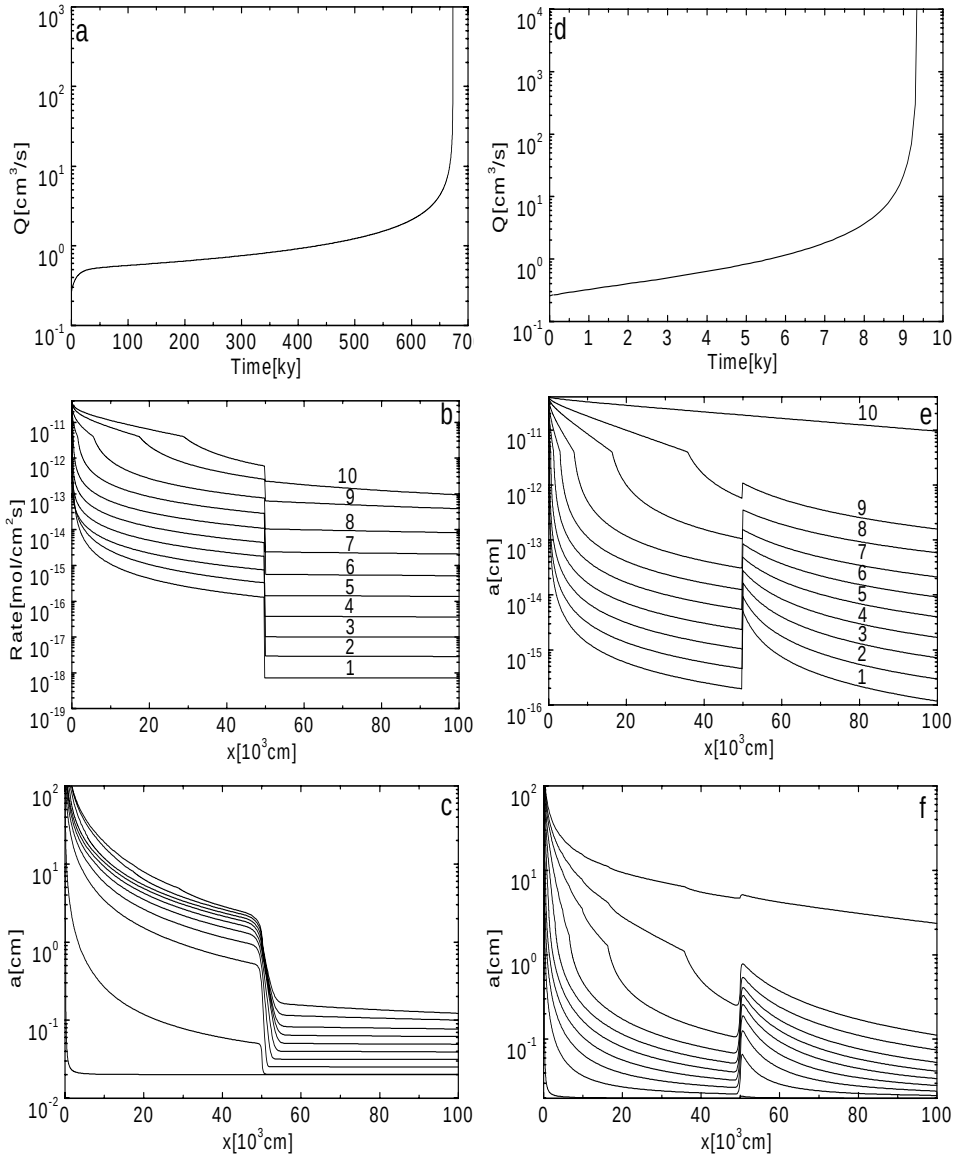

Figure 3.17: **a)** Evolution of flow rate in time for the standard fracture with $n_1 = 4$, $n_2 = 6$ and $K = 0.5$ (see Fig.3.15b). **b,c)** Profiles of dissolution rates and aperture widths for $n_1 = 4$, $n_2 = 6$ and $K = 0.5$ plotted at 0.1, 45.8, 452.1, 599.4, 649.1, 665.5, 670.9,672.5, 673 and 673.1 ky marked from 1-10 respectively. **d)** Evolution of flow rate in time for the standard fracture with $n_1 = 6$, $n_2 = 4$ and $K = 0.5$. **e,f)** Profiles of dissolution rates and aperture widths for $n_1 = 6$, $n_2 = 4$ and $K = 0.5$ at 0.1, 3.3, 5.8, 7.3, 8.2, 8.7,9, 9.2, 9.3 and 9.4 ky marked from 1-10 respectively.

($n_2 > n_1$). Therefore the evolution of a fracture strongly depends on the side from which the water enters.

To get some more insight into the problem, we can apply the bottleneck principle described in Sec.3.1. As shown there, the initial rate at the bottleneck is required to describe the breakthrough behaviour of the system. Without a proof, we can expect bottlenecks either at $x = KL$ or $x = L$, so we focus on the rates there. We use Eq.3.27 to obtain the initial rates at KL ($b_0 \gg a_0$ and $KL \gg x_s$) at the n_1 side of lithology boundary.

$$F(KL)_{n_1} = F(x_s)\left[1 + \frac{KL}{\lambda_{n_1}(x_s)}\right]^{n_1/(1-n_1)} \tag{3.53}$$

Concentration and therefore the saturation ratio is continuous across the boundary. From Eq.3.53 and Eq.2.11 we calculate the concentration at KL. Inserting it into the rate equation with n_2 and k_{n_2} we obtain the rate on the n_2 side of the boundary

$$F(KL)_{n_2} = F(x_s)\frac{k_{n_2}}{k_{n_1}}\left[1 + \frac{KL}{\lambda_{n_1}(x_s)}\right]^{n_2/(1-n_1)}. \tag{3.54}$$

The ratio between the rates on both side of the boundary at KL is

$$\frac{F(KL)_{n_1}}{F(KL)_{n_2}} = \frac{k_{n_1}}{k_{n_2}}\left[1 + \frac{KL}{\lambda_{n_1}(x_s)}\right]^{(n_1-n_2)/(1-n_1)}. \tag{3.55}$$

Employing Eq.3.28, we obtain the rate at the exit:

$$F(L) = F(KL)_{n_2}\left(1 + \frac{(1-K)L}{\lambda_{n_2}(KL)}\right)^{n_2/(1-n_2)}. \tag{3.56}$$

If $F(L) > F_{min}(KL)$ the bottleneck is at $x = KL$, otherwise it is at $x = L$.

3.3.2 THE CASE $n_2 > n_1$

If $n_2 \geq n_1$, the bottleneck is always at $x = L$, since the rates at the boundary drop and continue to drop as the solution proceeds towards the exit. To get at least an estimation for the behaviour of T_B, we make a rather crude approximation and assume the following:

- Penetration length λ_{n_2} is large, such that the rates do not change much between the boundary and the exit. Therefore $F(L) \approx F(KL)_{n_2}$ (see Eq.3.56).
- The first part of the fracture opens up quickly, therefore the hydraulic head acts only on the bottleneck part $x > KL$, i.e. $i = h/(1-K)L$.

These approximations enable us to get an estimate of T_B for $0.2 < K < 0.8$. Using the same procedure as in Sec.3.1, i.e. inserting the rate $F(KL)_{n_2}$ into Eq.3.29 and integrating it, we obtain

$$T_B \approx \frac{n_1 - 1}{3n_2 - n_1 + 1} \cdot \frac{a_0 \left(K(1-K)\right)^{\frac{n_2}{n_1 - 1}}}{2\gamma F(c_s)} \cdot \left(\frac{n_1 - 2}{2n_1 + 1} \cdot \frac{a_0}{2\gamma F(c_s)} \right)^{-n_2/n_1} \cdot \left(\frac{1}{T_B^0} \right)^{-n_2/n_1} . \quad (3.57)$$

T_B^0 is the breakthrough time if $n = n_1$ along the entire fracture. With increasing K, $F(KL)_{n2}$ and the length of the bottleneck part $(1 - K)L$ decrease. Both effects oppose each other with respct to the breakthrough time. This is maximal at $K = 0.5$ as can be calculated from Eq.3.57. Fig. 3.18a shows the dependence of T_B on K for the standard fracture with $n_1 = 4$ and $n_2 = 5, 6$ and 7. The dashed line denotes the approximation given in Eq.3.57 for $n_2 = 7$.

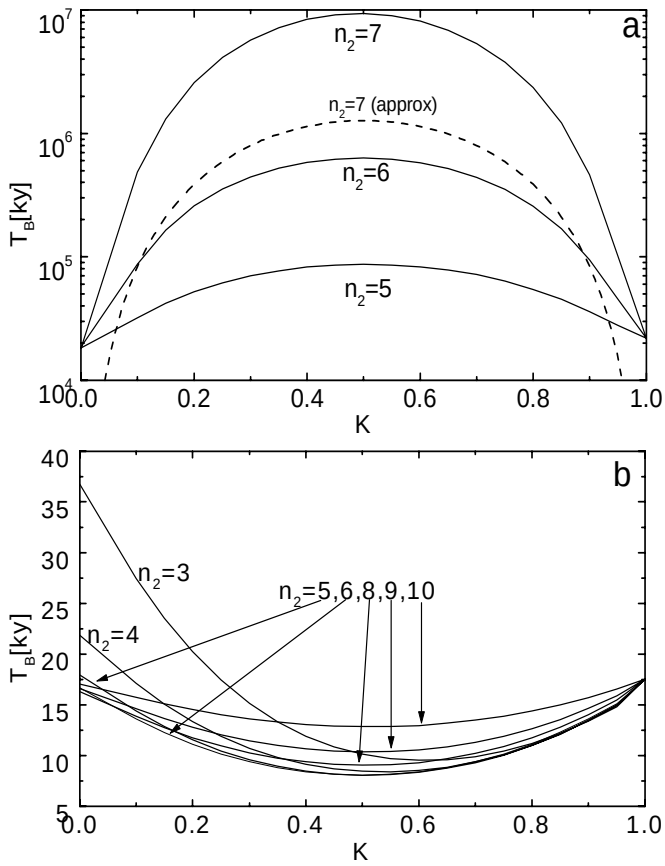

Figure 3.18: **a)** Dependence of breakthrough time on the position of lithological boundary ($x = KL$) for the standard fracture, where $n_1 = 4$ and $n_2 = 5, 6, 7$ (denoted on the line). The dashed line is an approximation given in Eq.3.57. **b)** As in figure **a**, but for $n_1 = 11$ and $n_2 = 10, 9, 8, 7, 6, 5, 4$ and 3.

3.3.3 THE CASE $n_2 < n_1$

If the rate order at the boundary drop, the dissolution rate is boosted up. The bottleneck can form either at $x = KL$ or at $x = L$ depending on the position of boundary and the change of dissolution rate there. For any pair of n_1 and n_2 there is a K where the rates at both possible bottlenecks are equal - we will call it K_{min}.

If $K < K_{min}$, the bottleneck is at the exit. As K increases, the rate at the exit increases and the length of the bottleneck part decreases. Consequently the breakthrough time drops with K.

Once K reaches the value K_{min} the two bottlenecks open simultaneously. Breakthrough with respect to K is minimal at this point.

For $K > K_{min}$, the bottleneck is at $x = KL$. The rate at KL decreases with increasing K and the length of bottleneck part ($x < KL$) increases. Both variations contribute to the rise of T_B with K.

The described behaviour is also shown in the Fig.3.18b. In this case $n_1 = 11$ and n_2 takes the values between 10 and 3.

3.3.4 MULTIPLE BOUNDARIES AND BOUNDARIES WITH INSOLUBLE ROCK

Arbitrary settings with multiple lithology can be assumed in nature as well as in the model. Fig. 3.19 gives an example of a fracture extending through a sequence of limestone sections with $n = 4$ and $n = 6$, starting with $n = 4$. The bottlenecks form in the region with higher kinetics order $n = 6$. $Q(t)$,

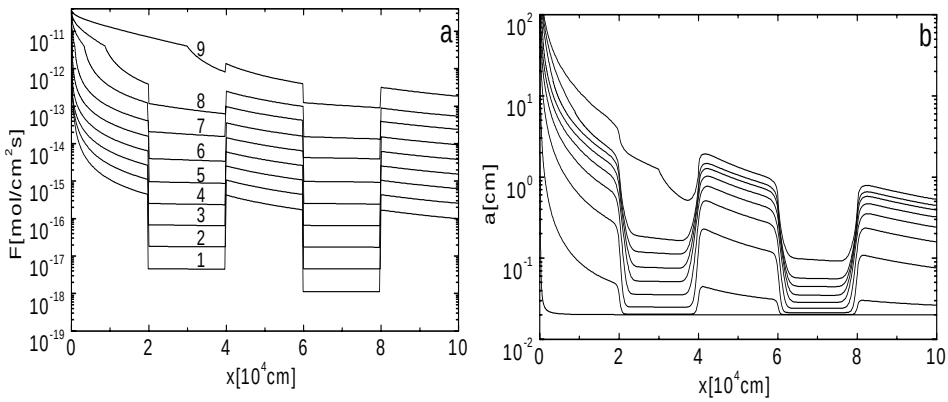

Figure 3.19: **a)** Evolution of dissolution rates in a fracture extending through four boundaries between $n = 4$ and $n = 6$. Lithology changes every $2 \cdot 10^4\, cm$. Profiles were recorded at 0.1, 14.6, 62.3, 99, 113.9, 119.7, 121.8, 122.4 and 122.7 ky, marked from 1-9 respectively. **b)** Aperture widths at the same times as in figure a.

not shown here, behaves as in Fig.3.17. Initially it rises fast due to the opening of $n = 4$ parts, but then builds up a plateau due to the bottlenecks in $n = 6$ regions which delay the breakthrough event. The rates between successive $n = 4$ regions are almost continuous, since the concentration within $n = 6$ regions rises only slightly, thus the aggressivity of the solution with respect to the limestone with $n = 4$ is preserved there.

One can imagine many possible lithology settings. The extreme contrast occurs when one part of the fracture extends through insoluble rock. In this case the flow rate initially rises due to the opening of the soluble part of the fracture, but the constant resistance of the insoluble part switches off the feedback mechanism. Fig.3.20 illustrates this.

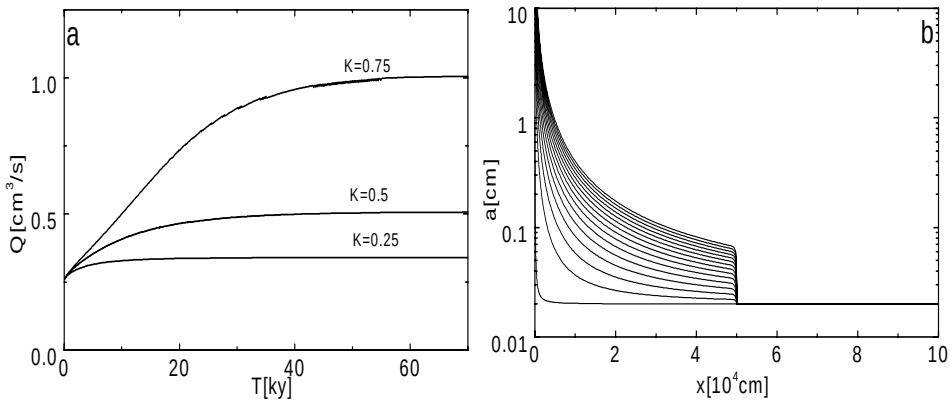

Figure 3.20: **a)** Evolution of flow rates in fracture with insoluble walls for $x \geq KL$ ($K = 0.25$, $K = 0.5$ and $K = 0.75$). **b)** Aperture width profiles for the $K = 0.5$. Lowermost line is at 100y, later profiles are taken with 4ky steps between 5 and 70ky.

Fig.3.20a shows the evolution of flow rates for the standard fracture with insoluble walls for $x \geq KL$ for three different values of K as denoted on the lines. Flow rate Q converges to the value $1/(1-K)Q_0$, where Q_0 is the initial flow rate and $(1-K)L$ is the length of the insoluble part. Figure 3.20b shows the evolution of fracture aperture widths for $K = 0.5$.

3.4 THE INFLUENCE OF SUBTERRANEAN CO_2 SOURCES ON INITIAL KARSTIFICATION: A SINGLE FRACTURE

Various geochemical settings can change the parameters of the rate equation within a single karstifying fracture. The change of the kinetic order n was discussed in Sec.3.3. Another parameter is the equilibrium concentration. This is determined by the content of CO_2 in the solution as shown in Sec.2.1. So far we have assumed that CO_2 stems entirely from the surface and that c_{eq} is constant along the entire fracture. One could assume various sources delivering CO_2 into the fracture and thus shifting the c_{eq}. Due to the non-linearity of the rate equation, the dissolution rates are highly sensitive to the variations of c/c_{eq} if the solution is close to saturation. During most of the initial karstification $c/c_{eq} > 0.99$ (cf. Fig. 3.3c) along almost the entire fracture . Therefore subterranean sources of CO_2, which increase the value of c_{eq}, might heavily influence the initial karstification processes. We discuss this topic in this section. It is not our aim to discuss the mechanisms of

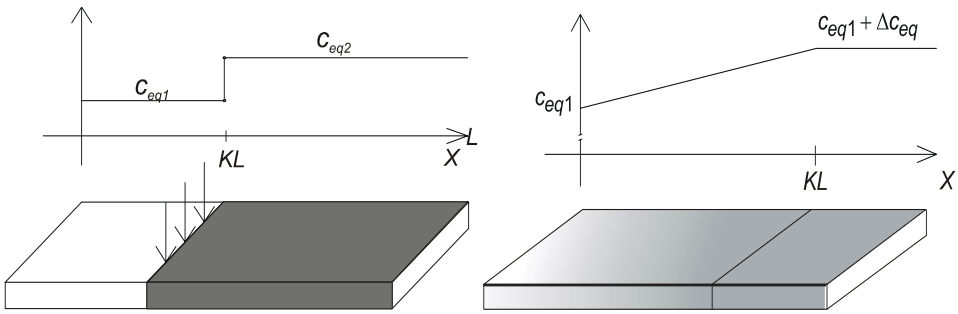

Figure 3.21: Conceptual models of subterranean CO_2 sources: **a)** Point source of CO_2 at position KL causes a step increase of c_{eq}. **b)** Even distribution of CO_2 input between the entrance of the fracture and the position KL causes a linear increase of c_{eq} in this region.

CO_2 delivery in detail, but to incorporate the effect of possible CO_2 sources into the model of a single fracture. We will focus on two simple cases:

- **Point input of** CO_2(Fig.3.21a): Although point sources are a rather unrealistic idealization, one can expect a very focused CO_2 delivery into the karstifying fractures when volcanic activity is present in the vicinity of evolving karst. The amount of CO_2 delivered by volcanic activity into the solution changes its c_{eq} with respect to calcite by Δc_{eq}.
- **Extended input of evenly distributed** CO_2 (Fig.3.21b): This scenario could refer to the case of microbial activity. If heterotrophic micro-organisms dwell on the walls of the fracture, they oxidize organic carbon constituents of karst water by aerobic metabolism and produce CO_2 along

the flow path of the water (Menne, 1998). The consequence is a linear increase[3] of c_{eq} within a part of the fracture where CO_2 input is evenly distributed. The increase of CO_2 concentration delivered by bacteria cannot exceed the concentration of O_2 in the water prior to conversion. The solubility of oxygen in the water is $11.3\,mg/l$ at 10^oC (Freeze and Cherry, 1979). Therefore a maximal increase of CO_2 is about $3.5 \cdot 10^{-7}\,mol/cm^3$. This corresponds to change of c_{eq} by $\Delta c_{eq} = 2 \cdot 10^{-7}\,mol/cm^3$ if c_{eq} prior to CO_2 delivery is $2\,\mu mol/cm^3$. Extended sources can also result from volcanic origin and may therefore exhibit a much larger Δc_{eq}.

3.4.1 POINT SOURCES OF CO_2

Let us suppose that a point CO_2 source is introduced into the karstifying fracture at some position $x_{in} = K \cdot L$, where $K \leq 1$.

The chemical picture of the scenario is presented on the Fig.3.21. The thick line presents the $CO_2 - Ca^{2+}$ equilibrium curve. See Fig.2.1 and the discussion in Chap.2 for more details. The solution enters into the fracture with some initial Ca^{2+} and CO_2 concentration represented by point A. The chemical pathway proceeds along the line A-CA until at point B' the concentration of CO_2 rises and dissolution proceeds along the parallel pathway B-CB. The net result of the CO_2 input with respect to our model is the change of the equilibrium concentration Δc_{eq}. Note that point A corresponds to the physical point $x = 0$ in the fracture and point B' to the point $x = KL$. In all the following model runs point B' is very close to the equilibrium curve. In summary: The dissolution rates for $x \leq x_{in}$ are determined by c_{eq_1}, the equilibrium concentration related to the CO_2-concentration of the inflowing water. At $x = x_{in}$ the equilibrium concentration increases due to the input of CO_2 to $c_{eq_2} = c_{eq_1} + \Delta c_{eq}$.

NUMERICAL RESULTS

To incorporate the above settings into the model of a single fracture we change c_{eq} in the rate equation according to:

$$c_{eq} = \begin{cases} c_{eq_1} & : \quad x < KL \\ c_{eq_2} & : \quad x \geq KL. \end{cases} \tag{3.58}$$

The new parameters describing this extended model are K and $\alpha = c_{eq_1}/c_{eq_2}$. We will focus our discussion on the effect of these two parameters on the breakthrough time. Fig.3.23a shows the evolution of flow rates for

[3] A linear incease is a good approximation for the small changes of c_{eq}. Generally the increase follows a cubic law as described in Sec.2.1

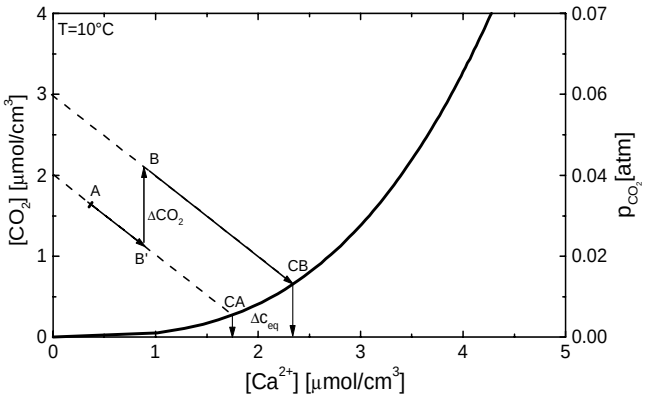

Figure 3.22: Chemical evolution of a $H_2O - CaCO_3 - CO_2$ solution flowing in a fracture under closed system conditions with respect to CO_2. The thick curve represents equilibrium with respect to calcite. See text for explanation.

various values of K for the standard fracture (see Tab.3.1 in Sec.3.1 for the basic parameters) and $\alpha = 0.91$ ($\Delta c_{eq} = 0.2 \mu mol/cm^3$). All curves exhibit the same behaviour with breakthrough times changing from 21.7ky at $K = 1$ (standard fracture) to a minimum value of 7.5ky at $K = 0.5$.

Fig.3.23b illustrates the dependence of the breakthrough time on K for various values of α. All curves exhibit a minimum which depends on α. Note that the breakthrough times at $K = 0$ are related to an inflowing solution with c_{eq_2}. Therefore these breakthrough times drop with increasing c_{eq_2} as $T_B = \alpha^{4/3} \cdot T_B^0$ (see Eq.3.34).

Fig.3.24a shows the T_B as a function of α for various values of K. In all cases there is a drastic drop of the breakthrough times in the region between $\alpha = 1$ and $\alpha \approx 0.9$. Two sets of curves are observed. For large K ($K > 0.7$) the breakthrough times drop up to a factor of two between $\alpha = 1$ and $\alpha = 0.975$ which corresponds to $\Delta c_{eq} = 0.05 \mu mol/cm^3$. Then only little variation is observed as α decreases. In contrary, for $K < 0.5$ the breakthrough times show a significant continuous decrease also at smaller values of α.

To explain this behaviour we focus on two representative cases. Fig.3.24b shows the dissolution rates along the fracture for $K = 0.25$ (dashed lines) and $K = 0.75$ (full lines) for various times of evolution. At the onset of karstification the dissolution rates exhibit a characteristic drop close to the entrance until they are boosted up at $x_{in} = KL$. Then the rates drop again.

For $K = 0.25$ the rates at the exit are considerably lower than at x_{in} at all times. This forms the bottleneck as shown by Fig.3.25a.

The situation becomes different for $K = 0.75$ (full lines). They first follow the rates as in the case of $K = 0.25$, and drop further until they are boosted up at $0.75L$. Now the rates at the exit are higher and the bottleneck

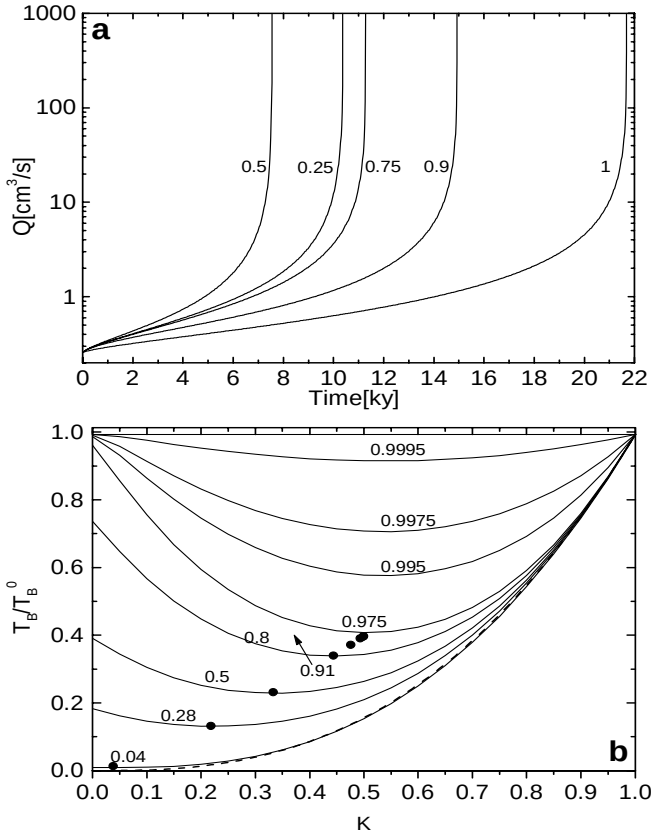

Figure 3.23: **a)** Evolution of flow rates for the standard fracture with a CO_2 input for various values of K (denoted on the curves). $\Delta c_{eq} = 0.2\,\mu mol/cm^3$. The curve for $K = 1$ corresponds to the standard fracture (see Tab.3.1). **b)** Dependence of T_B/T_B^0 on K for several values of α (denoted on the lines). Dots present the approximation given in Eq.3.64.

is at KL during the entire time span. This is shown by Fig.3.25b.

From the numerical results the following conclusions can be drawn:

- For any α, a K_{min} exists, where T_B is minimal. At K_{min} the rates at $x = KL$ and at $x = L$ are equal.

- In the region $K < K_{min}$, the bottleneck is at the end of the fracture: with increasing K, the rate there increases and the length of the bottleneck part $x > KL$ decreases. Thus the breakthrough time decreases in this region

- In the region $K > K_{min}$, the bottleneck is at KL, $F(KL)$ then decreases with increasing K, the length of the bottleneck part decreases, and consequently T_B increases.

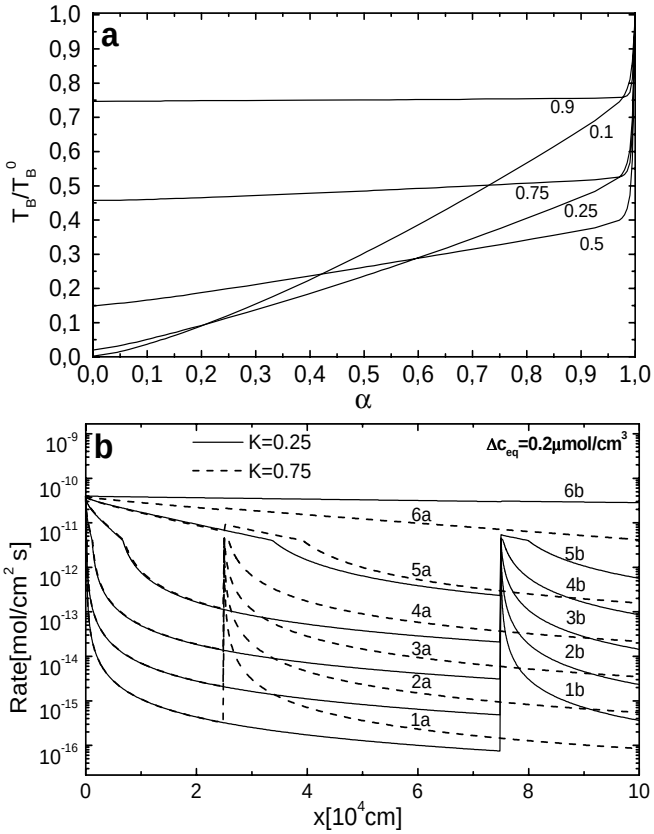

Figure 3.24: **a)** Breakthrough times as a function of α for various values of K as denoted on the curves. **b)** Dissolution rates for the point input: $\alpha = 0.91$, $K = 0.25$ (dashed lines) and $K = 0.75$ (full lines). For $K = 0.25$ profiles are recorded at 0.1, 6.3, 9.2, 10.11, 10.33, 10.37ky, marked by 1a-6a. For $K = 0.75$ profiles are recorded at 0.1, 6.93, 10.19, 11.07, 11.27 and 11.31ky, marked by 1b-6b.

ANALYTICAL ESTIMATION OF T_B

To give at least an approximate analytical results and to prove the above statements, we refer to the bottleneck principle. We use Eq.3.28 to obtain the rates at the both possible bottlenecks, i.e. at $x = KL$ and at $x = L$. The initial dissolution rate at the input of CO_2 is equal to:

$$F(KL)_{\downarrow} = F(c_s)\left(1 + \frac{KL}{\lambda_n(x_s)}\right)^{\frac{n}{1-n}}. \tag{3.59}$$

From numerical results we see that for most cases of interest the solution at $x = KL$ is close to c_{eq_1}, such that $c_{eq_1} - c(KL) << c_{eq_2} - c_{eq_1}$. This simplifies the rate after the CO_2 input to

$$F(KL)_{\uparrow} = k_n(1-\alpha)^n. \tag{3.60}$$

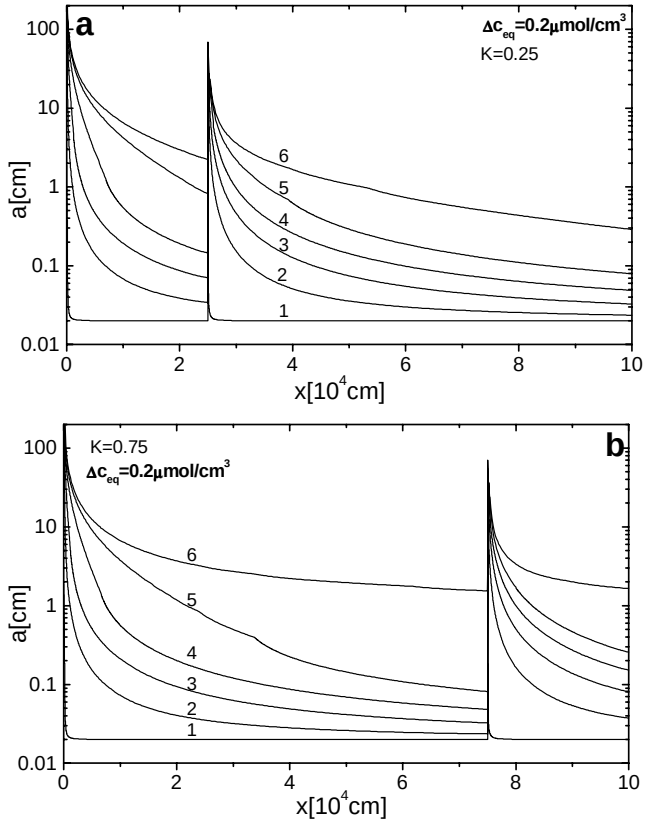

Figure 3.25: Evolution of aperture widths for the case from Fig. 3.24**a)** $K = 0.25$,**b** $K = 0.75$

$\downarrow$ and $\uparrow$ denote the rate at KL before and after the CO_2 input. Applying Eq.3.28 we obtain an estimation for the exit rate:

$$F(L) = k_n(1-\alpha)^n \left(1 + \frac{(1-K)L}{\lambda_n(KL)}\right)^{\frac{n}{1-n}}. \tag{3.61}$$

For convenience we define a new parameter $\tilde{\lambda}$ as

$$\tilde{\lambda} = \frac{\rho g h c_{eq_1} a_0^3}{24\eta L(n-1)k_n}, \tag{3.62}$$

so that the penetration lengths at x_s and $x = KL$ are (see also Eq.3.24):

$$\lambda_n(x_s) = \tilde{\lambda}(1 - c_s/c_{eq_1})^{1-n} \quad \text{and} \tag{3.63}$$
$$\lambda_n(KL) = \frac{\tilde{\lambda}}{\alpha}(1-\alpha)^{1-n}.$$

From $F(K_{min}L) = F(L)$ and neglecting the term "1" in Eqs.3.59 we get

$$K_{min} = \frac{\left(\frac{\tilde{\lambda}}{L}(1-\alpha)^{1-n} + \alpha\right)}{1+\alpha} \approx \frac{\alpha}{1+\alpha}. \tag{3.64}$$

The right side is valid if $(\tilde{\lambda}/L)(1-\alpha)^{1-n} << \alpha$ which also means $(1 - K)L/\lambda_n(KL) \gg 1$. Then K_{min} becomes independent of $\tilde{\lambda}/L$ and the breakthrough time can be expressed as

$$T_B^{min} = T_B^0 \cdot K_{min}^{n/(n-1)} = T_B^0 \left(\frac{\alpha}{1+\alpha}\right)^{n/n-1}. \tag{3.65}$$

Full circles on a Fig.3.23b mark this approximation. T_B^0 is the breakthrough time without CO_2 input given by Eq.3.34 in Sec.3.1. Note that T_B^{min} has the same functional dependence on basic parameters as T_B^0. The approximation is in a good accordance with the finite difference model for $\alpha \leq 0.91$. Then it fails, since the assumption does not hold anymore.

Another limiting case is when c_{eq_2} becomes so large, that the dissolution rates at the exit are sufficiently high and the last part of the fracture widens quickly in comparison to the first part. Therefore after a short time the hydraulic head acts only along the region $x \leq KL$. The breakthrough time can then be calculated by replacing L by KL and h/L by h/KL in Eq.3.34. In this case we obtain

$$T_B^{lim} = T_B^0 K^{\frac{2n}{n-1}}. \tag{3.66}$$

This result is presented by the lower dashed curve in Fig.3.23b. Finally for $K = 0$, the T_B dependence on α can be directly obtained from Eq.3.34 as $T_B^0 \alpha^{n/(n-1)}$.

In all three limiting cases, the dependence of T_B on the basic parameters (c.f. Sec.3.1) is, within the limit of our assumption, given by that of T_B^0. We can conclude, since all the equations solely contain the algebraic group $\tilde{\lambda}/L$, that this is also generally true and read T_B for all intermediate cases from Fig.3.23b if T_B^0 is known, provided $n = 4$. For other values of n similar graphs can be constructed. In the region between $n = 3$ and $n = 10$, not presented here, but checked, the deviations are not large.

3.4.2 EXTENDED SOURCES OF CO_2

We assume delivery of CO_2 by an evenly distributed population of microorganisms oxidizing organic carbon into CO_2. They deliver a constant rate of CO_2 as long as a sufficient amount of oxygen and organic matter is available.

NUMERICAL RESULTS

We model the situation by using a linear increase of c_{eq} in the rate equation:

$$c_{eq} = \begin{cases} c_{eq_1} + \frac{\Delta c_{eq}}{KL} x & : \quad x < KL \\ c_{eq_2} & : \quad x \geq KL \end{cases} \tag{3.67}$$

Additional parameters describing the extended model are now K and Δc_{eq}.

Fig. 3.26a shows the dependence of the breakthrough times on K for various values of Δc_{eq}. Other parameters correspond to the standard fracture with $c_{eq_1} = 2\mu mol/cm^3$. T_B decreases with increasing K.

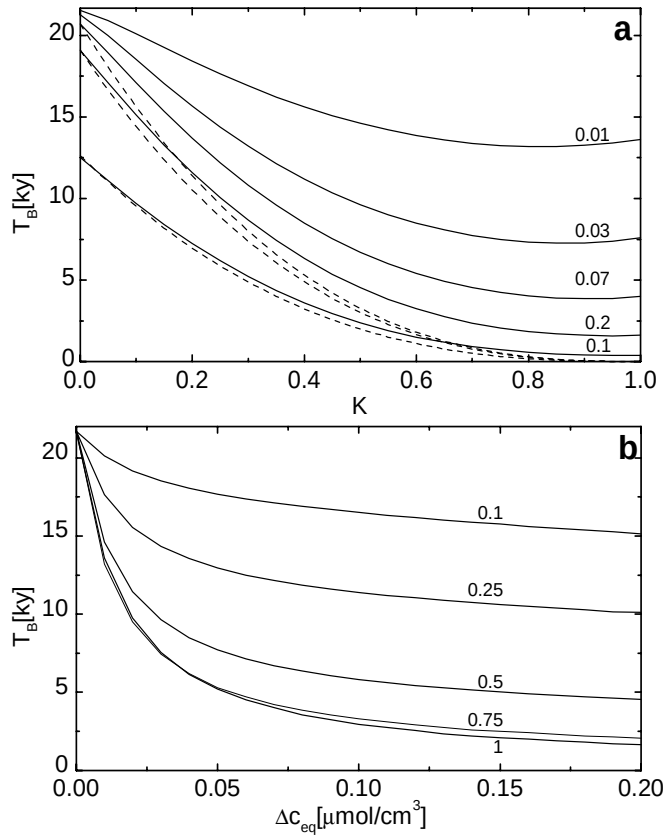

Figure 3.26: Efect of the extended sources of CO_2 on the breakthrough time of the standard fracture. **a)** T_B dependence on K for various values of $\Delta c_{eq}[\mu mol/cm^3]$ as denoted on the lines. The dashed lines show the approximation given by Eq.3.75 for $\Delta c_{eq} = 0.07\mu mol/cm^3$, $\Delta c_{eq} = 0.2\mu mol/cm^3$ and $\Delta c_{eq} = 1\mu mol/cm^3$ respectively. **b)** T_B dependence on Δc_{eq} for various values of K as denoted on the lines.

Fig. 3.26b shows the breakthrough times as a function of Δc_{eq} for various values of K (denoted at the curves). There is a steep decrease at

low Δc_{eq}. Most of the reduction occurs for $\Delta c_{eq} \leq 0.05 \mu mol/cm^3$. Thus when the organism dwell in the first half of the fracture ($K = 0.5$) and only about 25% of the maximum available oxygen ($11.3 mg/l$ at $10°C$) is converted to CO_2, the breakthrough time is reduced from 21.7 ky to 7.5 ky. If only 10% of O_2 is converted ($\Delta c_{eq} = 0.025 \mu mol/cm^3$) the reduction is still to 10 ky. Fig.3.27a shows the dissolution rates and the aperture widths along the fracture at several timesteps in the evolution. Again, the rates at the entrance drop steeply and then become constant. Beyond $x = KL$, c_{eq} is constant and the rates drop continuously according to Eq.3.20 as the solution moves towards the exit. Fig. 3.27b shows the corresponding profiles of the aperture widths. The bottleneck for the flow is located at the exit and therefore the widening there determines the breakthrough time.

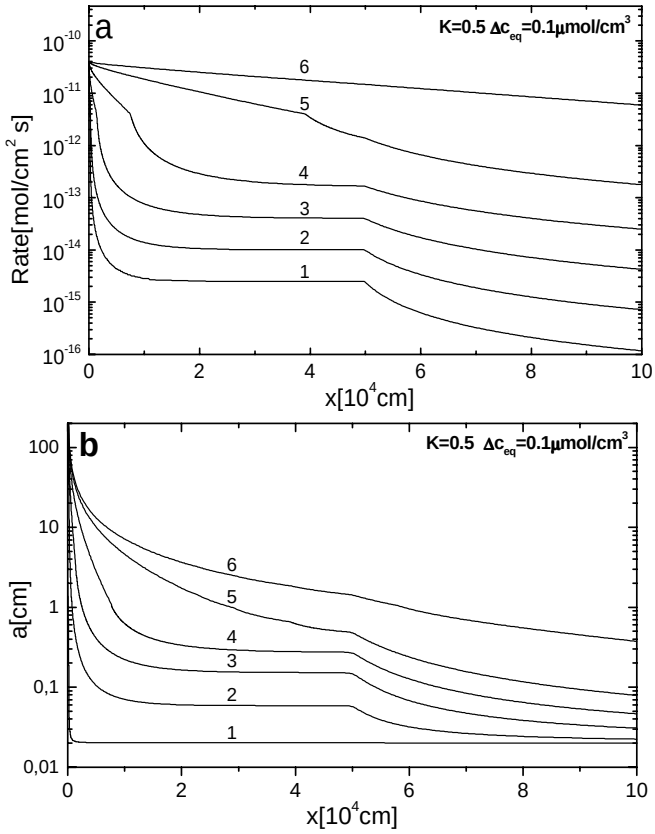

Figure 3.27: **a)** Profiles of the dissolution rates in standard fracture with extended CO_2 source at: 0.1, 3, 5, 5.6 5.82 and 5.83 ky, marked from 1-6. **b)** Evolution of fracture widths at the same time-steps.

ANALYTICAL APPROXIMATIONS

To understand this behaviour, we try to obtain some analytical approximations. The bottleneck forms always at the exit. The rate there can be obtained using Eqn.3.28 inserting KL and L for x_1 and x_2 respectively.

To calculate the rates at $x = KL$, one has to solve Eq.3.5 for the linear increase of c_{eq} as given in Eq.3.67. For convenience we introduce the variable $\Delta c(x) = c_{eq}(x) - c(x)$. Eq.3.5 then becomes

$$k_n \left(\frac{\Delta c(x)}{c_{eq}(x)}\right)^n P dx = Q\, d(c_{eq}(x) - \Delta c(x)) \tag{3.68}$$

We introduce $\kappa = \Delta c_{eq}/KL$ and rewrite the first part of Eq.3.67

$$c_{eq}(x) = c_{eq_1} + \kappa x = c_{eq_1}\left(1 + \frac{\kappa x}{c_{eq_1}}\right) \tag{3.69}$$

Inserting the upper expression into Eq.3.68 and reordering it we get:

$$\kappa - \frac{d\Delta c}{dx} = k_n \frac{P}{Q}\left(\frac{\Delta c}{c_{eq_1}(1 + \kappa x/c_{eq_1})}\right)^n. \tag{3.70}$$

The numerical results show, that for the cases of our interest $\kappa \gg d\Delta c/dx$, i.e. the variation of $\Delta c(x)$ is small compared to the rise of c_{eq}. Applying this in the upper equation gives:

$$\frac{\Delta c}{c_{eq_1}(1 + \kappa x/c_{eq_1})} = \frac{\Delta c}{c_{eq}(x)} = \left(\frac{Q\kappa}{k_n P}\right)^{1/n} = \left[\frac{1}{k_n} F(KL)\right]^{1/n}. \tag{3.71}$$

The rate at $x = KL$ can now be written as

$$F(KL) = \frac{\kappa Q}{P} = \frac{\Delta c_{eq} Q}{PKL}. \tag{3.72}$$

The result is somewhat surprising, since the rate does not depend on c_{eq_1}. This is also confirmed by numerical runs.

The exit rate can now be calculated by inserting the obtained $F(KL)$ into Eq.3.28. We obtain

$$F(L) = F(KL)\left[1 + \frac{(1-K)L}{\lambda_n(KL)}\right]^{\frac{n}{1-n}}, \text{where} \tag{3.73}$$

$$\lambda_n(KL) = \tilde{\lambda}\frac{c_{eq_2}}{c_{eq_1}}\left(\frac{F(KL)}{k_n}\right)^{(1-n)/n}. \tag{3.74}$$

We need to determine the range of the new parameters, where the enhancement of karstification is considerable. To do this we compare the initial dissolution rates $F(L,0)$ to the initial dissolution rates $F^0(L,0)$ (see Eq.3.31) for the fracture with no CO_2 input. As a criterion we choose $T_B/T_B^0 \approx 0.5$ and correspondingly $F(L,0)/F^0(L,0) \approx 2$. Therefore we

search for $\epsilon_{crit} = \Delta c_{eq}/c_{eq_1}$ where this criterion is achieved. For each K and $L/\tilde{\lambda}$ we obtain a value of Δc_{eq} where T_B is reduced to 1/2. The full lines on Fig.3.28 show the dependence of ϵ_{crit} on K for various values of $L/\tilde{\lambda}$ denoted at the corresponding curves. The lowest value of $L/\tilde{\lambda}$ corresponds to a fracture with $a_0 = 0.04cm, L = 10^4 cm, h/L = 0.05$, the highest value represents a fracture with $a_0 = 0.01cm, L = 10^6 cm, h/L = 0.01$. The middle curve is our standard fracture. Thus the entire region of natural karstification is covered. The four horizontal dashed lines present the maximal possible values of $\epsilon_{max} = \Delta c_{eq}^{max}/c_{eq_1}$ which can result from microorganisms when using up all the available oxygen. This causes an increase of the CO_2 concentration by $0.35\,\mu mol/cm^3$. The corresponding value of Δc_{eq}^{max} depends on c_{eq_1}; $\Delta c_{eq}^{max} = 0.32\,\mu mol/cm^3$ at $c_{eq_1} = 0.5\,\mu mol/cm^3$, $\Delta c_{eq}^{max} = 0.3\,\mu mol/cm^3$ at $c_{eq_1} = 1\,\mu mol/cm^3$, $\Delta c_{eq}^{max} = 0.2\,\mu mol/cm^3$ at $c_{eq_1} = 2\,\mu mol/cm^3$ and $\Delta c_{eq}^{max} = 0.1\,\mu mol/cm^3$ at $c_{eq_1} = 4\,\mu mol/cm^3$.

If the curves denoting ϵ_{crit} are above the corresponding lines representing ϵ_{max}, karstification is not significantly enhanced. On the other hand, if $\epsilon_{crit} < \epsilon_{max}$ a large enhancement is to be expected. From Fig. 3.28 one reads that a deep invasion of micro-organisms into the fracture is necessary. In view of the initial flow velocities of the water in the order of several metres/day, such deep invasion seems likely. For the standard case with $c_{eq_1} = 2\,\mu mol/cm^3$, $K > 0.4$ is required. If little external CO_2 is supplied from the surface, i.e., $c_{eq_1} = 0.5 - 1\,\mu mole/cm^3$, this value of K

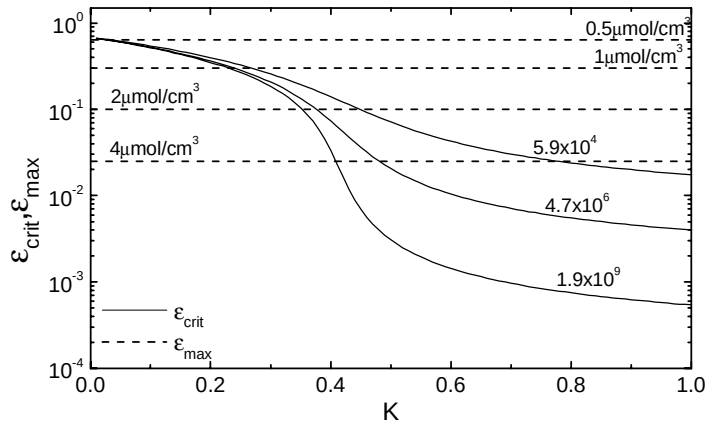

Figure 3.28: The full lines represent the value of $\Delta c_{eq}/c_{eq_1}$ where the breakthrough time of the fracture with the extended CO_2 source is reduced to half compared to the breakthrough time of the fracture with no extra CO_2. Numbers denote the value of $L/\tilde{\lambda}$ for the presented cases; the lowest value corresponds to a fracture with $a_0 = 0.04cm$, $L = 10^4 cm$, $h/L = 0.05$, the highest represents a fracture with $a_0 = 0.01cm$, $L = 10^6 cm$, $h/L = 0.01$ and the middle curve is our standard fracture. Dashed lines present the $\epsilon_{max} = \Delta c_{eq}^{max}/c_{eq}$ which can be delivered by microbial activity for four different values of c_{eq_1} as given on the lines. If a full line is below a certain dashed line means that the bacterial activity can reduce the "intrinsic" breakthrough time for more than one half.

is reduced and significant enhancement of karstification can arise solely by the activity of micro-organisms .

It is also possible to give an extreme limit of enhancement for each value of K. If Δc_{eq_1} becomes so large that the constant initial dissolution rate becomes very large compared to that of the same fracture with no CO_2 supply, karstification is entirely governed by the evolution of the last part of the fracture which represents the bottleneck for the flow. Then the hydraulic head acts entirely along that part, so that

$$T_B(K) = T_B^0(c_{eq_2}) \cdot (1-K)^{\frac{2n}{n-1}}, \tag{3.75}$$

$T_B^0(c_{eq_2})$ is the breakthrough time of the corresponding fracture with constant $c_{eq} = c_{eq_2}$. The lowest dashed curve in Fig. 3.26b represents this limit, for the standard fracture. It shows that bacterial activity can be sufficient to approach this limit closely. It should be noted that the approximation breaks down when K is close to 1. The two higher dashed curves show that for smaller values of Δc_{eq} significant deviations occur.

Fig.3.29a represents the dependence of T_B on Δc_{eq} for various values of L and K. . Three different lengths are presented; $L = 10^6\,cm$ by the full lines, $L = 10^5\,cm$ (standard fracture) by the dashed lines and $L = 10^3\,cm$ by the dotted lines. The values of K are denoted at the lines. Other parameters are "standard". It demonstrates clearly that for $L > 1\,km$ and $K > 0.5$ an increase of c_{eq} by $1\mu mol/cm^3$ is sufficient to reach the maximum of enhancement. For karstification along short fractures of about $100m$, however, biogenic CO_2 reduces the breakthrough time only to about one half. For low values of $K \approx 0.1$ no significant enhancement arises at all. This again shows that deep invasion of micro-organisms into the initial karst system is necessary.

THE REVERSE CASE: EXTENDED INPUT IN THE SECOND HALF OF THE FRACTURE

The full lines on Fig.3.29b present the dependence of T_B on K for various values of Δc_{eq} if the CO_2 is delivered in the second part of the fracture at $x \geq KL$. In this case $c_{eq} = c_{eq_1}$ for $x < KL$, and $c_{eq} = c_{eq_1} + \kappa(x - KL)$ for $x \geq KL$. The numbers on the curves denote $\Delta c_{eq}/c_{eq_1}$.

For comparison, the dashed lines present the results from Fig.3.26. When CO_2 is delivered for $x < KL$, the bottleneck is the exit part of the fracture. The breakthrough times in this case are some function of $(1-K)$. If, however, CO_2- supply is delivered at $x > KL$, than the part $x < KL$ represents the bottleneck and the breakthrough time is a similar function, but now of K. At $K \approx 0.5$ breakthrough times for both cases should not differ much. Moreover the corresponding curves should be mirror like, because breakthrough times should be close to each other if the lengths of the bottlenecks are equal for the two cases. As an example, breakthrough

time for some K for the case where CO_2 is delivered at $x < KL$, should be similar to the breakthrough time at $1 - K$ for the case where CO_2 is delivered at $x > KL$ since the lengths of the both bottlenecks are equal. This is nicely demonstrated by Fig. 3.29b and gives further support to the "bottleneck method" which we have used to analyse the numerical results.

So far we have assumed that microbiological oxidation of organic carbon increases with increasing flow through the fracture, such that the increase in c_{eq} is independent of the flow rate. This implies that the overwhelming bulk of bacteria is floating in the solution and their concentration is independent on flow rate. If, however, the bacteria are located at the fissure surfaces forming a biofilm and their rate of production is assumed to be constant,

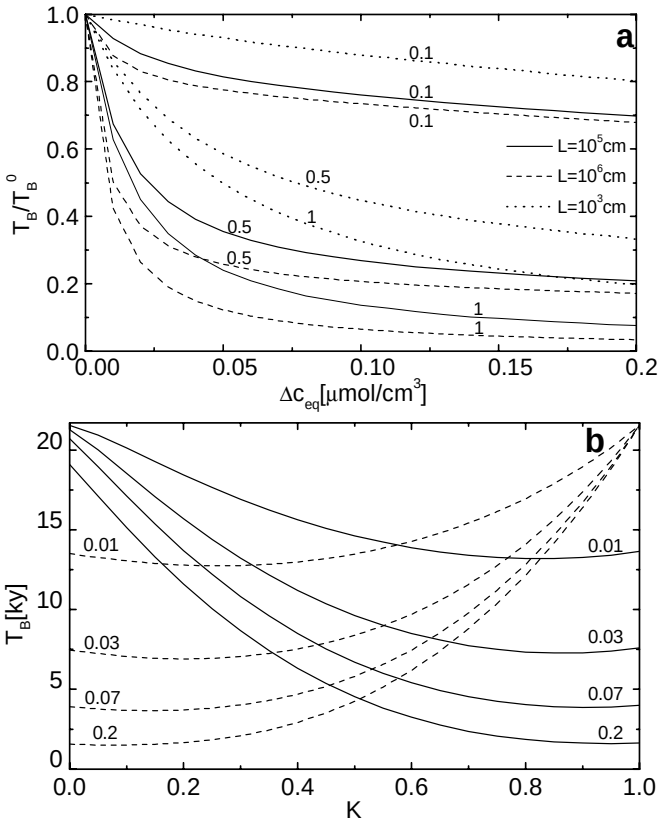

Figure 3.29: **a)** Breakthrough times for the standard fracture (full lines) and fractures with $L = 10^6 cm$ (dashed) and $L = 5 \cdot 10^3 cm$ (dotted) as a function of Δc_{eq}. The numbers on the curves denote K. The scale is in units of T_B^0, i.e. breakthrough times of the respective fractures without CO_2 supply. These are $0.32ky$, $21.7ky$ and $467ky$, for $L = 5 \cdot 10^3 cm$, $L = 10^5 cm$ and $L = 10^6 cm$ respectively. **b)** $T_B(K)$ for the values of $\Delta c_{eq}[\mu mol/cm^3]$ denoted at the lines. The dashed lines denote the case where the input is in the first part of fracture, same as in Fig.3.26a. The full lines represents the case, when CO_2 input starts at KL.

then the concentration of CO_2 decreases as the flow rate increases. If at time $t = 0$, $\Delta c_{eq}(0)$ is the increase in equilibrium concentration with respect to calcite at flow rate $Q(0)$, at later times t, $\Delta c_{eq}(t) = \Delta c_{eq}(0) \cdot Q_0/Q(t)$. This can be incorporated into the numerical model by employing $\Delta c_{eq}(t)$ in each time step. The results qualitatively resemble those of Fig.3.26, although the variations are less pronounced. One could envisage many

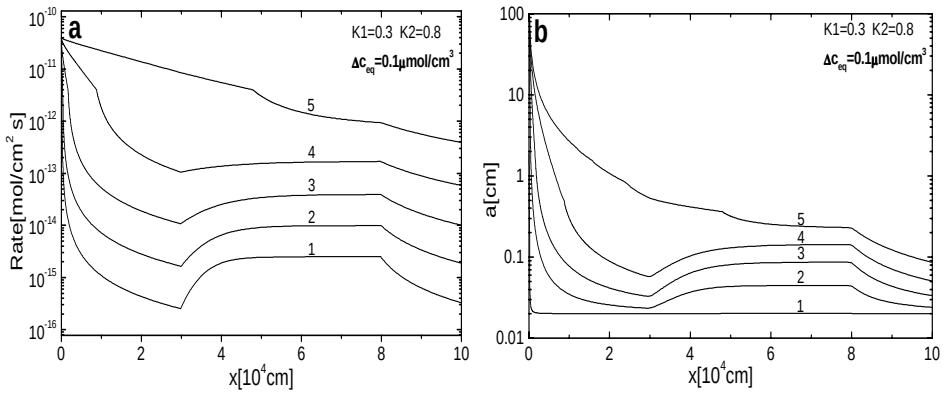

Figure 3.30: **a)** Profile of the dissolution rates in the standard fracture with extended CO_2 source between K_1L and K_2L, where $K_1 = 0.3$ and $K_2 = 0.8$. Profiles are recorded at: 0.1, 2.1, 2.95, 3.23, 3.4ky, marked from 1-6, respectively. **b)** Profiles of the aperture width at the same times.

different scenarios of CO_2 input into the karstifying fractures. As a final example we take the case, where CO_2 is supplied between $x_1 = K_1L$ and $x_2 = K_2L$, which causes a constant increase of c_{eq} in this region. For $x > K_2L$, c_{eq} remains constant. Fig.3.30 show the evolution of the dissolution rates and aperture widths for the standard fracture with $K_1 = 0.2, K_2 = 0.8, \Delta c_{eq} = 10^{-7}\, mol/cm^3$. After an abrupt drop close to the entrance the rates increase in the region where CO_2 is released, and then drop when approaching the exit. Breakthrough is reduced by a factor of almost 7 with respect to the T_B^0.

3.4.3 CONCLUSION

Subterranean sources of CO_2, either supplied at point inputs or continuously along a part of a karstifying fracture, cause a significant enhancement on early karstification. The reduction of breakthrough times depends on the amount of CO_2 supplied and on the position of the inputs.

For point inputs the highest reduction of breakthrough times is observed if the input is located near the center of the fracture. In this case a small increase of p_{CO_2} by about $2 \cdot 10^{-3}\, atm$ is enough to reduce breakthrough

times to about a half. If the input is close to the entrance, an increase of about $0.1\,atm$ is required for a significant reduction of breakthrough times. For inputs close to the exit of the fracture, even a large increase of p_{CO_2} affects breakthrough times only moderately. This values correspond for situations of vegetated karst with $c_{eq_1} \approx 2\mu mol/cm^3$. For bare karst areas with saturation of about $0.5 - 1\,\mu mol/cm^3$, the influence of CO_2 inputs is increased and lower values of additional CO_2 are needed to cause similar decrease of breakthrough times.

Continuous CO_2 input can arise from from extended diffuse gas migration from deep volcanic sources or from heterotrophic micro-organisms dwelling at the walls of the karstifying fractures. Micro-organisms can cause an increase of p_{CO_2} by about $6 \cdot 10^{-3}\,atm$. For natural karstification this is enough for a significant reduction of breakthrough times, provided the micro-organisms have invaded deep into the fracture, populating at least the first third of length. In this case the influence of CO_2 supply for bare karst areas is even more enhanced. The karstification can arise even if only atmospheric CO_2 is contained in the inflowing water.

3.5 THE ROLE OF MIXING CORROSION IN EARLY KARST EVOLUTION

3.5.1 BACKGROUND AND MODEL STRUCTURE

A BRIEF HYSTORY OF MIXING CORROSION: WHEN AND WHY ?

The chemical background of mixing corrosion has been already discussed in Sec.2.1. If two saturated solutions with different chemical compositions mix, the aggresivity can be renewed due to nonlinearity of the $Ca^{2+} - CO_2$ equilibrium curve. The closer to saturation the mixing solutions are, the higher is the shift of the aggressivity. Although mixing corrosion had been known before, its role in karst was first stressed by Bögli (1964), (1980) who suggested it as a possible cave forming mechanism.

Experiments by Weyl (1958) and Erga and Terjesen (1956) revealed a linear rate law for the dissolution kinetics of limestone in $H_2O - CO_2$ solution and therefore the evolution of extended karst conduits as observed in nature could not be explained by theoretical models (White and Longyear, 1992). Bögli suggested that caves could originate deep in the rock due to the mixing of saturated solutions. Mixing corrosion was also discussed by Dreybrodt (1981a) who showed that, owing to this mechanism, cave conduits can grow when two saturated solutions mix along an intersection of fractures. This model does not explain the fact pointed out by Ford and Ewers (1978), that most of the caves develop along bedding planes without any intersections by joints.

Mixing corrosion was put into the "back stage", after it was shown that the action of non-linear dissolution kinetics alone can generate extended karst conduits. In Sec.3.4 we have seen that due to the nonlinearity only a small change of parameters in the rate equation causes a large reduction of T_B. From the model point of view we can consider mixing corrosion as an extra source of CO_2 therefore we might expect it to cause a similar enhancement of early karstification.

MODEL STRUCTURE

To achieve mixing of two solutions, we have to leave the "easy-to-analyse" territory of single fracture models. Fig.3.31 shows the simplest case where mixing is possible: Two symmetric fractures joining into a third one. All have initial aperture widths a_0 and widths b_0. Fractures 1 and 2 join into fracture 3 at the distance kL from the entrance, where L is the total length of the system. At the confluence water is mixed completely. The hydraulic head at the entrances 1 and 2 is h. At the outflow the hydraulic head is set to zero.

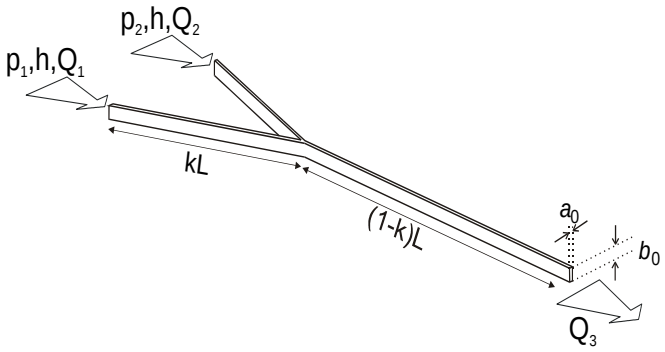

Figure 3.31: Symmetric confluence of two fractures. Conceptual model for the most simple scenario where mixing corrosion is active. p_1 and p_2 denote the p_{CO_2} of solutions at the entrances of the fractures which join at the position kL.

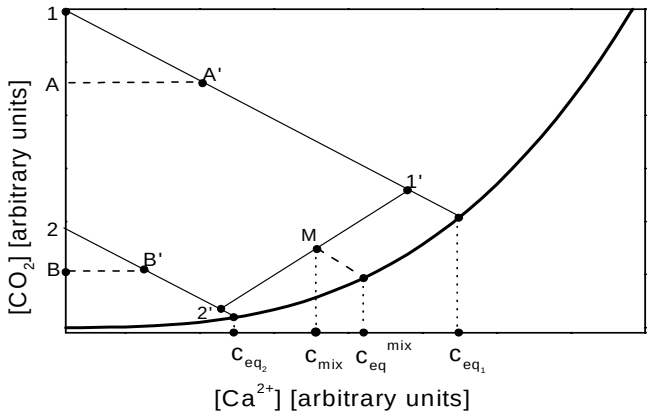

Figure 3.32: Chemical scenario of mixing corrosion. See text for explanations.

Fig.3.32 shows the chemical evolution of the solution in fractures 1 and 2 with respect to CO_2 and Ca^{2+}. The solution enters at points 1 and 2 with $[Ca^{2+}] = 0$ and different concentrations of CO_2 corresponding to equilibrium with p_1 and p_2 respectively. The evolution of solutions within the fractures is illustrated by the full lines. Points 1' and 2' depict the chemical composition at the exits of both fractures. Point M shows the concentration c_{mix} after immediate complete mixing at the confluence. The equilibrium is given by the intersection of the dashed line representing dissolution by the mixed solution in fracture 3 under closed conditions and the $CO_2 - Ca^{2+}$ equilibrium curve (fat line).

Another scenario is also possible. Assume that both soils exhibit different soil structures and contain calcite. In that case water seeping down will dissolve calcite under open system conditions designated by the dashed lines BB' and AA' until at points A' and B', respectively, it enters into the fractures. From then on it dissolves limestone under closed system con-

ditions. This leads to the same amount of undersaturation as in the first scenario given above. Even if points A and B coincide, this last scenario allows mixing corrosion.

To calculate the evolution of fracture widths, we use the following procedure:

1. Calculate the resistance of each fracture and the head h_j at the junction according to
$$h_j = h\frac{R_1R_3 + R_2R_3}{R_1R_2 + R_1R_3 + R_2R_3}, \tag{3.76}$$
where R_1, R_2 and R_2 are the resistances of the three fractures calculated by Eq.3.2.
2. Apply the transport-dissolution model (see Sec.3.1) and calculate the widening and chemical evolution of fractures 1 and 2.
3. Calculate the concentration c_{mix} entering into fracture 3 assuming complete mixing,i.e.
$$c_{mix} = \left(Q_1c_1^j + Q_2c_2^j\right)/(Q_1 + Q_2), \tag{3.77}$$
where c_1^j and c_2^j are the concentrations in the fractures 1 and 2 at the confluence.
4. Calculate the widening of the fracture 3.
5. Repeat steps 1.-3. until the onset of turbulence.

3.5.2 NUMERICAL RESULTS AND DISCUSSION

MODEL PARAMETERS

Following parameters were used in the runs that follow: $a_i(t = 0) = 0.02\,cm$, $b_i(t = 0) = 100\,cm$ for $i = 1, 2, 3$. $h = 5000\,cm$, $p_1 = 0.05\,atm$ and p_2 is in the range of $0.003\,atm$ to $0.05\,atm$. Kinetic constant and order is the same as in the standard fracture: $k_1 = 4 \cdot 10^{-11}\,mol\,cm^{-2}s^{-1}$, $k_n = 4 \cdot 10^{-8}\,mol\,cm^{-2}s^{-1}$, $c_s = 0.9c_{eq}$, $n = 4$.

Note: from here on the expression "Mixing Corrosion" will be abbreviated as MC.

LINEAR KINETICS WITH MC VS. NONLINEAR KINETICS WITHOUT MC

We start with the results of Böglis concept of MC presented in Fig.3.33, where dissolution rates are defined only by the linear kinetics. It shows the aperture widths of fractures 1 and 3, as they develop in time for $p_1 = 0.05\,atm$ and $p_2 = 0.003\,atm$. Due to the exponential decrease of dissolution

rates, fracture 1 opens at the entrance and the dissolution front progresses very slowly. Mixing corrosion causes opening at the junction, but has only

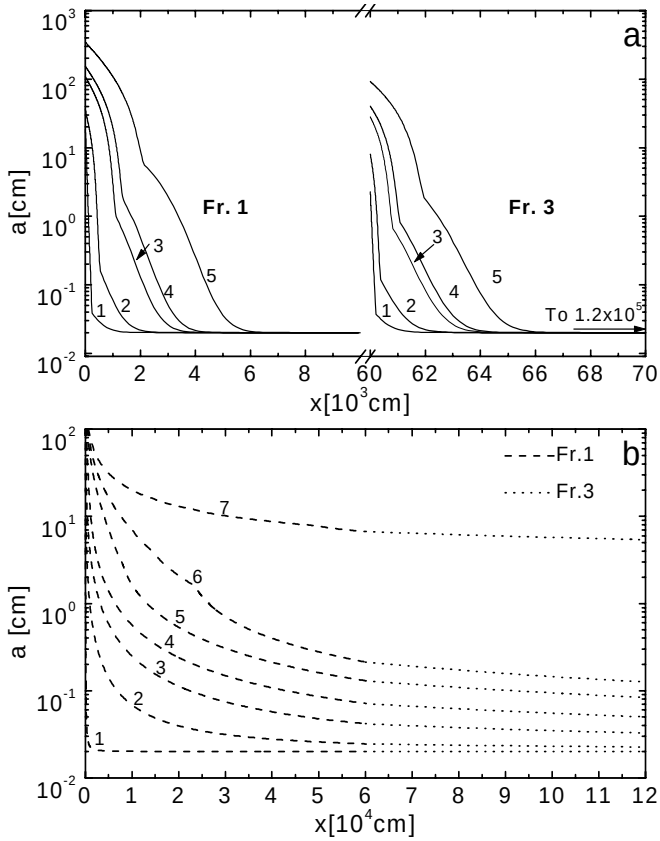

Figure 3.33: **a)** Profiles of fracture 1 and 3 if only linear kinetics is operative. Profiles are recorded at 0.2, 2, 20, 40 and 400 ky, marked from 1-5 respectively. $k = 0.5$, $p_1 = 0.05\,atm$, $p_2 = 0.003\,atm$. Note a break in the x-axis. **b)** Same settings with $p_1 = p_2 = 0.05\,atm$. No MC, but non-linear kinetics is active. Profiles at 0.1, 23.9, 48.6, 55.2, 56.9, 57.2 and 57.4 ky, marked by 1-7.

a local importance. There is no breakthrough in a geologically relevant time. Fig.3.33b shows the evolution of the aperture widths when no MC is present, i.e. $p_1 = p_2 = 0.05$, but nonlinear dissolution rates are assumed. All other parameters are unchanged. It depicts the profiles of all three fractures. Note that fractures 1 and 2 are equal due to the symmetry of the settings . The behaviour is, as expected, very similar to that shown in the previous sections. Breakthrough is achieved after 57ky.

NONLINEAR KINETICS WITH MC

As shown MC is not necessary for speleogenesis. But is it important?

In the next step we combine MC ($p_1 = 0.05\,atm$ and $p_2 = 0.03\,atm$) and non-linear dissolution rates. The aperture widths for the three fractures are shown by Fig.3.34a. Due to the larger p_1 and correspondingly a larger c^1_{eq},

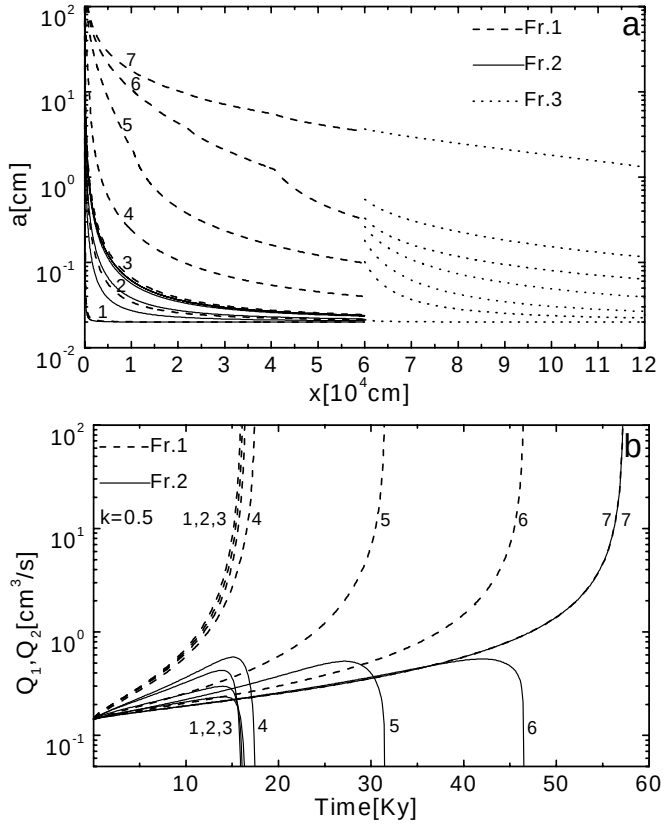

Figure 3.34: **a)** Profiles of aperture widths for $p_1 = 0.05\,atm$ and $p_2 = 0.03\,atm$. Breakthrough occurs at 17.6ky. Profiles are taken at: 0.1, 6.3, 11.3, 15.8, 17.2, 17.5, and 17.6ky, marked by 1-7. **b)** Flow rates through fracture 1 (dotted lines) and fracture 2 (full lines) as a function of time for $p_1 = 0.05\,atm$ and $p_2 = 0.003$, 0.01, 0.02, 0.03, 0.04, 0.045, 0.05 atm marked by 1-7.

the widths in fracture 1 increase by far faster than those in fracture 2. Thus the resistance of fracture 1 decreases more rapidly. Consequently the head at the confluence rises (see also eq. 3.76) causing reduced flow rates in fracture 2 compared to those in fracture 1. Therefore dissolution rates at the exit of fracture 2 remain low, and the restriction of this fracture is maintained. At the confluence MC boosts the dissolution rates. Breakthrough occurs at 17ky, less than one third of the value without MC.

To elucidate the processes underlying conduit genesis by the combined action of MC and nonlinear kinetics Fig.3.34b presents the flow rates Q_1 and Q_2 through the fractures 1 and 2 for $p_1 = 0.05\,atm$ and various values of p_2 in the range from $0.003\,atm$ up to $0.05\,atm$. In all cases Q_1 shows a slow increase until it is drastically enhanced at breakthrough. Q_2 exhibits a different pattern. The flow rate increases initially , but the rincrease is suppressed by the rising head at the junction due to the relatively fast widening of fracture 1. Shortly before breakthrough the resistance of frac-

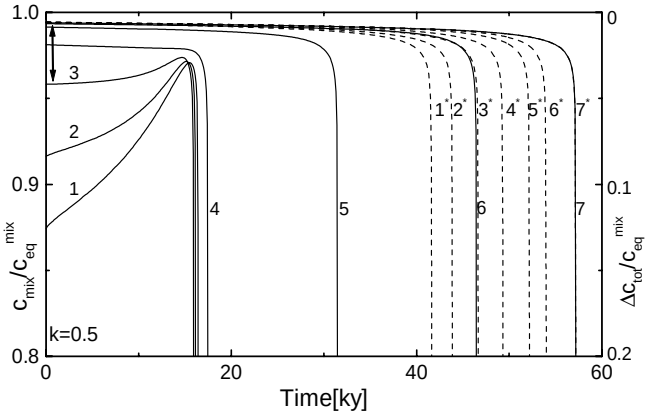

Figure 3.35: Evolution c_{mix}/c_{eq}^{mix} in time for the same parameters as in Fig.3.34. Dashed lines 1*-7* depict the corresponding curves when MC is switched off numerically.

ture 1 drops to such low values that the hydraulic head at the junction approaches the head at the entrance of fracture 1. Therefore the head difference and consequently the flow rate along fracture 2 decrease until they become zero. In the symmetric case, where $p_2 = p_1$, both fractures behave in the same way and both exhibit breakthrough (cf. curve 7).

In the case where $p_1 > p_2$, Q_1 increases more rapidly than Q_2, therefore the effect of MC decreases until at breakthrough it is switched off completely. This is visualized by Fig.3.35 which shows the saturation ratio of the mixed solution (c_{mix}/c_{eq}^{mix}) at the confluence as a function of time. Values of p_2 are as in Fig.3.34b . For curves 1-3 with $p_2 < 0.03\,atm$ this ratio increases in time until a drastic drop at the breakthrough is observed. It is interesting to note that for $p_2 < 0.03\,atm$ the values of T_B are almost equal. A second regime is exhibited for $p_2 > 0.03\,atm$. In this region the ratio c_{mix}/c_{eq}^{mix} is only slightly dependent on p_2 and decreases slowly in time until it drops to zero at breakthrough. The value of T_B increases with p_2. Curve 7 with $p_2 = 0.05\,atm$ presents the case without MC.

CHEMICAL EVOLUTION OF THE SOLUTION IN FRACTURES

To obtain more insight into the mechanisms of this behavior, we discuss the chemical composition of the solution at the confluence. Fig. 3.36 illustrates the pathways of the chemical evolution. Chemical pathways of the solutions in fractures 1 and 2 (closed system) are represented by the lines through AA_{eq} and BB_{eq} respectively. gh M_0M depicts the evolution of the concentrations at the entrance of the fracture 3. The fat line depicts the CO_2-Ca^{2+} equilibrium. Points A,B and M characterize the concentrations of Ca^{2+} and CO_2 at arbitrary time t. A and B refer to the solutions at the exits of fractures 1 and 2, M refers to the mixed solution at the entrance of fracture 3. Point D gives the average concentration of two fully saturated solutions at the exit of fractures 1 and 2, denoted by points B_{eq} and A_{eq}. Point M_{eq} gives the equilibrium composition of the solution entering fracture 3. The subscript 0 at those points indicates the composition at time zero.

The total undersaturation of the mixed solution with respect to Ca^{2+} is Δc_{tot} as shown in the figure. It consists of two contributions, Δc_{mix} and Δc_{eq} . Δc_{mix} results from mixing of the two undersaturated solutions (points A and B) in the diagram. It becomes zero if both solutions are saturated. Δc_{eq} gives the undersaturation by MC due to the curvature of the CO_2-Ca^{2+} equilibrium curve. Δc_A and Δc_B are the saturation deficits of the solutions at the exit of fractures 1 and 2.

During the evolution of the fractures, Q_1 increases and therefore point A moves to lower calcium concentrations. As long as Q_2 increases B moves into the same direction, which is reversed as soon as Q_2 starts to decrease. As a consequence point M moves along the curve M_0M. As the ratio Q_1/Q_2

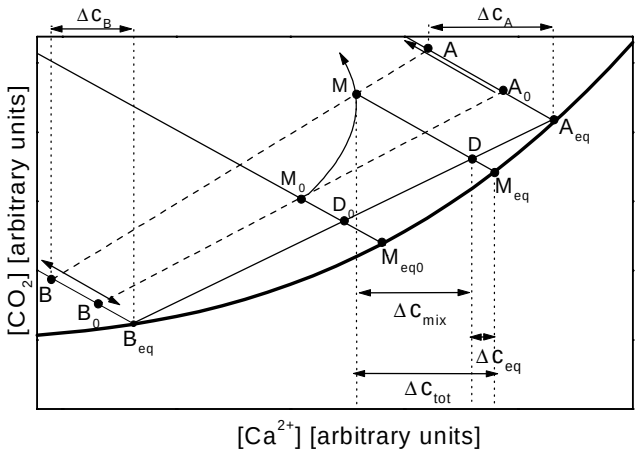

Figure 3.36: Chemical evolution of the solution at the exits of the fracture 1 (point A) and 2 (point B) and at the confluence (point M) after complete mixing. See text.

increases in time, point M_{eq} moves towards A_{eq} . Then Δc_{eq} approaches zero and MC is switched off.

From Fig.3.35 we can now read the value $\Delta c_{tot}/c_{eq}^{mix}$, where c_{eq}^{mix} refers to the saturation at point M_{eq}. This is indicated on the right vertical axis. Note that $c_{mix}/c_{eq}^{mix} = 1 - \Delta c_{tot}/c_{eq}^{mix}$. For curve 7, where $p_1 = p_2$, Δc_{eq} is zero during the entire evolution. Therefore $\Delta c_{tot} = \Delta c_{mix}$. At time zero Δc_{mix} of all other curves must be smaller, since Δc_B decreases with decreasing p_2. Furthermore Δc_{mix} is a continuously increasing function in time. The difference between curves 1-6 to curve 7 represents the corresponding value Δc_{eq} for each of these curves in a reasonable approximation. This, as an example, is indicated by an arrow at curve 3. For curves 1-3, Δc_{eq} is initially much larger than Δc_{mix} . Due to the increasing ratio of Q_1/Q_2 during the evolution of the fracture, $\Delta c_{eq}/c_{eq}^{mix}$ decreases and consequently the curves rise. This is opposed by the increase in $\Delta c_{mix}/c_{eq}^{mix}$, which takes the value of 1 at breakthrough. Therefore a maximum occurs close to breakthrough. In curve 4 the rise in Δc_{mix} cancels the decay of Δc_{eq} , such that Δc_{tot} remains constant during most of the time until breakthrough. For curves 5 and 6 Δc_{eq} is much smaller than Δc_{mix}. Therefore Δc_{tot} increases in time.

To visualize the effect of Δc_{eq} to the T_B we have also calculated the breakthrough behaviour, when MC is switched off, by fixing Δc_{eq} numerically to zero and retaining only Δc_{mix} as contribution to Δc_{tot}. The dashed lines in Fig.3.36, marked from 1* to 7* corresponding to lines 1-7 respectively, present the results. From these it can be seen that for curves 1-4 MC has a significant effect to the reduction of T_B. For curves 5 and 6, although $\Delta c_{eq} < \Delta c_{mix}$, the reduction in T_B is still remarkable. Curves 7 and 7* are identical since $\Delta c_{eq} = 0$ in any case.

3.5.3 THE REDUCTION OF THE BREAKTHROUGH TIME DUE TO THE MC

To answer the question, why does T_B stay constant for $p_2 < 0.03\,atm$, we have calculated T_B as a function of k, whereby L has been kept to $1.2{\cdot}10^5\,cm$. Fig.3.37 shows the results for the various values of p_2 . For $p_2 < 0.03\,atm$ the curves are crowded to a small region and exhibit a minimum close to $k \approx 0.5$. For $p_2 > 0.03\,atm$, T_B increases and for $p_2 > 0.04\,atm$ a maximum arises. The upmost curve represents $T_B(k)$ for $p_2 = p_1$. We have also calculated T_B for $p_1 = 0.07\,atm$, varying p_2 from 0.03 to 0.07 atm, and for $p_1 = 0.03\,atm$ with p_2 from 0.03 to 0.003 atm, and have found a similar behaviour. To elucidate the reason for the limit in the reduction of T_B, Fig.3.38a shows the evolution of the aperture widths in time for a junction with $k = 0.0167$ for $p_1 = 0.05\,atm$ and $p_2 = 0.03atm$. As can be easily visualized fracture 1 opens up quickly in time such that its flow resistance

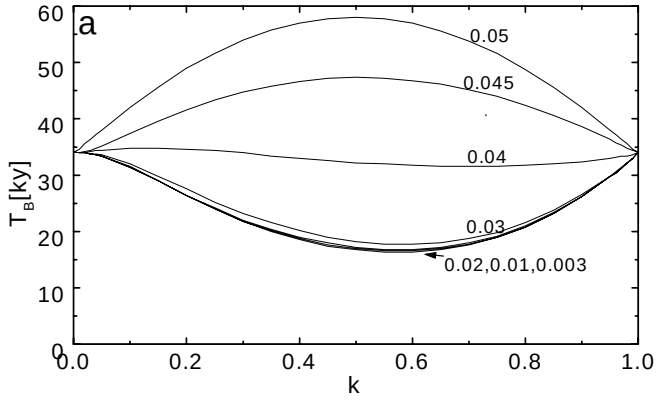

Figure 3.37: Breakthrough time as a function of k. $p_1 = 0.05atm$, value of p_2 are denoted on the curves.

becomes small against that of fracture 3, which still retains its bottleneck at the exit. Fracture 2 due to the lower p_{CO_2} also retains its high resistance. As a consequence the flow rates in this fracture drop quickly.

This is shown by the corresponding curves in Fig.3.39a, which illustrate the flow Q_1 and Q_2 as a function of time for various p_2 . After about 10 thousand years the ratio Q_1/Q_2 has dropped to about 0.1. Therefore at that time MC is switched off almost completely. Due to the decreasing value of Q_2 the dissolution rates in fracture 2 drop and its aperture widths remain restricted . Fracture 1, however, opens quickly. Therefore the T_B is determined entirely by the evolution of fractures 1 and 3 which experience dissolution rates independent of p_2 during most of their evolution time. Consequently T_B becomes independent on p_2.

In contrast if p_2 approaches p_1 (i.e. $p_2 > 0.03atm$) the effect of MC becomes small, since $\Delta c_{eq} < \Delta c_{mix}$. Furthermore fracture 2 opens up more quickly, such that the ratio Q_1/Q_2 drops less rapidly, until it remains constant when $p_1 = p_2$. Nevertheless, the increase of dissolution rates by the action of Δc_{eq} is sufficient to exert a significant influence to the T_B. Fig.3.39b shows c_{mix}/c_{eq}^{mix} as a function of time for the various p_2. The curves for $p_2 \leq 0.03atm$ (curves 1-3) show a steep rise until MC is switched off and from then on a plateau until breakthrough occurs.

The behaviour exhibited by Fig.3.37 for $k \leq 0.5$ is independent on p_1. Therefore the same behaviour is expected, e.g. for $p_1 = 0.07atm$ and p_2-values from 0.003 to 0.07atm. As has been mentioned above this was verified by computer simulations. If k increases the length of the restricted exit fracture 3 decreases and as long as the entrance fracture 1 is sufficiently wide T_B decreases.

The situation becomes different for large values of $k > 0.5$. As an example Fig.3.38b illustrates the evolution of the aperture widths for $k = 0.833$ and other parameters as in Fig.3.38a. In contrast to what we have

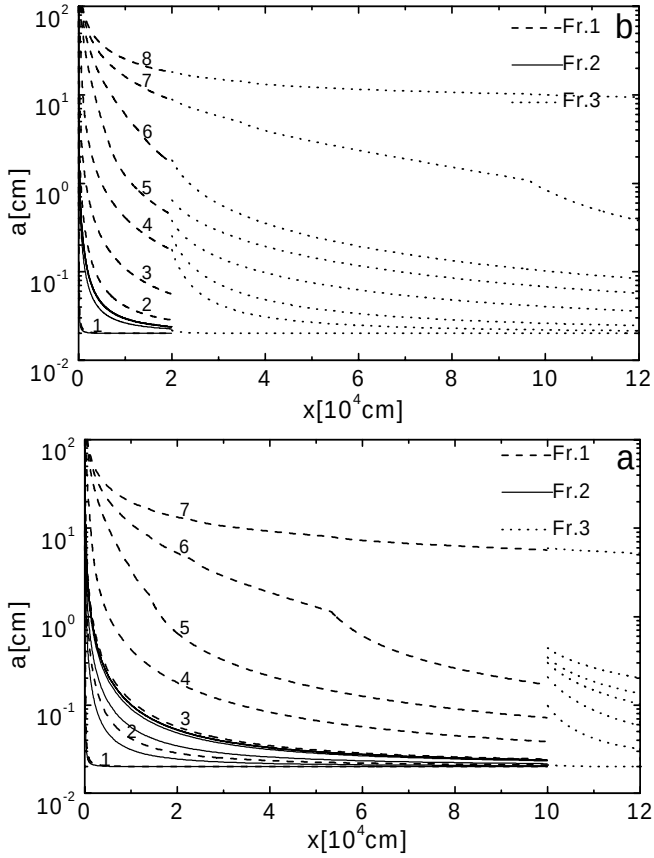

Figure 3.38: **a)** Profiles of aperture width for the junction with $k = 0.167$, $P_1 = 0.05atm$ and $p_2 = 0.03atm$. Profiles are taken at 0.1, 9.6, 17.8, 25.7, 27.8, 28.2, 28.4 and 28.5ky marked by 1-8, respectively. **b)** Parameters as in figure a, but $k = 0.833$. Profiles at 0.1, 6.6, 14.5, 20.8, 22, 22.2 and 23.3 marked by 1-7, respectively.

observed above, now the fracture 3 opens first, and fractures 1 and 2 both remain restricted during almost the entire time until breakthrough.

As long as p_2 is sufficiently small, T_B is therefore determined by dissolution in fracture 1, independent of p_2. For sufficiently large p_2, however both Δc_{mix} and Δc_{eq} determine T_B which rise until $\Delta c_{eq} = 0$, i.e. $p_1 = p_2$. The behaviour of c_{mix}/c_{eq}^{mix} and Q_1, Q_2 as functions of time resembles very much that with $k = 0.5$ as plotted in Fig.3.35 and 3.39b and is therefore not shown.

The essential result of our model calculations so far is condensed in Fig.3.37. The upper curve depicts the T_B with equal p of both inflowing solutions as a function of k. Therefore MC is absent. $k = 0$ and $k = 1$ relate either a single fracture or two identical isolated fractures respectively. Therefore the T_B are equal for both k. For each value of $0 < k < 1$, the T_B

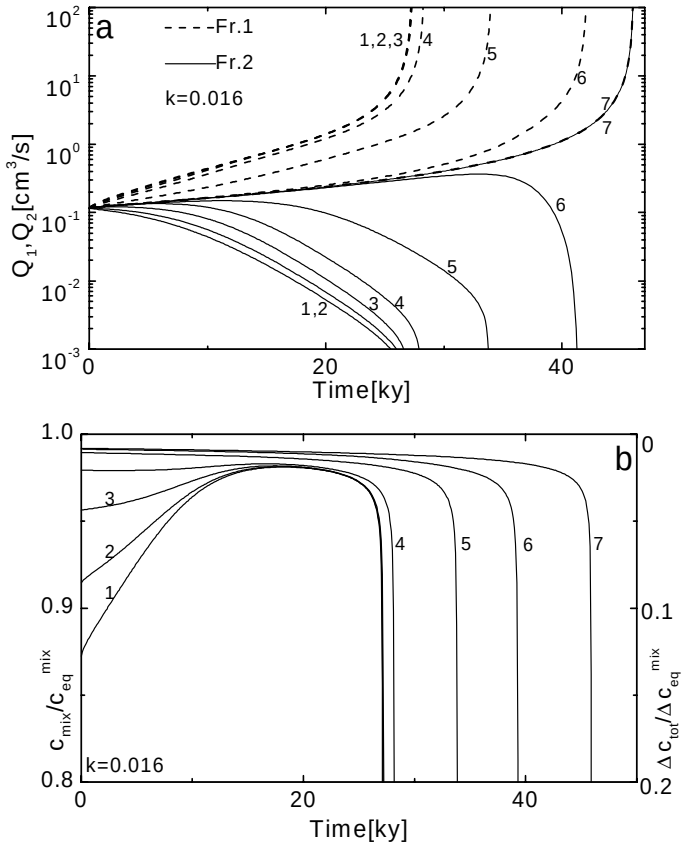

Figure 3.39: **a)** Flow rates Q_q and Q_2 as a function of time for $p_1 = 0.05atm$ and various p_2 as in Fig.3.34. Other parameters are the same as in Fig.3.38. **b)** Evolution of c_{mix}/c_{eq}^{mix} as a function of time for the same setting as in figure a.

must be higher, because the initial flow rates through each of the entrance fractures are lower than that through the isolated fracture. Due to the higher concentration of Ca^{2+} at the confluence the dissolution rates are lower than in the isolated fractures. Only a slight reduction of p_2 to about $0.04atm$ is sufficient to reduce T_B significantly. A limit of reduction is achieved for $p_2 = 0.03atm$ and further decrease of p_2 has no effect.

3.5.4 ASYMMETRIC CONFLUENCE

The symmetric arrangement depicted by Fig. 3.31 is not very likely in a natural setting. First the heads at the entrances 1 and 2 can be different, and furthermore also the length and aperture widths of the fractures cause

different flow resistances. The flow through the fracture 2 is given by

$$Q_2 = \frac{R_3(h_2 - h_1) + R_1 h_2}{R_1 R_2 + R_2 R_3 + R_1 R_3}. \tag{3.78}$$

Q_1 is found by interchanging the subscripts 1 and 2. In the following we assume $h_1 > h_2$ and $p_1 > p_2$. Therefore Q_1 is positive, i.e. it is directed towards the confluence. For Q_2 three cases are possible as can be read from eq.3.78:

1. $Q_2 > 0$ when $\|h_2 - h_1\| R_3 < h_2 R_1$
2. $Q_2 = 0$ when $\|h_2 - h_1\| R_3 = h_2 R_1$
3. $Q_2 < 0$ when $\|h_2 - h_1\| R_3 > h_2 R_1$

These conditions are independent on the resistance R_2. Now depending on the evolution of the aperture widths, the following scenarios arise:

- Initially condition 1 is valid and remains so until breakthrough. Then both flows are directed towards the confluence. At breakthrough the resistance of the winning path along fractures 1 and 3 drops close to zero ($R_1 \approx R_3 \approx 0$) and consequently the ratio Q_2/Q_1 becomes zero. MC is operative, until $Q_2/Q_1 > 0.1$.
- Initially condition 1 is valid. But as fractures 1 and 3 open up condition 3 is achieved. As soon as that happens Q_2 changes its flow direction. Then MC is no longer effective, and depending on the values of R_2 breakthrough occurs first via fracture 3 or fracture 2 solely by the action of nonlinear kinetics.
- Condition 3 holds at $t = 0$. Then MC is not active from the very beginning. Since under the action of nonlinear kinetics fracture 1 opens more quickly than fractures 2 and 3 the condition 3 remains valid and breakthrough occurs either via fracture 2 or 3.

If three fractures with entrance heads h join to a confluence into fracture 4 with head $h = 0$ at its exit, similar situations arise. Q_1 is always positive, assuring $p_1 = max(p_i)$. Depending on the initial values of the fracture resistances R_1, R_2, R_3, R_4 and their evolution in time Q_2 and Q_3 can take both flow directions, either towards the confluence or opposite. If Q_2 and Q_3 are positive, mixing of three solutions activates MC at the entrance of fracture 3. If $Q_2 > 0$ and $Q_3 < 0$ or vice versa two solutions mix and MC is active in fracture 4 and fractures 3 or 2, respectively. If both Q_2 and Q_3 are negative higher order kinetics determine exclusively the evolution of all aperture widths. Depending on the resistances, the p_{CO_2} , and the heads acting, breakthrough can occur along each combination of two of the four fractures. Thus, there is always a winning pathway which does not only depend on the geological setting (resistances and heads) but also on the chemical compositions of the inflowing solutions. All these possibilities exist also in two-dimensional networks, which we present in Sec. 4.2.3.

3.5.5 CONCLUSION

Variations of p_{CO_2} in the soil of the catchment area, different pathways of solutions in the vadose zone, different soil structures etc., can cause different chemical compositions of solutions entering the closed system, and upon their mixing they affect mixing corrosion. As shown, mixing corrosion can play an important role in the early karstification. A study on a simple junction presented here showed that not a large variation in p_{CO_2} is needed for mixing corrosion to produce large reductions of breakthrough times of the evolving conduits. It was shown that the reduction of breakthrough time depends on the location of confluence and is largest at $k = 0.5$ (see Fig.3.31) . The reduction also increases with decreasing p_2 and becomes constant for $p_2 < 0.5\, p_1$.

When discussing early karstification one also has to consider the geochemical settings such as distribution of CO_2 in the soil and the soil structure. Although MC is not a crucial factor for cave development it plays an important role in the early stage of cave evolution.

3.6 EVOLUTION OF A SINGLE FRACTURE WITH CONSTANT RECHARGE

So far we have assumed a constant head driving the water through the fracture. In this section we discuss another important element of more complex settings, a fracture with a constant recharge. All the scenarios and settings presented so far for the fracture with constant head, can also be applied to the fracture with constant recharge. This is not the aim of this section. Our goal is to present some very basic results which are new with respect to what has been shown so far.

3.6.1 MODEL STRUCTURE

Fig. 3.40 shows the concept: a constant recharge $dQ/dx = q$, with calcium concentration c_{in} is introduced along the fracture. Prior to the recharge region, the fracture carries initial flow Q_0 with concentration c_0.

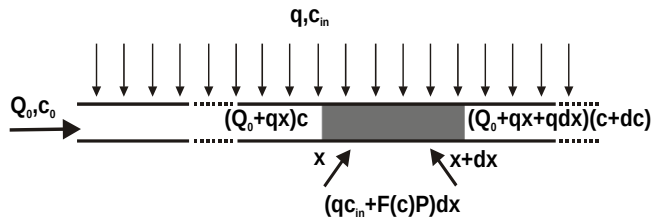

Figure 3.40: Basic parameters and mass conservation between x and $x + dx$ in a single fracture with a constant recharge.

3.6.2 NUMERICAL RESULTS

To obtain numerical results we proceed as in the fracture with constant head conditions. But we use an adapted mass conservation equation. Instead of Eq.3.5, the conservation of Ca^{2+} ions now demands:

$$(Q_0 + qx)c + F(c)Pdx + c_{in}qdx = (Q_0 + qx + qdx)(c + dc). \tag{3.79}$$

The numerical algorithm used in this case is slightly different to the one used so far. The concentration changes due to the dissolution and to the mixing with the inflowing water. Therefore, if $c(x)$ is the concentration at

the position x, $c(x + \Delta x)$ is calculated by:

$$c(x + \Delta x) = c_{mix}(x) + \frac{F(c_{mix}(x))P(x)\Delta x}{qx}, \tag{3.80}$$

where $\quad c_{mix}(x) = \dfrac{qxc(x) + q\Delta x\, c_{in}}{(x + \Delta x)q}.$

There is no breakthrough in this case, since the flow rate is constant in time. Termination of the calculation is thus "user-defined". Figure 3.41

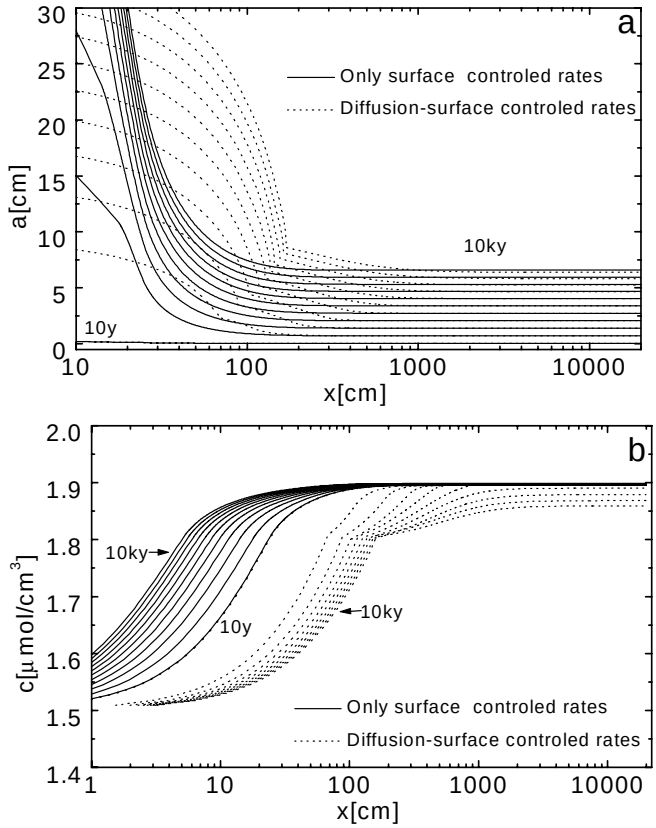

Figure 3.41: Profiles of aperture widths (**a**) and concentration (**b**) for the fracture with constant recharge. $a_0 = 0.03cm$, $b_0 = 100cm$, $Q_0 = 0.1cm^3/s$, $q = 1.5 \cdot 10^{-4}cm^2/s$, $c_0 = c_{in} = 1.5\mu mol/cm^3$. Profiles are taken in ky intervals. Dotted lines show the case where surface-transport controlled dissolution is considered, full lines show the results when only surface control is considered. Note the logarithmic scale in x.

shows the evolution of the aperture widths and concentrations along the fracture for various time. Full lines represent the case where only surface controlled rates were assumed, dotted lines present the case where diffusion limited dissolution was also considered. The difference between both cases is significant only close to the entrance, where the rates are diffusion

controlled. Although including diffusion makes no difficulty in numerical models, excluding it can be a big help on the way towards more general - analytical results.

From the model runs we observe the following:

- Provided that the fracture is wide i.e. $b \gg a$, it is widened uniformly in time and the widening does not depend on its initial aperture.
- The concentration initialy exhibits a fast rise to above 99% of its asymptotic value c_{sat}. We define x_{sat} as the point in the fracture where $c = 0.99c_{sat}$.
- The fracture widths initially drop and than stay constant for $x \geq x_{sat}$.
- c_{sat} and x_{sat} do not depend on the initial length and width of the fracture.
- There is no feedback mechanism since the hydraulic head is not constant, but is assumed to be adapted to the offered recharge.

The evolution of the fracture with constant recharge is thus well described by c_{sat} and x_{sat}. How these depend on the specific parameters q and c_{in} is shown on Fig.3.42. It shows the dependence of x_{sat} and c_{sat} on q for various c_{in} as denoted on the lines in $\mu mol/cm^3$. Since c_{sat} is the asymptotic value for $x \to \infty$, x_{sat} is taken at the point where $x = 0.99 \cdot c_{sat}$. Full lines present the case when only linear kinetics ($c_s = c_{eq}$) was assumed, dashed lines present the results when also nonlinear dissolution rates ($c_s = 0.9c_{eq}$, $n = 4$) are considered.

3.6.3 ANALYTICAL APPROXIMATIONS

To gain some more insight into the dependence of c_{sat} and x_{sat} presented in Fig.3.42, we try to get some analytical approximations. Multiplying the terms in Eq.3.79 and neglecting the higher order differentials ($dxdc$) we get

$$\frac{dx}{Q_0 + qx} = \frac{dc}{q(c_{in} - c) + F(c)P}. \tag{3.81}$$

For a wide fracture, where P can be regarded as a constant, the equation does not depend on the fracture aperture and is therefore constant in time. The differential equation can be easily integrated for the case of linear kinetics, where $F(c) = \tilde{k}_1(c_{eq} - c)$ eith $\tilde{k}_1 = k_1/c_{eq}$. In this case we obtain basic integrals for x and c. The result yields:

$$\left[1 + \frac{qx}{Q_0}\right]^{-(1+\tilde{k}_1 P/q)} = \frac{qc_{in} + \tilde{k}_1 P c_{eq} - c(\tilde{k}_1 P + q)}{qc_{in} + \tilde{k}_1 P c_{eq} - c_{in}(\tilde{k}_1 P + q)}. \tag{3.82}$$

Note that c_0 was taken equal to c_{in}. Some further algebraic "gymnastics" gives an explicit equation for $c(x)$:

$$c(x) = \frac{qc_{in} + \tilde{k}_1 P c_{eq}}{q + \tilde{k}_1 P}\left[1 - (1 + qx/Q_0)^{-(1+\tilde{k}_1 P/q)}\right] + c_{in}\,(1 + qx/Q_0)^{-(1+\tilde{k}_1 P/q)}. \tag{3.83}$$

If $x \to \infty$ the term $(1 + qx/Q_0)^{-(1+\tilde{k}_1 P/q)}$ vanish and an expression for c_{sat} is obtained:

$$c_{sat} = \frac{qc_{in} + \tilde{k}_1 P c_{eq}}{q + \tilde{k}_1 P}. \tag{3.84}$$

From Eq.3.83 we see that $c(x) = c_{sat}$ when $Q_0 = 0$.

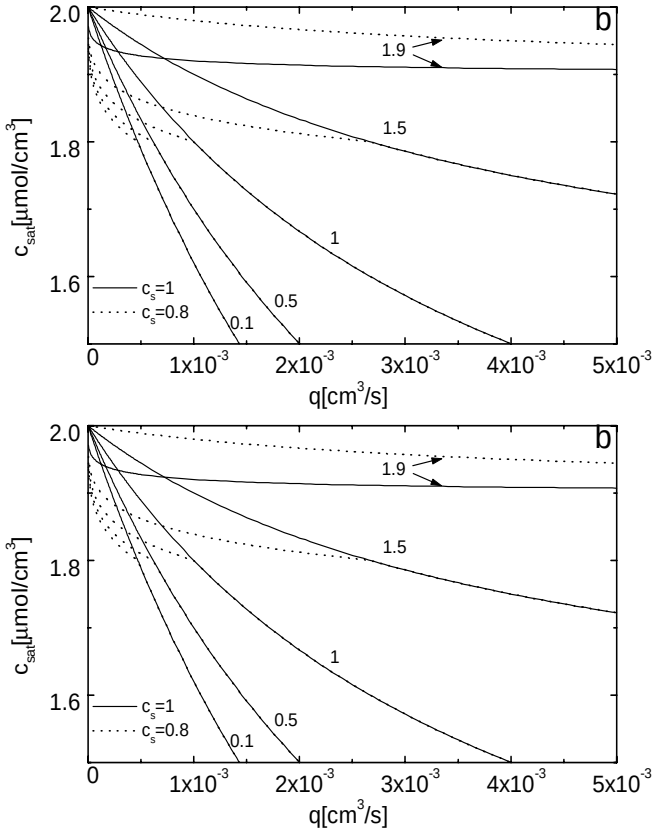

Figure 3.42: The dependence of x_{sat} (**a**) and c_{sat} (**b**) on q for various c_{in} (denoted on the lines in $[\mu mol/cm^3]$). In both cases $Q_0 = 10^{-3} cm^3/s$. Other parameters are the same as in Fig.3.41

The value of x_{sat} can then be determined according to some criterion which we choose, e.g. at $c_{crit} = 0.99 c_{sat}$. From Eq.3.82 we obtain:

$$x_{sat} = \frac{Q_0}{q}\left[\left(\frac{1 - c_{in}/c_{end}}{1 - c_{crit}/c_{sat}}\right)^{\frac{q}{q+\tilde{k}_1 P}} - 1\right]. \tag{3.85}$$

Note that $x_{sat} \propto Q_0$.

Fig. 3.42 presents the dependence of x_{sat} and c_{sat} on q. Full lines show the case when only linear kinetics is assumed and represent directly

the results from Eqs.3.84 and 3.85. Dashed lines show the dependence when kinetic switches at $c_s = 0.9c_{eq}$ to non-linear with $n = 4$, $k_4 = 4 \cdot 10^{-8} mol/cm^2 s$.

Whenever $c_{in} < c_s$ the results with and without the switch of the kinetic order coincide as soon as q is large enough to keep the resulting concentration c_{sat} below c_s. Note, that q is not arbitrary but is limited by the amount of precipitation which can occur in nature. Assuming direct recharge of rain into the fracture, value $q = 1 \cdot 10^{-3} cm^2/s$ would correspond to a precipitation rate about $300 mm/y$. Thus cases with $q > 2 \cdot 10^{-3}$ are unlikely in nature and are here presented for completeness.

3.6.4 FRACTURE WITH A CONSTANT RECHARGE AND VARYING GEOCHEMICAL PARAMETERS

In the case of the fracture with constant head conditions we discussed how variations of geochemical parameters, such as kinetic konstants or CO_2 content influence the early evolution. Here we present a few results for the case when kinetic parameters n and k_n change within the fracture (see Sec.3.3) under conditions of constant recharge.

As in the constant head conditions, the rates and consequently the widths change at the lithology boundary if the concentration c_{sat} is above the c_s. If $c_{sat} < c_s$ the lithology change makes no difference, since the first order kinetic is active. If $c^{(1)}_{sat} > c_s$ than the ratio between the rates on the both sides of boundaries is equal to

$$\frac{F(KL)_{n_1}}{F(KL)_{n_2}} = \frac{k_{n_1}}{k_{n_2}} \left(1 - \frac{c_{sat}}{c_{eq}}\right)^{\frac{n_1 - n_2}{1 - n_1}} \tag{3.86}$$

Fig.3.43a shows the profiles of aperture widths when the nput concentration $c_{in} = 1.8 \mu mol/cm^3$, other parameters are as in Fig. 3.41. Dissolution rates and aperture widths at the boundary drop, but then they increase behind the boundary and approach the asymptotic value. The reason for this increase is that $c^{(1)}_{sat} > c^{(2)}_{sat}$, therefore the concentration of solution for $x > x^{(2)}_{sat}$ is lower than the concentration at the boundary.

In Fig.3.43b the kinetic parameters change from $n = 8$ to $n = 4$. Other parameters are the same as in figure a. The aperture widths at the boundary are boosted up. Then they drop to asymptotic value, since the concentration beyond the lithology boundary increases and therefore the dissolution rates and aperture widths decrease.

In both cases the fracture can be considered as two succesive fractures with the initial flow and concentration $Q^{(1)}_0$ and $c^{(1)}_0$ for $x < KL$ and $Q^{(2)}_0 = Q^{(1)}_0 + qKL$, $c^{(2)}_0 = c^{(1)}_{sat}$ for $X > KL$, provided that $KL > x^{(1)}_{sat}$.

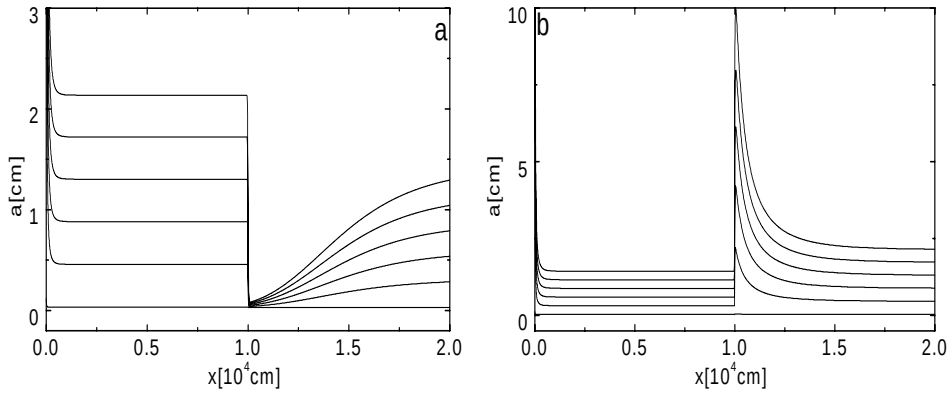

Figure 3.43: Evolution of aperture widths for the fracture with a constant recharge and lithology boundary. **a)** $n_1 = 4$, $n_2 = 8$, $K = 0.5$. **b)** $n_1 = 8$, $n_2 = 4$, $K = 0.5$. First profile is taken at 10y, than every 2ky starting at 2ky. $Q_0 = 0.1cm^3/s$, $q = 1.5 \cdot 10^{-3} cm^2/s$. Other parameters are tha same as in Fig.3.41.

3.6.5 CONCLUSION

The main result obtained in this section is the concept of a steady state: Concentration along the fracture remains constant after some distance x_{sat} from the entrance. Almost entire fracture opens evenly and widens linearly in time.

Fractures with constant recharge as discussed here are rather unlikely in nature. Nevertheless, the concept of a fracture with the constant recharge will be met in Chap.5 where we shall discuss the evolution in an unconfined aquifer.

4 THE EVOLUTION OF TWO-DIMENSIONAL NETWORKS UNDER CONSTANT HEAD CONDITIONS

One-dimensional models are the key for understanding the processes acting during early karst evolution. To predict how the spatial evolution and the distribution of evolving conduits of early 3-dimensional karst depends on the mechanical and geochemical parameters, we have to employ models with higher dimensions. A first step forward are two-dimensional (2D) fracture networks. The evolution of early karst in 2D networks under the constant head conditions was discussed by Lauritzen et al.(1992), Groves and Howard (1994a) (1994b) (1995), Dreybrodt and Siemers (2000), Siemers and Dreybrodt (1998) and Siemers (1998). The reader is referred to the work of Siemers and Dreybrodt (1998) and Siemers (1998), where the modelling concepts used also in this work are explained in detail. In this chapter we make a quick summary of the results presented in the works quoted above and add some new results by including new geochemical parameters such as CO_2 sources and mixing corrosion.

4.1 BASIC PRINCIPLES OF MODELLING 2D FRACTURE NETWORKS

To model early karstification of 2D fracture networks one needs:

1. Generating the fracture network with imposed boundary conditions.
2. Applying the dissolution-tranport model as presented in Chap.3.1 to the fractures of the net. This includes calculation of the head difference and dissolutional widening for each fracture.

4.1.1 GENERATION OF 2D NETWORKS

There are several ways of generating the 2D fracture networks. The simplest option is the regular rectangular ("brick") network first presented by Groves and Howard (1994a). This chapter upgrades the work of Siemers and Dreybrodt (1998) who used percolation networks to approximate the stochastic distribution of primary fractures in limestone.

THE GENERATION OF PERCOLATION NETWORKS

Fig.4.1a shows a bond percolation network on a square lattice. This is generated the following way. Initially a square lattice of netpoints (sites) is generated. The lines connecting the neigbouring netpoints are occupied by fractures (open bonds) with probability p. Fig. 4.1b shows an excerpt of the net shaded in figure a. The dots represent the netpoints. The full lines represent the fractures (open bonds) and the dotted represent the closed bonds.

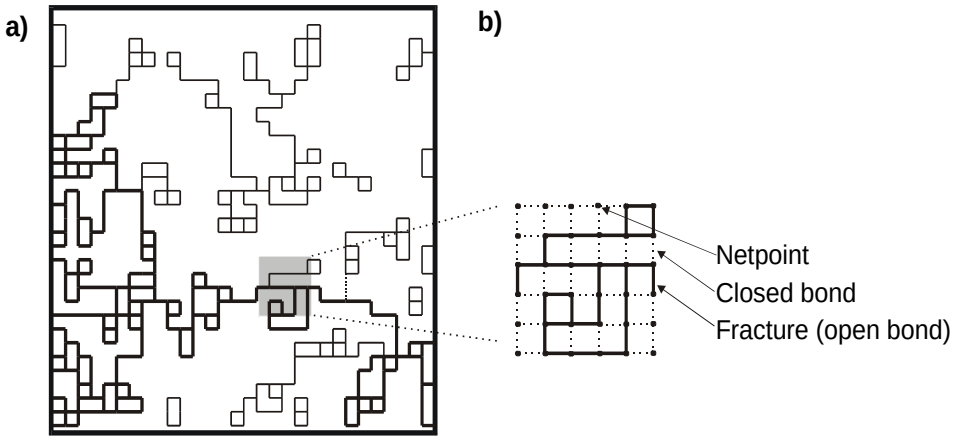

Figure 4.1: An example of percolation net with $p = 0.5$. **a)** Thick lines denote the percolation backbone. Non-percolating clusters or dead ends of percolation backbone are presented by the thin lines. **b)** Excerpt from the net, with netpoints and occupied and non-occupied bonds marked by the full and dotted lines. See text.

Fractures generated this way form clusters of various sizes, depending on p (Fig.4.1a). For each lattice type (e.g. triangular, square, honeycomb; see Stauffer (1960) or Lee and Farmer (1993) for details) there is a critical occupation probability p_c where infinite clusters start to form. For the square lattice presented here we use bond percolation [1] with $p_c = 0.5$.

[1] Net can also be generated via site percolation procedure, where the occupation of the netpoints is determined statistically. Fracture is present if both netpoints on its sides are occupied.

Therefore, taking a square net with $p \geq 0.5$ a cluster of fractures exists connecting the sides of the net which can transmit water.

All generated fractures can be classified into two classes:

1. **Percolating fractures** are connected to the entrance and to the exit of the network by uninterrupted and self-avoiding pathways. They are grouped into the cluster which is connected to the left and right boundary of the network and thus they can carry flow. They are represented by the thick lines in Fig.4.1a.
2. **Non-percolating fractures** do not carry flow within the network. They are either parts of isolated clusters or dead ends. These are presented by the thin lines in Fig.4.1b. Simple dead ends, i.e. fractures with no connection or only one to neighbouring fractures are already excluded from the figure.

During a process of network generation all the non-percolating fractures are omitted by an iterative procedure.

THE BOUNDARY CONDITIONS

Fig. 4.2a shows a percolation net with $p = 0.8$ and the boundary conditions imposed on it. These are set as follows:

- Hydraulic head h_{in} at the left-hand side and $h_{out} = 0$ at the right-hand side of the net.
- Nonpermeable upper and lower boundary.
- Solution is entering the system with initial Ca^{2+} concentration c_0 and is in equilibrium with partial CO_2 pressure $p^0_{CO_2}$.

The initial aperture widths of the fractures can have any distribution. In the presented runs all fractures have equal initial aperture widths a_0 and equal initial widths b_0.

CALCULATION OF NETWORK EVOLUTION

To calculate the widening of each fracture in the network, the flow rate and the concentration of solution entering it must be known as discussed in Sec.3.1. Flow through the fracture connecting the node points i and j is given by

$$Q_{ij} = \frac{h_i - h_j}{R_{ij}}, \tag{4.1}$$

where R_{ij} is the resistance of the fracture, h_i and h_j are the heads at nodes i and j. The calculation of the heads is based on mass conservation for

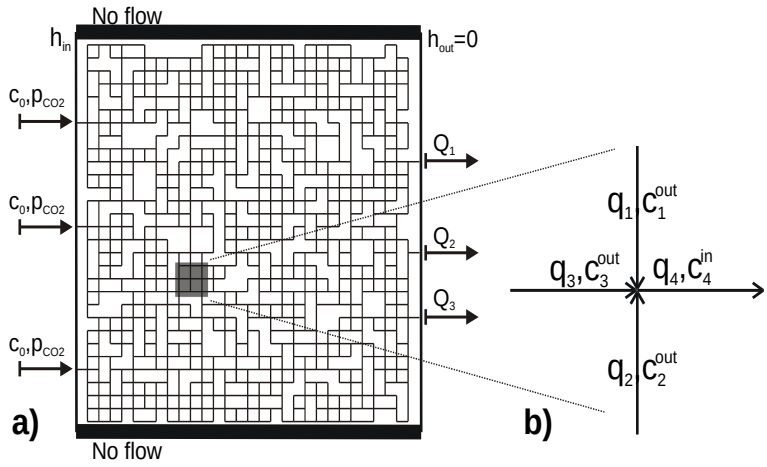

Figure 4.2: **a)** Percolation net ($p = 0.8$) with imposed boundary conditions. Inputs are on the left-hand side and outputs on the right-hand side of the net. The upper and the lower boundaries are impermeable. **b)** Junction of four fractures. Mass conservation for flow and ionic species is valid at all junctions. See text for discussion.

each node point (see Fig.4.1b)

$$\sum Q_{in}(i) - \sum Q_{out}(i) = \sum_j Q_{ij} = 0, \tag{4.2}$$

where$Q_{in}(i)$ is the flow rate towards node i and $Q_{out}(i)$ the flow rate away from it. Q_{ij} is the flow rate through the fracture connecting nodes i and j and R_{ij} its resistance. Eqs.4.1 and 4.2 give a set of linear equations for the unknown heads. This can be solved by standard methods. A good choice is a preconditioned CG iteration method for sparse matrices (see (Stewart and Leyk, 1994)).
Once the flow rates are known, the dissolution widening is calculated by the following procedure:

1. Apply the one-dimensional dissolution-transport to all the fractures connected to the input points at the left boundary. Calculate the new profile of these fractures for the time Δt.
2. Select the nodes where the concentration of the inflowing solution is known and apply the transport-dissolution model to the fractures draining the water from them. See App.A for some technical details on this point.
3. Calculate the new profiles for these fractures and the concentrations at their exits. In all presented model runs complete mixing [2] at the nodes

[2]See (Philip, 1988), (Hull and Koslow, 1986) for more details on mixing at the fracture intersection. Our measurements on a physical model of a fracture intersection show that combination of complete mixing and stream routing would be the best choice. Further knowledge on this topic is required. Siemers and Dreybrodt (1998) and Siemers (1998) demonstrated the dependence of the network evolution on the mixing model applied

is assumed. The concentration of the solution at node i is than given by (see also Fig.4.1)

$$c_i = \frac{\sum_j Q_j c_j^{out}}{\sum_j Q_j}. \tag{4.3}$$

Q_j is the flow rate of a fracture carrying the water to the node i and c_j^{out} its concentration at the exit.

4. Repeat 2 and 3 until the new profiles for all conduits have been obtained.
5. Calculate the new head distribution according to the new fracture resistances and repeat 1-4 for the next timesteps until the onset of turbulent flow. Laminarity of the flow is assured through calculation of the Reynolds number for each fracture at each timestep.

4.1.2 RESULTS FOR THE BASIC CASE

The set of figures in the next few pages shows the various aspects of the evolution of the percolation network. Fig.4.3 shows the aperture widths in units of the initial aperture width a_0. Fig.4.4 shows the flow rates in units of the maximum flow rate Q_{max} in the net . Note that that Q_{max} increases in time. Therefore the same line thicknesses represent different absolute values at different time steps. Fig.4.5 shows the distribution of the dissolution rates in units of $F(c_s) = 4 \cdot 10^{-12} mol/cm^2 s$. Fig.4.6 shows the contour map of the head distribution. The figures present four snapshots of the net at different timesteps: at 1ky, at 3ky, at 5.5ky and at breakthrough at 5.81ky. The parameters of the net are given in the caption of Fig.4.3. The percolation probability is 0.8. The net has three inputs and three outputs marked by A, B and C and A^*, B^* and C^*. The solution has the same chemical properties at all inputs.

- **Situation at 1ky** is presented by figures a in Figs.4.3-4.6. [3] The fractures close to the inputs A,B and C are in the region of high dissolution rates and have therefore been widened considerably. The distribution of flow rates is relatively uniform, except in the vicinity of inputs and outputs. Dissolution rates drop continuously from the left to the right side. Opening of the fractures close to the inputs has caused the penetration of high hydraulic head ($h > 0.999 h_{in}$) into the net. The vertical distribution of hydraulic heads and dissolution rates is uniform, except close to the inputs and outputs.
- **At the midpoint at 3ky** shown by figures b in Figs.4.3-4.6, the pathways marked by 1, 2 and 3 on Fig.4.3b have progressed deeper into the network. In this region the flow and high dissolution rates are already focused to the fractures comprising these pathways. More to the right,

[3] Discussion of the presented results will be time oriented. Therefore the reader should consider the figures of all parameters at certain time, e.g. Figs.4.3-4.6 a for the state at 1ky.

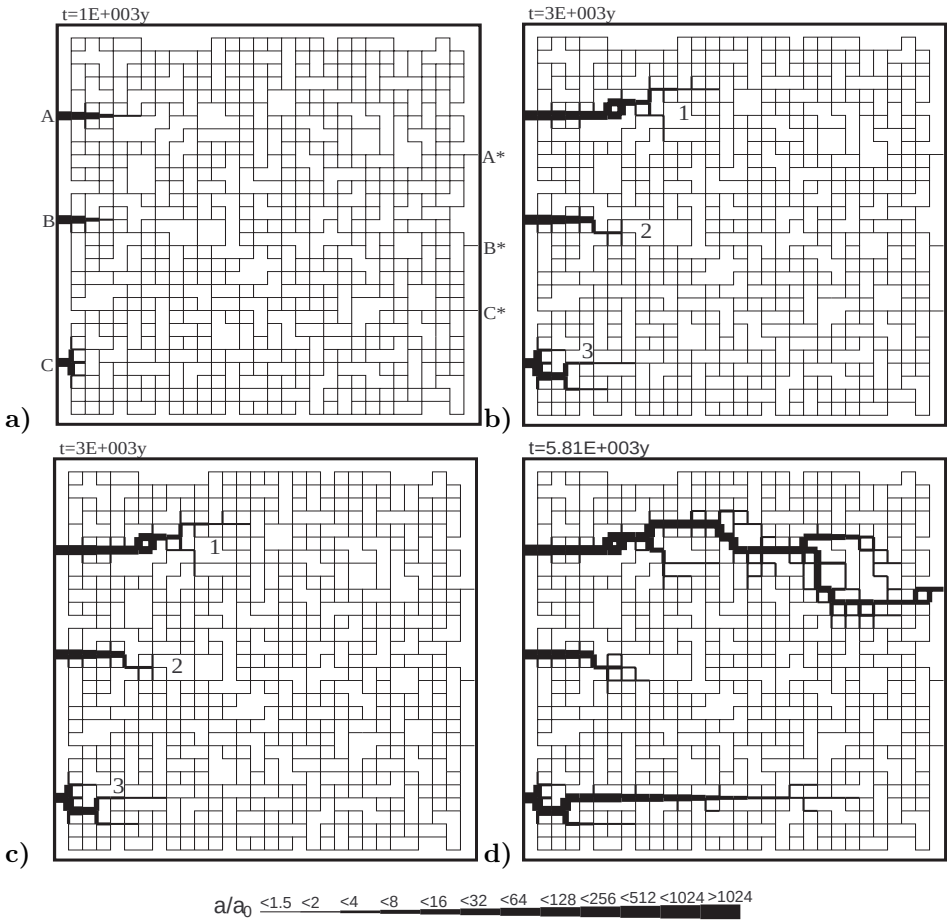

Figure 4.3: Aperture widths of the fractures in a percolation network in units of a_0 at different stages of its evolution . Times are denoted at the figures. The size of the net is $900m \times 900m$, grid size is $30m$, $p = 0.8$. Other parameters: $a_0 = 0.03cm$, $b_0 = 100cm$,$\Delta h = 50\,m$, $c_0 = 0$, $c_{eq} = 2\,\mu mol/cm^3$, $k_1 = 4 \cdot 10^{-11}\,mol/cm^2s$,$n = 4$,$k_4 = 4 \cdot 10^{-8}\,mol/cm^2s$. Inputs and outputs are denoted on figure a by A,B,C and A*, B*, C*, respectively.

in the part where no considerable widening has occured, the distribution of flow rates is still uniform. In this part the dissolution rates have also increased. The regions of high hydraulic heads (lighter areas in Fig.4.6) have penetrated deeper, causing high gradients in the right hand side of the net.

- **Close to the breakthrough at 5.5ky** (figure c in Figs.4.3-4.6) pathway 1 starting at input A almost reaches the output A*. Dissolution rates and flow rates are high along this pathway. The pathway 3 connecting C and C* is a bit less favourable, but has still evolved considerably. The looser of the "breakthrough race" is pathway 2 connecting B and

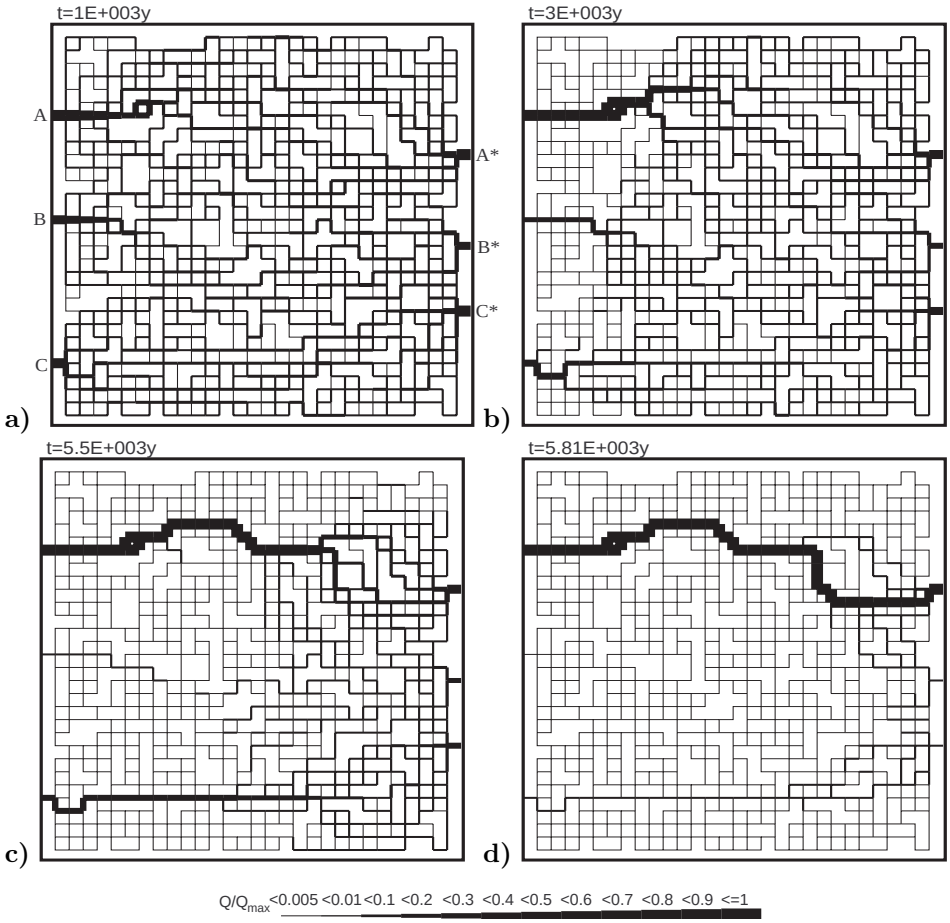

Figure 4.4: Evolution of flow rates. Line thicknesses represent the magnitude of flow rates in units Q/Q_{max}, where Q_{max} is the flow through the fracture with the highest flow rates. **a)** $Q_{max} = 5.36\,cm^3/s$, **b)** $Q_{max} = 10.12\,cm^3/s$, **c)** $Q_{max} = 30\,cm^3/s$, **a)** $Q_{max} = 172\,cm^3/s$.

B*. The region of high hydraulic heads caused by an efficient widening of pathways 1 and 3 reaches almost to the outputs preventing the flow along the less developed pathway 2 (BB*).

- **The breakthrough situation at 5.81ky** is shown by figure d in Figs.4.3-4.6. At 5.81ky breakthrough occurs along pathway 1, which carries most of the flow. Pathway 3 has also evolved close to the breakthrough, while pathway 2 has not evolved any further. High dissolution rates act along both evolved pathways. Note that some flow with high dissolution rates also leads from pathway 1 and 3 to the output B*. Consequently close to the output A* a set of vertical fractures is evolving in the direction of output B*. The breakthrough of pathway 1 ends our simulation with the onset of the turbulence.

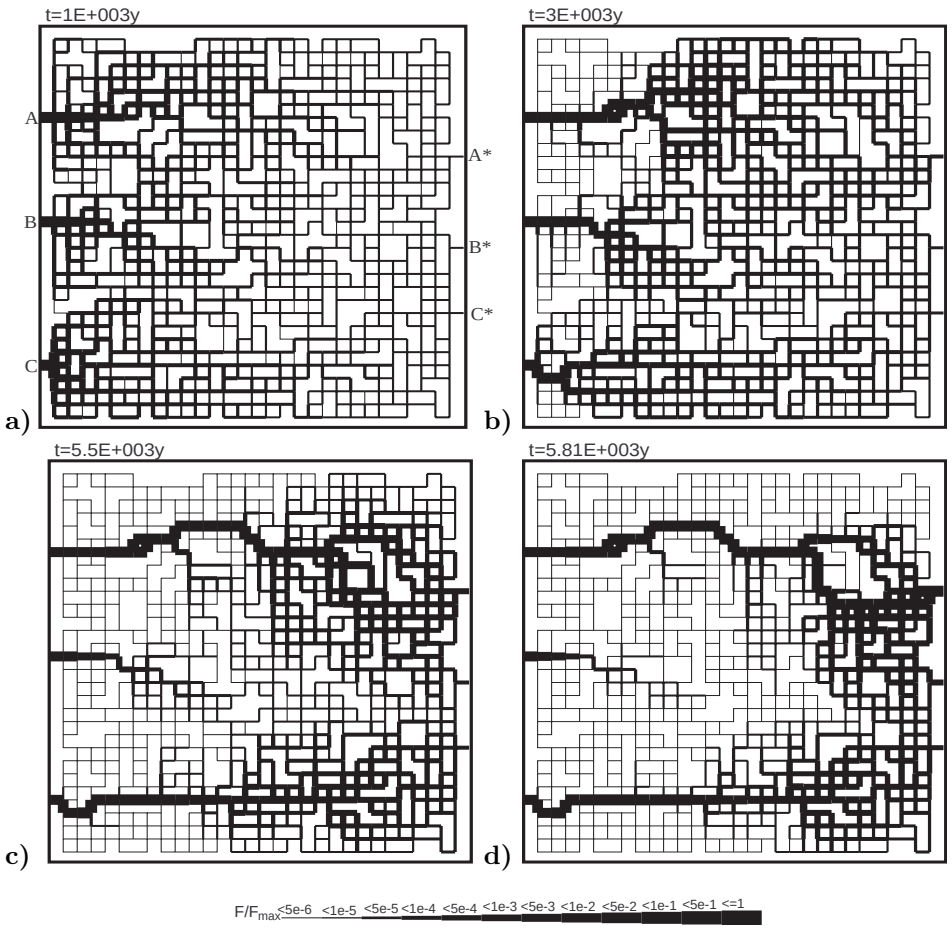

Figure 4.5: Evolution of dissolution rates. The line thickness represent the dissolution rates in units F/F_{max}, where $F_{max} = F(c_s) = 4 \cdot 10^{-12}\, mol/cm^2 s$.

Probably the most important result of 2D models is that the time evolution of flow is in a good accordance with the one dimensional models. Fig.4.7 shows the flow through each input and output as it evolves in time. The flow through inputs A and C increases continuously due to the feed-back mechanism as in the 1D model. Flow through input B initially increases, but starts to decrease after 2ky due to the hydraulic head redistribution caused by efficient widening of the pathways 1 (AA*) and 3 (CC*) (see discussion on the Figs.4.3-4.6). Note that the output B* attracts also the water from the inputs A and B, therefore the flow rate there also increases and shows breakthrough behaviour.

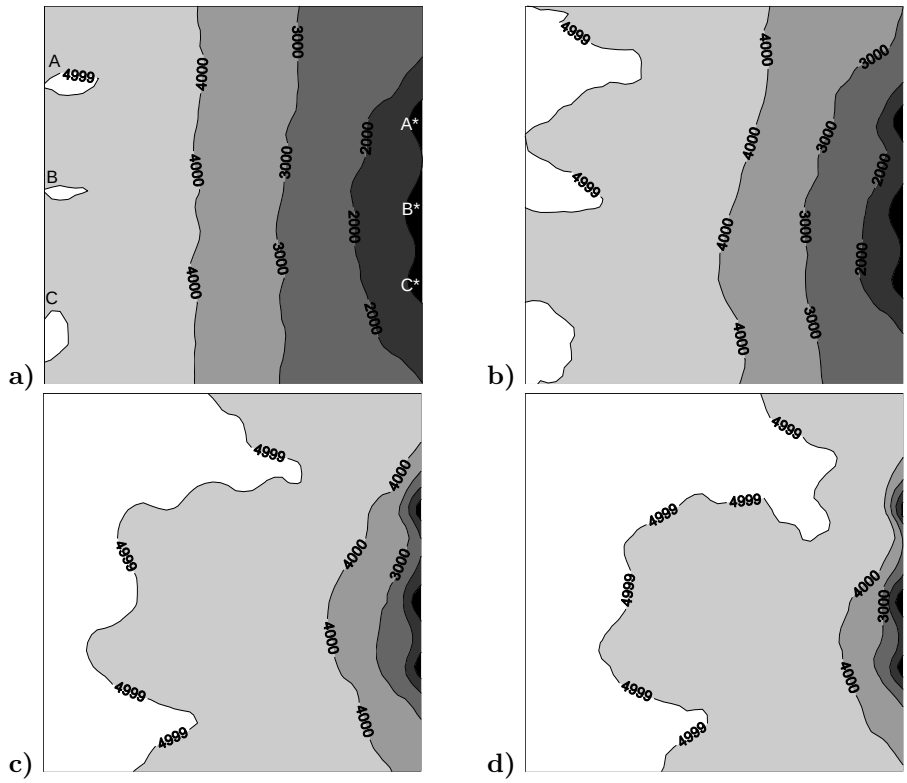

Figure 4.6: Distribution of the hydraulic heads. Contour map. Value on the isolines are given in centimeters. On figure a the positions of inputs and outputs are marked.

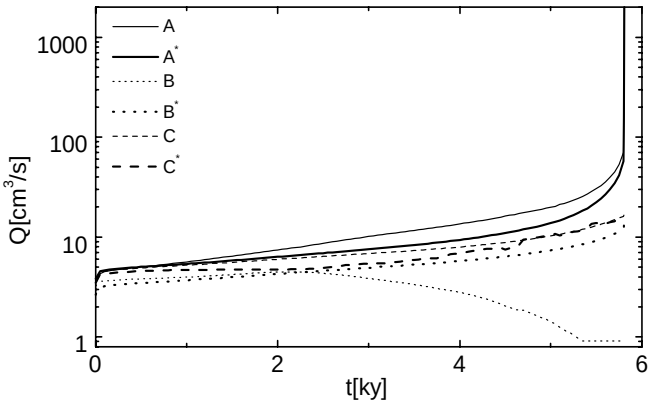

Figure 4.7: Evolution of flow rate at the inputs and outputs of the percolation net presented in Figs.4.7. The inputs A,B,C and outputs A*,B*,C* are depiceted at figures a on Figs.4.3-4.6.

SOME GENERAL CONCLUSIONS

Of course we cannot give general conclusions based on the one single case shown here. Therefore the reader is referred to the work of Siemers and Dreybrodt (1998) for details. There it is shown that the breakthrough times of 2D networks are in a good agreement with Eq.3.34, when the length L is the length of the winning pathway. When the initial distribution of pathways is such that there is significant difference in their length or head, the pathway which exhibits a minimal breakthrough time is also the winning one. When the resistances of the pathways are close to each other, one must also consider the distribution of dissolution rates which is determined by the chemical parameters and mixing rules used in the model. The length of the pathways and therefore also T_B decreases with increasing percolation probability p.

4.2 EVOLUTION OF 2D NETWORK IN VARIOUS GEOCHEMICAL SETTINGS

We discussed several geochemical mechanisms which considerably affect the evolution of a single fracture (See Secs.3.1, 3.3, 3.4 and 3.5). These effects were discussed from the viewpoint of breakthrough time. In this section we introduce similar scenarios into the percolation networks, and we will pay more attention to the evolution of conduit patterns.

The effect of varying lithology on the evolution of 2D percolation network was discussed by Siemers (1998).

4.2.1 THE INFLUENCE OF INPUT SATURATION RATIO ON THE EVOLUTION OF FRACTURE NETWORKS

As shown for the single fracture (See Sec.3.1) the feedback mechanism is switched off for high input saturation. The next step is to examine the effect of the initial saturation state on the breakthrough time and the pattern evolution in fracture networks.

Fig.4.8 shows the aperture widths at the onset of turbulence for the net presented in Figs.4.3-4.6 but with initial concentration close to equilibrium; at all inputs $c_0/c_{eq} = 0.95$ in Fig.4.8a, and $c_0/c_{eq} = 0.98$ in Fig.4.8b.

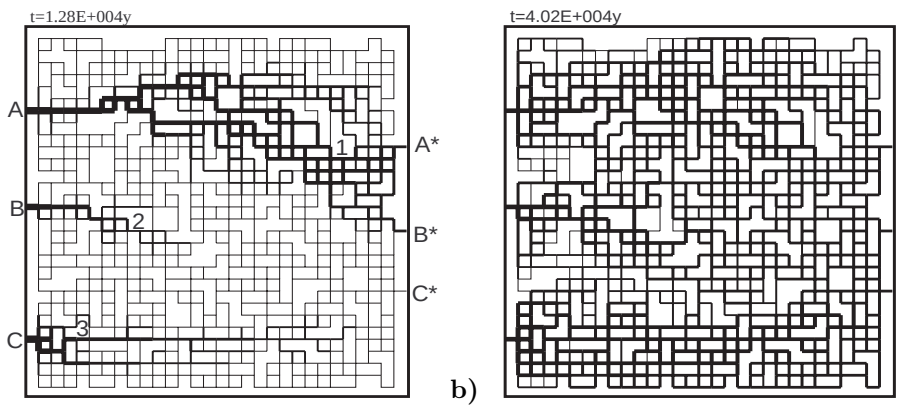

Figure 4.8: Aperture widths at the onset of turbulence for the net presented in Fig.4.3 with **a)** $c_0/c_{eq} = 0.95$ and **b)** $c_0/c_{eq} = 0.98$

Comparing Figs.4.8a, b and Fig.4.3d we observe, that the evolved pattern is more maze-like if c_0/c_{eq} is closer to 1. In Fig.4.3d two relatively unbranched pathways evolved. The set of pathways marked by 1 on the

Fig.4.8a is already more branched and extends also to the output B*. The situation on Fig.4.8b is quite different. One still observes preferential pathways, but they are hidden within the complex network of evolved conduits.

This observed behaviour can be generally explained by the following reasoning: Consider two arbitrary pathways within the evolving net. Pathway A with length L_A and flow rate Q_A and pathway B with L_B and Q_B. Assume that they both drain water from the same node point. Therefore they have the same initial saturation ratio c_{in}/c_{eq}. As shown in Sec.3.1 dissolution rates at the exit of these pathways can be taken as a measure telling how differently the pathways evolve. From Eq.3.19 we find the ratio $F_1(L_1)/F_2(L_2)$ as

$$\frac{F_A(L_A)}{F_B(L_B)} = \left(\frac{1+\alpha(1-c_{in}/c_{eq})^{n-1}L_A^2}{1+\alpha(1-c_{in}/c_{eq})^{n-1}L_B^2}\right)^{\frac{-n}{n-1}} . \tag{4.4}$$

Parameter α contains all the parameters which are equal for both pathways. Eq.4.4 shows that the ratio $F_A(L_A)/F_B(L_B)$ drops with rising c_{in}/c_{eq}. Therefore the pathways are more equivalent at higher c_{in}/c_{eq}. If $c_{in} \to c_{eq}$ the ratio goes to 1. Consequently the network consisting of many possible pathways shows more maze-like pattern if c_{in}/c_{eq} is close to 1.

To conclude the discussion on the influence of c_0/c_{eq}, Fig.4.9 presents the evolution of flow rates at the inputs and outputs for the both cases given in Fig.4.8. For $c_o/c_{eq} = 0.95$ the behaviour is similar to that in

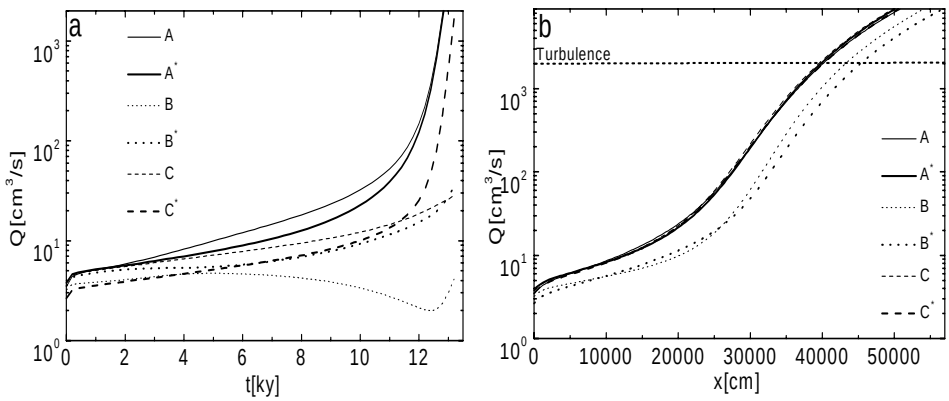

Figure 4.9: **a)** The evolution of flow rates at inputs and outputs for $c_0/c_{eq} = 0.95$. **b)** The evolution of flow rates at inputs and outputs for $c_0/c_{eq} = 0.98$. Symbols represent the inputs and outputs as marked in Fig.4.8a

Fig.4.7, except for the longer T_B. Also note the revival of flow at the input B close to the breakthrough. For $c_0/c_{eq} = 0.98$ the feedback is switching off already before turbulence occurs.

4.2.2 MIXING CORROSION AND CO_2 INPUTS IN 2D FRACTURE NETWORKS

In this section we extend the results obtained in Sec.3.4 and 3.5 by introducing different chemical compositions at the input points and introducing CO_2 inputs within the network.

THE MODEL MODIFICATION

At any point in the net the chemical composition of the solution is described by the concentration of CO_2 and Ca^{2+}, i.e. the (CO_2, Ca^{2+}) pair which belongs to some $CO_2 - Ca^{2+}$ line connecting the point $(CO_2^0, 0)$ and (CO_{2eq}, Ca^{2+}_{eq}).

When all the (CO_2, Ca^{2+}) pairs of solutions entering at various input points belong to the same line as used in the runs presented so far, each (CO_2, Ca^{2+}) point of all mixed solutions in the net also belongs to this line. Therefore only one equilibrium concentration is valid for the whole net. Fig.4.10 looks rather complex. It presents a scenario where the (CO_2, Ca^{2+})

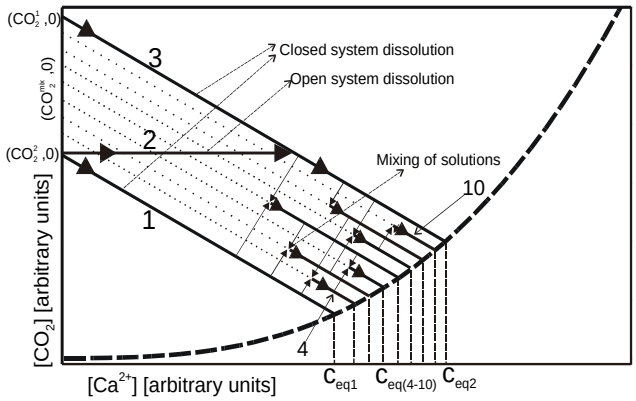

Figure 4.10: Chemical pathways of solutions with different chemical compositions. Mixing of solutions belonging to different $CO_2 - Ca^{2+}$ lines produces new solutions belonging to a new $CO_2 - Ca2+$ line.

pairs of solutions entering the net belong to different $CO_2 - Ca^{2+}$ lines. Solution 1 enters the closed system a $(CO_2^0(1), 0)$, solution 2 at $(CO_2^0(2) = CO_2^0(1), Ca^{2+}(2))$, solution 3 at $(CO_2^0(3), 0)$. Note that the pathway of solution 2 can be interpreted as solution 1 which has dissolved some amount of calcium $Ca^{2+}(2)$ in the open system conditions. It is chosen so that the pathway of solution two in the closed system coincides with that of solution 3. As these solutions mix, the (CO_2, Ca^{2+}) pairs of the mixed solutions

belong to new $CO_2 - Ca^{2+}$ lines. Thick lines 4-10 in Fig.4.10 represent the pathways of mixed solutions. The dashed lines point to the Ca^{2+}_{eq} for these curves. The number of the "higher generation" $CO_2 - Ca^{2+}$ lines depends also on the head and flow distribution in the net which defines how much the solutions with different chemical compositions mix.

Various p_{CO_2} at the inputs or CO_2 inputs in the net cause the (CO_2, Ca^{2+}) pairs of the solution in the net to belong to different lines. Therefore we have to track the CO_2 concentration in the net. When assuming complete mixing, for any node point the following relations are valid:

$$[Ca^{2+}] = \frac{\sum Q_i [Ca^{2+}]_i}{\sum Q_i} \quad \text{and} \quad [CO_2] = \frac{\sum Q_i [CO_2]_i}{\sum Q_i}. \tag{4.5}$$

To trace the equilibrium concentration in the net we track the $[CO_2]$ the same way as the calcium concentration (see App.A) and calculate c_{eq} at each node point by solving Eq.2.6.

4.2.3 MIXING CORROSION IN 2D FRACTURE NETWORKS

FIRST RESULTS: SIMPLE MIXING SCENARIO

As shown in Sec.3.5, when two solutions with points (CO_2, Ca^{2+}) on different lines mix, MC occurs. We have shown that the effect of MC depends on the distance of the points to equilibrium. and the distance between the $CO_2 - Ca^{2+}$ lines of the mixing solutions.

Fig.4.11 shows three nets at breakthrough. The only difference between the parameters of these nets is p_{CO_2} at the lower input marked by B in Fig.4.11c. In Fig.4.11a p_{CO_2} at both inputs is $0.05\,atm$ and $T_B = 16.8\,ky$. No mixing corrosion (MC) is present in this case. Two competing pathways have developed with the upper one winning.

On Figs.4.11b and c, p_{CO_2} at the input B is $0.03\,atm$ and $0.003\,atm$, with breakthrough times of $8.8\,ky$ and $5ky$ respectively.

The network in Fig.4.11 is modified so that the upper and lower region can be divided into two parts: an upper one connecting the input A to output A* and a lower one connecting the input B to the output A*. These two parts have one confluence denoted by **1** in Fig.4.11c, and a region of confluences close to the exit denoted by **2**. These are the regions where solutions from both inputs mix and consequently MC is active.

At the early stage of karstification MC is active at both locations. Widening of fractures is enhanced there such that the resistance of the developing conduit system is lowered significantly in the region between **2**, and the output A*. Therefore the upper branch developing from the input A towards the output A* has a shorter effective length by about 20%

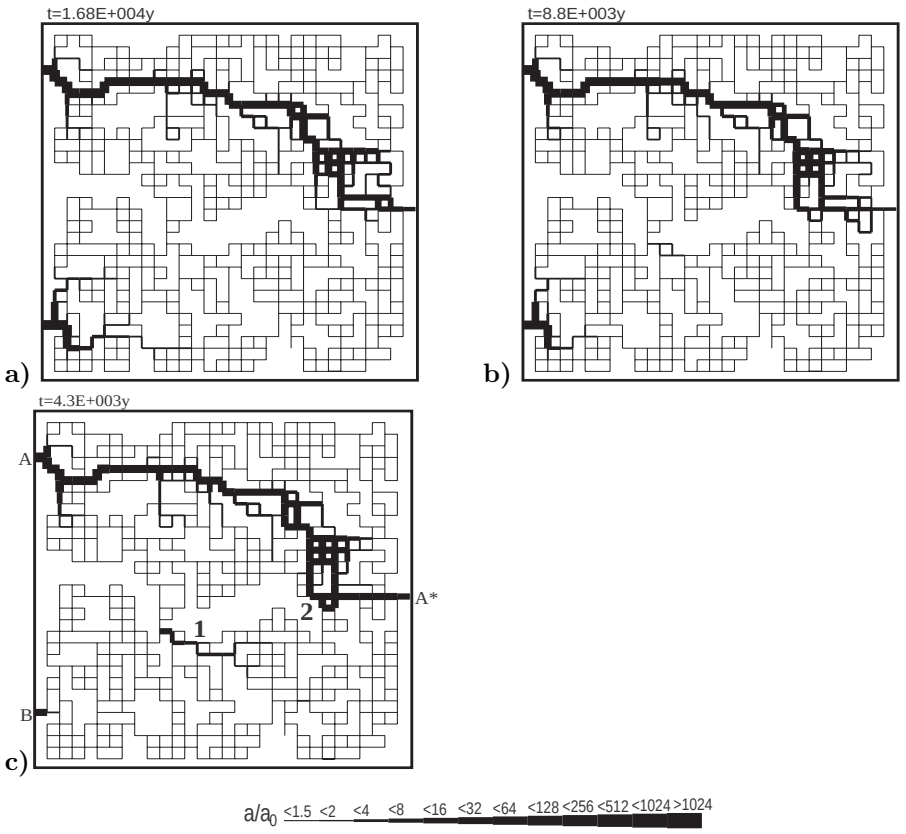

Figure 4.11: The breakthrough situation of the net with two inputs and one output. Inputs, output and mixing regions are marked on fig c. **a)** $p_{CO_2}(A) = 0.05atm$, $p_{CO_2}(B) = 0.05\,atm$. **b)** $p_{CO_2}(A) = 0.05\,atm$, $p_{CO_2}(B) = 0.03\,atm$. **c)** $p_{CO_2}(A) = 0.05\,atm$, $p_{CO_2}(B) = 0.003\,atm$. Other chemical and geometrical parameters are the same as in Fig.4.3.

from its very early evolution. Since its T_B is related to this effective length by Eq.3.34 one expects a reduction of T_B by about one half. Due to MC widening occurs at confluence **1** and a conduit starts to grow from there. This however remains isolated, since the conduits growing from the lower input cannot reach it until the breakthrough of the upper branch.

The lower branch at breakthrough is much less developed than that in Fig.4.11a for two reasons. First, it has less time to grow. Second, the equilibrium concentration of its input solution is reduced by about 25%, owing to the reduced p_{CO_2} . Therefore its T_B is expected to increase by about 50% (cf. Eq.3.34). This behaviour is more pronounced in Fig. 4.11c, where MC is more effective causing further reduction of breakthrough time and larger aperture widths of the isolated conduit system ($T_B = 5ky$). The evolution of the lower branch consequently is inhibited significantly.

FURTHER RESULTS AND DISCUSSION: THE SNAPSHOTS OF THE EVOLUTION

To gain some more insight into these processes Fig.4.12 shows the evolution of a more complex net with further connections close to the inputs. $p_{CO_2}(A)$ is 0.05 atm and $p_{CO_2}(B)$ is 0.003 atm.The colours depict the equilibrium concentrations of the mixed solutions. Red symbolizes the equilibrium concentration achieved in a closed system for $p_{CO_2} = 0.05\,atm$ ($c_{eq}(A) \approx 2.1\mu mol/cm^3$), dark blue is related to the solution with $p_{CO_2} = 0.003\,atm$ ($c_{eq}(B) = 0.17\mu mol/cm^3$). Mixing of these solutions creates new values of c_{eq} (see Fig.4.10) between the two extremes and activates MC, Δc_{eq} (See Fig.3.36 in Sec.3.5) is largest when equal flow rates are mixed, indicated by green. Light blue indicates mixing, where c_{eq} is closer to $c_{eq}(B)$, and yellow where it is closer to $c_{eq}(A)$. Both colours exhibit similar values of Δc_{eq} and therefore similar strength of MC. The line thicknesses

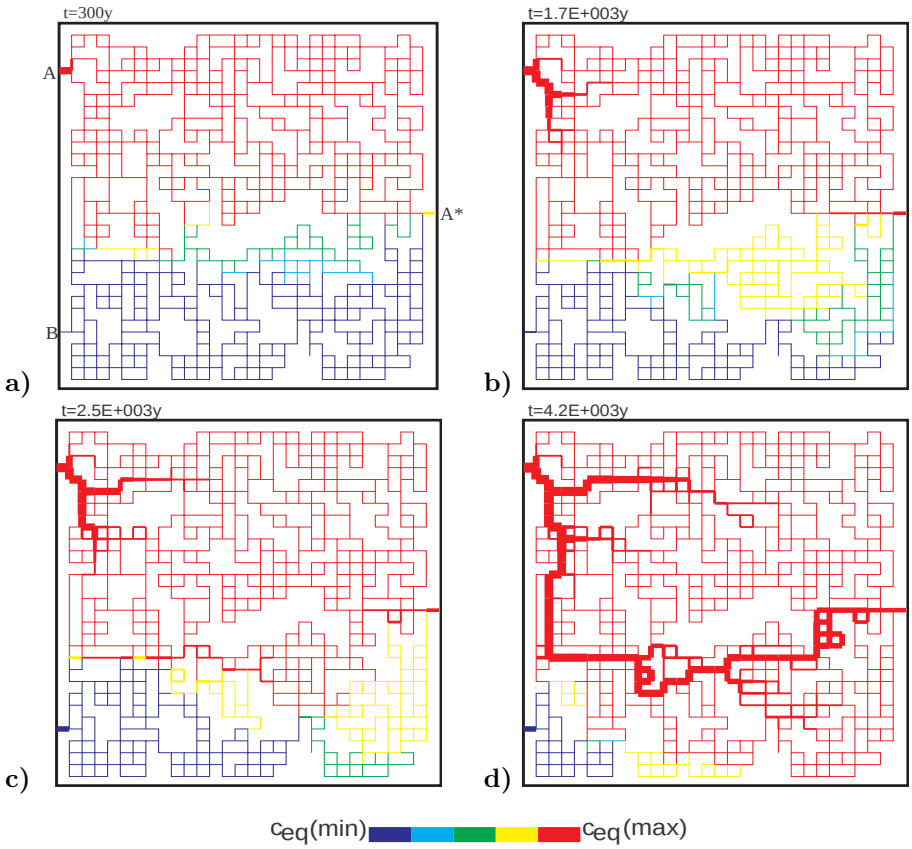

Figure 4.12: The net with $P_{CO_2}(A) = 0.05\,atm$ and $P_{CO_2}(B) = 0.003\,atm$ at four different times: **a)** $t = 0.3\,ky$, **b)** $t = 1.7\,ky$, **c)** $t = 2.5\,ky$ and **d)** $t = T_B = 4.2\,ky$. Other parameters are the same as in Fig.4.3.

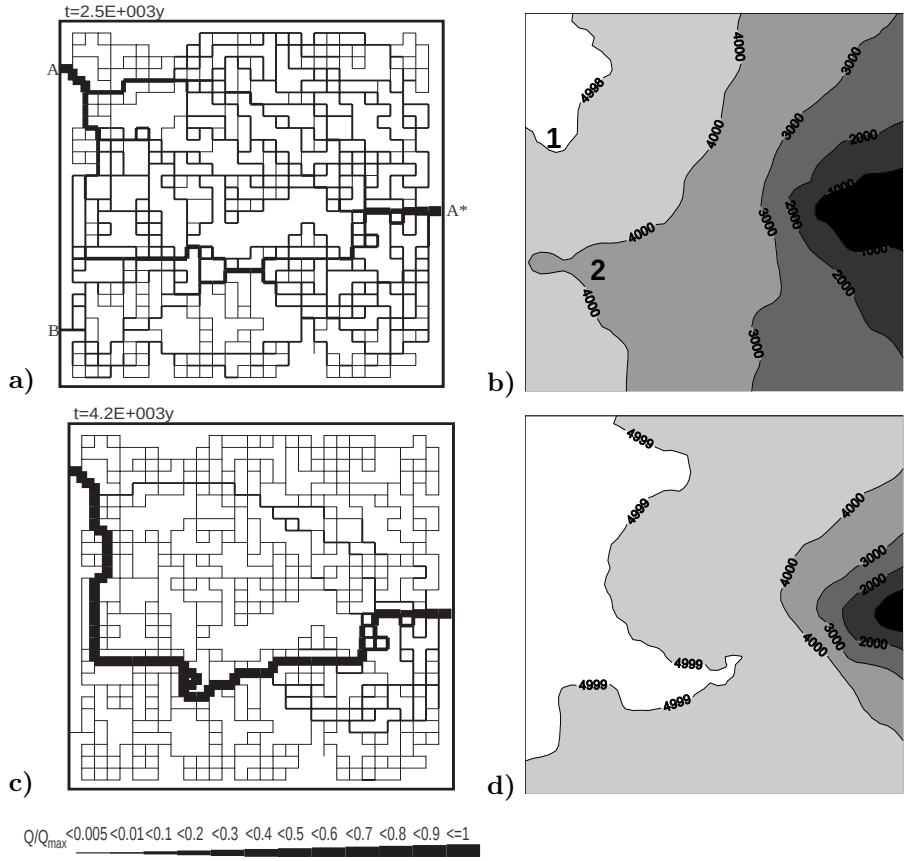

Figure 4.13: **a)** Flow rates for the net from Fig.4.12 at 2.5ky, $Q_{max} = 20cm^3/s$. **b)** Hydraulic heads at 2.5 ky. **c)** Flow rates at 4.2ky, $Q_{max} = 174cm^3/s$. **d)** Hydraulic heads at 4.2ky.

depict the aperture widths in the same scale as in Fig.4.11.

At the onset of evolution at $0.3\,ky$ (figure a) two regions of flow are established. The red one carries solution from the input A and the dark blue area from the input B. MC is active at their boundaries (green, yellow). Only little fracture enlargement has occurred so far.

After $1.7\,ky$ (figure b) enlargement of fractures becomes visible in the regions of MC. Due to the change of the hydraulic heads the flow pattern changes such that more water from the upper input invades into blue terrain of figure a. The region of strongest MC is therefore replaced by a region with c_{eq} closer to $c_{eq}(A)$ (yellow area) and furthermore a part of the dark blue terrain is replaced by green (strongest MC) and light blue. It should be noted at this point, that the flow rates (not shown here) are evenly distributed at the onset of karstification. But as time passes the ratio of the flow rates into the upper input to that into the lower one increases steadily. The colours also indicate the mixing ratio of these solutions, such

that from red to dark blue the contribution of water from the upper input decreases.

After 2.5 ky the upper conduit has penetrated towards the exit and MC has created an extended system of isolated conduits, fed mainly by water from the upper input. The area draining the lower input is further reduced. Under such conditions the shortest pathway from the upper input to the output is diverted toward the pathway along the conduits enlarged by MC and breakthrough occurs along these at 4.2ky. At this time flow from the upper input has conquered almost almost the whole net and MC region is restricted only to the vicinity of the lower input. The winning pathway is completly different to that without MC. This is identical to the one on Fig.4.11. Summarizing, we state that besides the effects of MC at the simple confluence presented in Sec.3.5, mixing corrosion in two-dimensional networks causes the redistribution of flow paths and formation of the isolated pathways. Fig.4.13 presents the flow rates and hydraulic

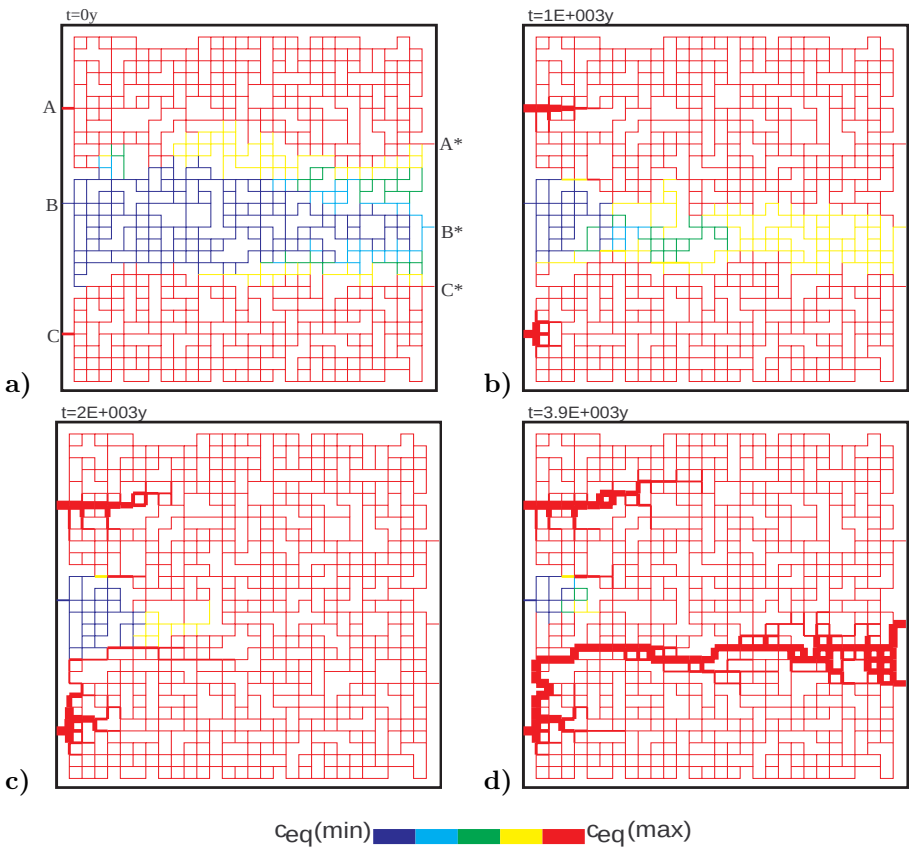

Figure 4.14: Basic net from Figs.4.3-4.6 with. p_{CO_2} at the input A and C is 0.05 atm and at the input B 0.003 atm. Aperture widths and equilibrium concentrations at different timesteps as denoted.

heads at 2.5ky and at the breakthrough. Due to the opening of the fractures caused by the MC, the region of lower ($h < 4000cm$) hydraulic heads, marked by 2 on Fig.4.13b, has evolved. The region of high hydraulic head 1 is attracted to it due to the increased gradient. Instead of forming the pathway along the shortest way to the output (AA*), the solution entering input A is diverted along the fractures connecting regions 1 and 2.

Fig.4.14 shows the evolution of the net presented in Figs.4.3-4.6. p_{CO_2} is $0.003\,atm$ at the input B and $0.05\,atm$ at the inputs A and C. Initially the regions of influence of three inputs are well separated (red,dark blue, red) with mixing zones in yellow, light blue and green at the boundaries (figure a). As the time progresses - figures b and c at 1 and $2\,ky$ - more flow from the input A and C invades into the region of input B and the mixing region is retreating towards the inputs. The effect of MC is already visible, since the isolated fractures evolved in the mixing zones are creating the shortcuts for the flow. At $2\,ky$ as presented in figure d the conduit system evolving from the input C is joining an isolated system caused by the MC. Figure d shows the resulting pattern at the breakthrough at $3.9\,ky$. As we see, it differs considerably to that of Fig.4.3 where the mixing corrosion is not present. In the settings presented the MC caused a new effective pathway leading from the lowermost input.

ANOTHER SCENARIO WITH ACTIVE MC : SAME p_{CO_2} BUT DIFFERENT Ca^{2+} CONCENTRATION AT THE INPUTS

Up to now the input solutions were calcium free, i.e. $c_0 = 0$ and different CO_2 concentrations at different inputs were the reason for the MC. As mentioned in Sec.3.5 and shown in Fig.4.10, MC occurs whenever (CO_2, Ca^{2+}) pairs of solutions entering the system belong to different $CO_2 - Ca^{2+}$ lines.

This is also the case when the dissolution history of solutions in open system differs (see line 1 and 2 in Fig.4.10). In this case solutions enter the closed system with same p_{CO_2}, but with different calcium concentrations.

Fig. 4.15 shows the evolution of such a net. The net is identical to that from Fig.4.11. Both solutions are entering the closed system with $p_{CO_2} = 0.05\,atm$. Input 1 has an initial Ca^{2+} concentration $3.3\mu mol/cm^3$. This corresponds to 90% of c_{eq} in the open system for $p_{CO_2} = 0.05\,atm$. The solution entering at the input 2 has no calcium.

The evolution of the net is similar to the one presented in Fig.4.11. Conduits evolving at the mixing points A and B are representing shortcuts for the flow, changing the evolving pattern with respect to basic case (Fig. 4.11a) and reducing the T_B. Due to the high c_0/c_{eq} at the upper input, the evolving pattern between the upper input and output shows higher complexity, i.e. is more maze-like due to the reasons discussed in Sec.4.2.1.

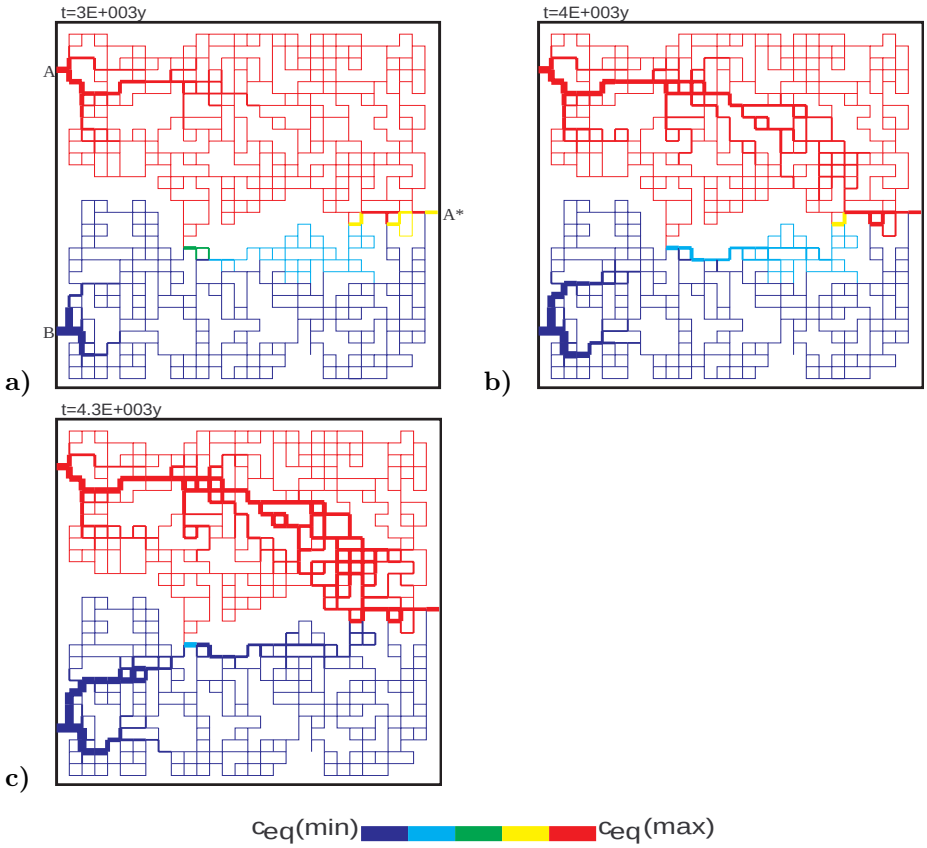

Figure 4.15: The evolution of aperture widths and equilibrium concentrations for the case where both solutions enter with the same p_{CO_2}, but different calcium concentrations. p_{CO_2} at the both inputs is $0.05\,atm$. The calcium concentration at the upper input is $3.3\mu mol/cm^3$ and set to zero at the lower input.

4.2.4 THE EFFECT OF CO_2 SOURCES IN 2D NETWORKS

THE CONCEPTS

To simulate CO_2 inputs in 2D percolation networks we define a point, line or a region located in the net with a fixed concentration of CO_2. Fig.4.16 shows the chemical pathways of solutions when CO_2 is introduced in such a way. The initial solution with $(CO_2^0, 0)$ evolves along pathway 1, reaches the CO_2 input region, where its CO_2 concentration rises (marked by 2) and follows a new $CO_2 - Ca^{2+}$ line. Solutions at the CO_2 inputs can have various saturation ratios and can thus (3 and 4) be shifted to different $CO_2 - Ca^{2+}$ lines. The presence of CO_2 sources also induces mixing corrosion. We are not going to show and discuss the wide variety of cases when CO_2 inputs

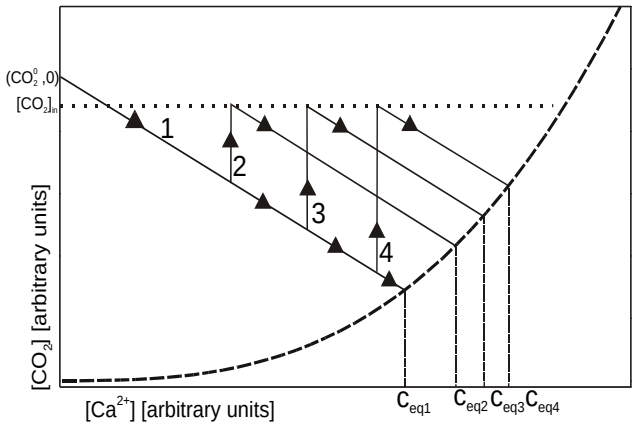

Figure 4.16: Chemical pathways of solutions in the presence of a CO_2 inputs

are introduced into the network. We point out just a few cases.

THE RESULTS

Fig.4.17 shows three stages in the evolution of a net, where a line source of CO_2 is introduced. The p_{CO2} in the region marked by a shaded rectangle in Fig.4.17a is set to $0.04\,atm$. $p_{CO_2} = 0.05\,atm$ at the inputs A and B. Otherwise the net is identical to the one presented in Fig.4.11.

Fig.4.17a shows the distribution of aperture widths and equilibrium concentrations after $1\,ky$. The shift of c_{eq} due to the CO_2 inputs causes a growth of the conduits in the lower right part of the net. Close to the output the solutions from both inputs mix. Their different chemical composition initiates mixing corrosion and therefore the growth of conduits (green) in the mixing zone.

At $1.9\,ky$ (figure b), the set of conduits initiated by the CO_2 input and mixing corrosion join, and offer a shortcut for the pathway connecting the input B and the output. The breakthrough along this pathway occurs at $2.4\,ky$ (Fig.4.17c). Fig.4.17d shows the distribution of hydraulic heads at 2ky (figure b). Note the high hydraulic gradient in the region of CO_2 input.

Fig.4.18 presents the evolution with a localised CO_2 input (denoted by shading). The other parameters are the same as for the net presented in Fig.4.3. Figure a shows the net at 1.5ky. A set of conduits has evolved between the CO_2 input and the output. Conduits also evolve due to mixing corrosion at the boundaries of the region with different c_{eq}. Fig.4.18b shows the situation at the breakthrough (2.3ky). The pathway from the middle input has joined the pathway evolving from the CO_2 input to the output. The drop of head along this pathway also attracts the pathway leading from the uppermost input.

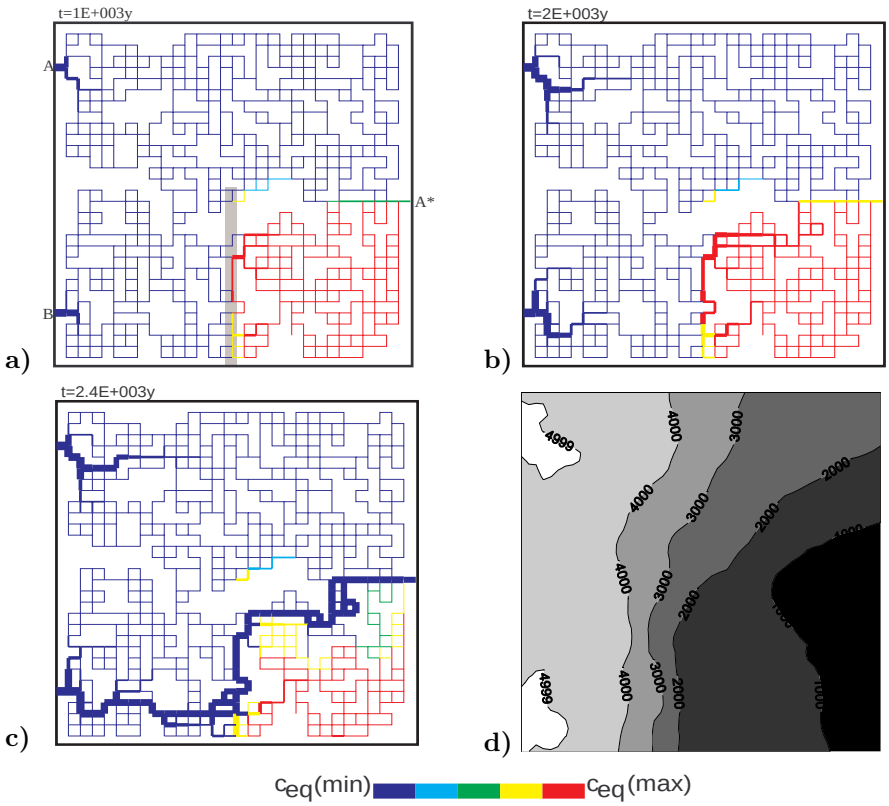

Figure 4.17: Net with a line input of CO_2. In the region shaded in figure a the p_{CO_2} is fixed to $0.04\,atm$. **a,b,c)** Aperture widths and equilibria at 3 different time steps as denoted on the figures. Fig c shows the breakthrough scenario. **d)** The distribution of the hydraulic heads at 2ky.

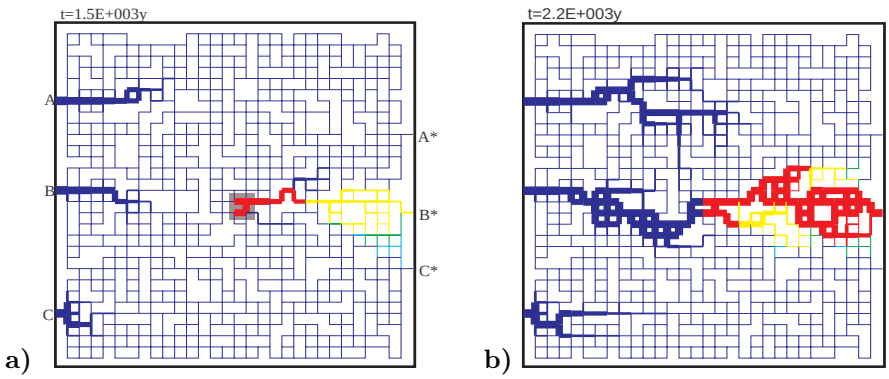

Figure 4.18: Two steps at 1.5ky (**a**) and at the breakthrough (**b**) in the evolution of the net with constant $p_{CO_2} = 0.05\,atm$ region. This region is marked by the gray shade in figure a. Otherwise the net is identical to the one presented in Figs.4.3-4.6.

5 TOWARDS MORE COMPLEX MODELS: THE EVOLUTION OF EARLY KARST IN THE DIMENSION OF LENGTH AND DEPTH

5.1 INTRODUCING NEW CONCEPTS

In the models presented so far were calculated under constant head conditions[1] . Only flow in prominent fractures with initial aperture widths of several tenths of a millimetre was considered.

The concepts of matrix flow and typical conductivities in early karst were introduced in Chap.1. This chapter gives a more comprehensive picture of early karstification by considering also the flow and dissolution in the matrix which is represented by a dense fracture system. Besides this, the more "natural" boundary condition of constant recharge to the aquifer is introduced. The modelling domain remains two-dimensional, representing a vertical section of a limestone plateau.

5.2 THE MODELLING CONCEPTS

5.2.1 THE MODEL AND ITS PARAMETERS

Fig.5.1a shows a vertical section of a limestone plateau downcut by the valley on its right-hand side. The massif is dissected by fractures of various initial apertures. Prominent fractures are shown in the massif. An enlargement shows a net of fine fractures which represent the "matrix" part of an aquifer. Fig.5.1b shows a simplified version of the cross-section representing the modelling domain discussed in this chapter.

[1] Exception is the one in Sec.3.6, where a constant recharge was assumed.

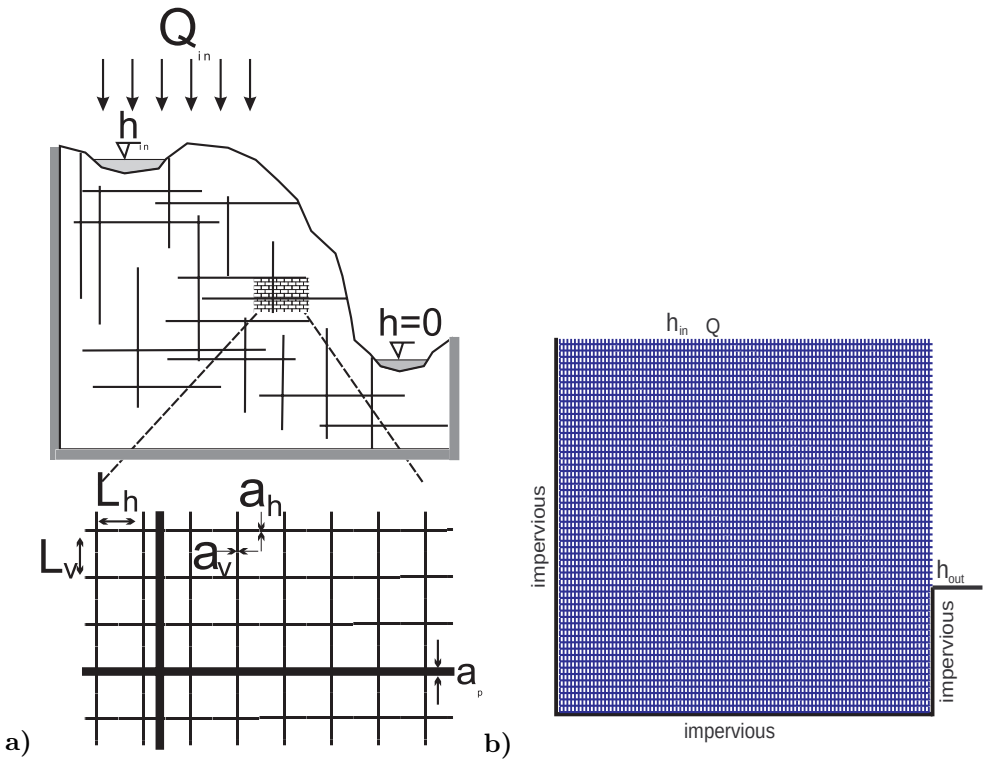

Figure 5.1: **a)** Schematic representation of a cross-section through the limestone plateau. At the top a combination of constant recharge and constant head conditions can be applied. Thick gray lines show impermeable boundaries. The lower picture is an enlargement showing the parameters of the fracture systems. **b)** The model aquifer with its boundary conditions.

The model plateau is rather small, 200m long and 30m high[2]. The matrix conductivity is represented by a rectangular net of fine fractures with aperture widths $a \approx 0.005\,cm$. Prominent fractures with aperture widths in the order of few tenth of a millimetre can be incorporated into the matrix. A recharge of 450mm/year is evenly distributed at the surface of the plateau and "offered" to the aquifer.

The left-hand side, the base and the lower right-hand side are assumed impermeable. This is marked by thick solid lines in Fig.5.1b. The hydraulic head h_{out} at base level is set to zero. The cliff on the right represents a seepage zone where the water leaks from the aquifer. Constant head conditions can also be applied on the top , e.g. an allogenic river flows over the massif. Tab.5.2.1 presents the new parameters used in the model and their typical values.

[2]The primary goal was to present a larger scale model, but this remains a future job due to numerical problems and limited computational power.

Name	Sign	Typical value	Units
Aperture width of prominent fractures	a_p	0.02	cm
Width	b	100	cm
Aperture widths of horizontal "matrix" fractures	a_h	0.007	cm
Spacing between horizontal "matrix" fractures	s_h	50	cm
Aperture widths of vertical "matrix" fractures	a_v	0.006	cm
Spacing between vertical "matrix" fractures	s_h	200	cm
Recharge to the aquifer	Q_{in}	450	$mm/year$
Length of the massif	L	200	m
Thickness of the massif	D	30	m

Table 5.1: Basic parameters and their "standard" values

5.2.2 BASIC EQUATIONS AND BOUNDARY CONDITIONS FOR GROUNDWATER FLOW

To get a better understanding of the following results, we give a quick review of water flow in porous aquifers. The flow of water in porous media is described by Darcy's law and the continuity equation. Darcy's law relates the velocity (i.e. flow density) of the water to the hydraulic gradient:

$$\vec{v} = -\mathbf{K}\nabla h, \tag{5.1}$$

where $\mathbf{K}$ is the hydraulic conductivity tensor. The hydraulic head[3] is explicitly defined as the sum of the kinetic energy, the pressure and the potential energy. The kinetic energy can safely be neglected for the cases of our interest, therefore we obtain:

$$h = \frac{p}{\rho g} + z. \tag{5.2}$$

Neglecting the non-diagonal values of $\mathbf{K}$, the following relations are valid for the Cartesian coordinate system:

$$v_x = -K_x \frac{\partial h}{\partial x}, \quad v_y = -K_y \frac{\partial h}{\partial y}, \quad v_z = -K_z \frac{\partial h}{\partial z}. \tag{5.3}$$

The continuity equation for incompressible fluid gives $\nabla \vec{v} = 0$. Coupling it with Eq.5.1 one obtains:

$$\frac{\partial}{\partial x}\left(K_x \frac{\partial h}{\partial x}\right) + \frac{\partial}{\partial y}\left(K_y \frac{\partial h}{\partial y}\right) + \frac{\partial}{\partial z}\left(K_z \frac{\partial h}{\partial z}\right) = 0 \tag{5.4}$$

Note that for an isotropic conductivity the equation becomes Laplace's equation, i.e. $\Delta h = 0$.

The following boundary conditions apply to our model :

1. **Impermeable boundary:** This condition is satisfied by setting $\partial h/\partial n = 0$, where n is the normal direction with respect to the boundary.

[3] Also groundwater head, piezometric head or groundwater potential

2. **Boundary condition at the water-table:** $h = z$.
3. **Boundary condition at the seepage face**[4]**:** $h = z$.

Our model is discrete, i.e. flow is defined by a set of linear equations which relates the heads at the node points to the resistivities of the fractures connecting the node points. The solution is obtained in the same way as described in Chap.4.

Eq.5.4 is, except for the most simple cases, solved numerically. An ansatz for the finite differences model (Bear, 1979) gives a similar set of equations as we get for the discrete fracture system. In fact, if conductivities are taken as

$$K_x = K_h = \frac{\rho g a_h^3}{12\eta s_h} \quad \text{and} \quad K_z = K_v = \frac{\rho g a_v^3}{12\eta s_v}, \tag{5.5}$$

one obtains a set of equations identical to that of a discrete fracture system. The conductivities given in Eq.5.5 can also be interpreted as conductivities of a discrete fracture system, averaged over the surface between the two fractures. Therefore when taking a domain with a large number of fractures, its "continuum" conductivity is given by Eq.5.5.

Our model implies an unconfined aquifer, i.e. an aquifer with a water table (WT) [5] which divides a saturated phreatic and an unsaturated vadose zone (see Fig.5.1). Recharge is infiltrating through the surface and the vadose zone down to the phreatic zone at the WT. The position of the WT depends on recharge.

5.2.3 NUMERICAL PROCEDURE

The general procedure is similar to the one described in Chap.4. For each timestep the flow within the saturated zone is calculated and the transport dissolution model is applied to the fractures.

To obtain the flow through the fractures, the position of the WT must be known, since it defines the boundary conditions for flow and separates the saturated zone from the unsaturated one.

The position of the WT and the height of the seepage face is calculated by the following procedure:

1. An initial guess for the WT is assumed.
2. A recharge defined by precipitation is equally distributed to the points of the assumed WT.
3. The heads of all the net-points below and at the assumed WT are calculated with the boundary conditions defined by the assumed WT and seepage face.

[4]The condition at the water-table (abbrevated as **WT**) and seepage face is $h = z + p_{atm}/\rho g$. The second term is acting on all faces and can thus be subtracted

[5]Expression free surface or phreatic surface is also used

4. The heads of the points on the WT are checked for the boundary condition. Their head must, within a given error, equal to their elevation. In our case this condition yields $h = z \pm s_h/2$. If the condition for the point is valid, the WT is kept there, otherwise the WT is either shifted to the point above if $h > z + s_h/2$ or to the point below if $h < z - s_h/2$. Thus a new approximation for the WT is obtained.
5. Procedure 1-3 is iterated until all the points on the assumed WT fulfil the condition $h = z \pm s_h/2$.

Once the WT and the seepage zone are obtained, the flow through the fractures in the phreatic zone is calculated and the transport-dissolution model is applied. This is done in the same way as described in Sec.4.1. In this case the widening of each fracture in a timestep is not calculated by the finite difference procedure, but according to the widening rate at the exit:

$$a_i(t + \Delta t) = a_i(t) + 2\gamma F(L, t). \tag{5.6}$$

$F(L, t)$ is the dissolution rate at the exit of a fracture calculated by Eq.3.20. This approximation is not crude, since most of the fractures have high initial saturation ratios and the rates along them do not change much. Results obtained by using the finite differences procedure for each fracture are almost identical. The reason for the approximation is purely technical since it saves calculation time and memory usage.

Chemical parameters used are those given in Tab.3.1. During percolation through the vadose zone, the solution already attains some saturation state. This is taken into account by taking c_0 between c_s and $0.97c_{eq}$, so that the initial concentration rises linearly with the depth of the water-table. The choice of the parameter c_0 is rather arbitrary. It influences the evolution of an aquifer, but does not change the results conceptually. A broad sensitivity analysis has not yet been done.

5.3 RESULTS

5.3.1 NO PROMINENT FRACTURES: THE EVOLUTION OF A FINE FRACTURE SYSTEM

CONSTANT RECHARGE

The aquifer consists only of a fine fracture system to which the condition of constant recharge at the top is applied. No prominent fractures are present in the modelling domain.

Fig.5.2a shows the situation at 50y which is practically identical with

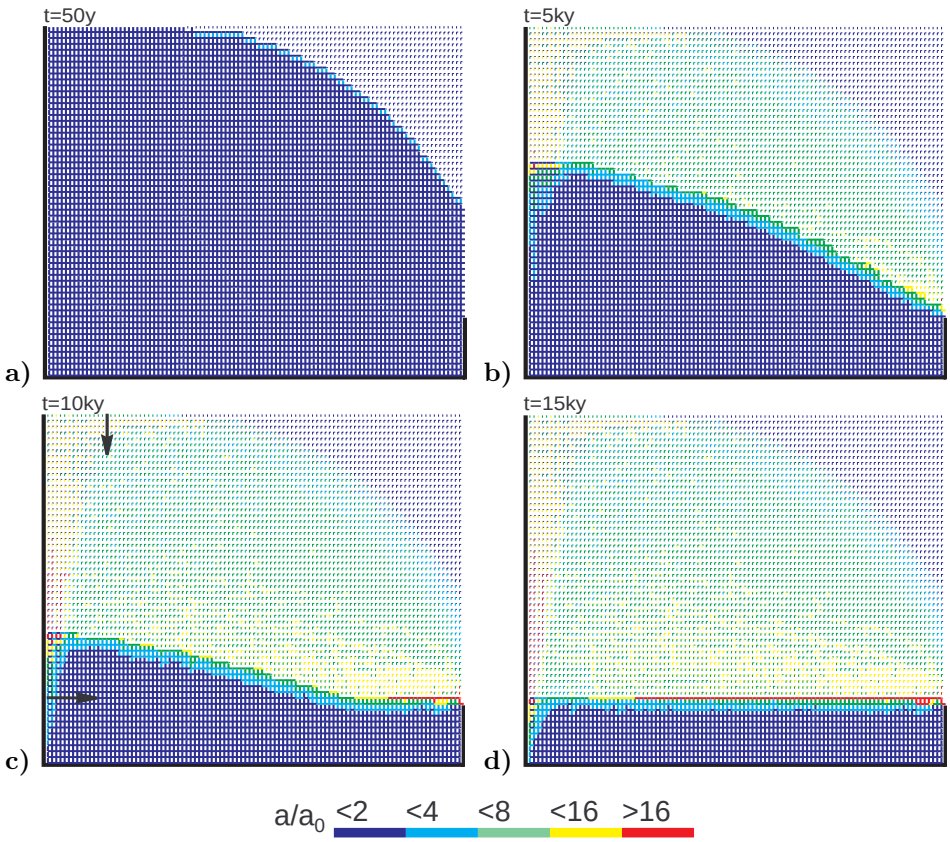

Figure 5.2: Evolution of an aquifer with evenly spaced fine fractures and constant recharge. Distribution of fracture widths after 50y (**a**), 5ky (**b**), 10ky (**c**) and 15ky (**d**). The colours represent the widths of the fractures in units $a(t)/a_0$, where a_0 is the initial width of vertical fractures ($a_0 = a_h(t = 0)$). Fractures designated by full squares represent the phreatic zone, those by open angles the vadose zone. The water-table is thus clearly presented.

the initial one. The phreatic zone is indicated by fat fracture lines, and the vadose zone by thin interrupted ones. In this way the position of the WT is clearly presented. The colours show the fracture aperture widths increasing from dark blue to red as denoted in the figure. a_0 is the initial width of the vertical fractures. Fig.5.2b shows the situation after 5ky. WT has dropped due to the increasing fracture widths in the aquifer.

After 10ky the WT reaches the lowest possible output fractures. This is presented in Fig.5.2c. A conduit develops by continuous dissolution along the base level and grows headwards (Fig.5.2d) until it reaches the left boundary after 20ky. Inspection of the colours in Fig.5.2 reveals that the hydraulic conductivity increases by about 2 orders of magnitude, leaving a highly permeable vadose zone as is observed in nature (cf. Eq.5.5). Dissolutional widening is most active close to the water-table at all times,

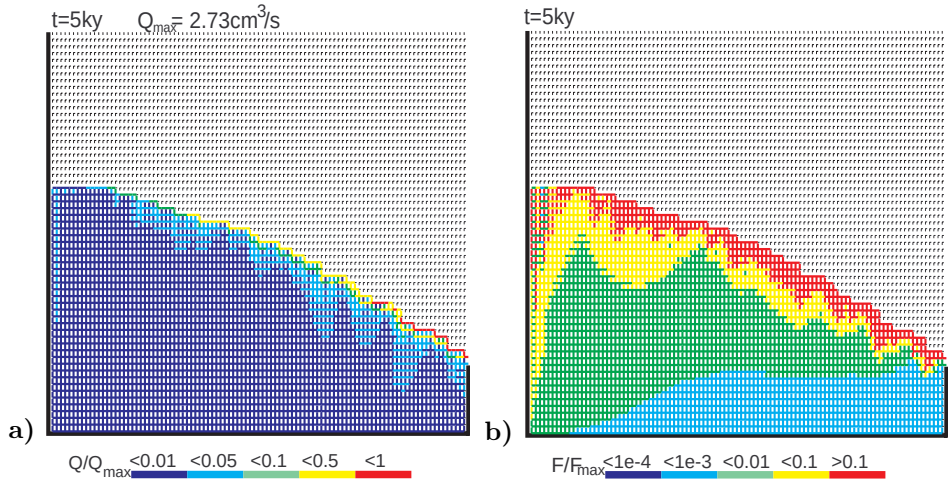

Figure 5.3: . **a)** Flow rates in units of Q/Q_{max} at 5ky. The fracture with the highest flow rate has a ratio of Q/Q_{max} equal to 1. Most of the flow is concentrated to the permeable fringe at the top of the phreatic zone. Confer to Fig.5.2b. **b**) Dissolution rates in units F/F_{max} where $F_{max} = 4 \cdot 10^{-12} molcm^{-2}s^{-1}$ corresponding to bedrock retreat of few $10^{-3} cm/year$. The maximal dissolution rates are active close to the water-table and drop rapidly with depth.

since the solution quickly approaches equilibrium when penetrating into the net. Therefore close to the WT a narrow region of higher permeability is established which attracts flow. In Fig.5.2a a small light blue fringe indicates this zone. Later the fringe becomes wider and is composed of fractures with apertures up to $16a_0$. With increasing time the water-table drops, leaving behind the vadose region of increased conductivity. The phreatic zone below still has low hydraulic conductivity. In such an aquifer most of the flow is directed along the water-table. Fig.5.3a shows the flow rates through the fractures at 5 ky and clearly illustrates (green, yellow, red

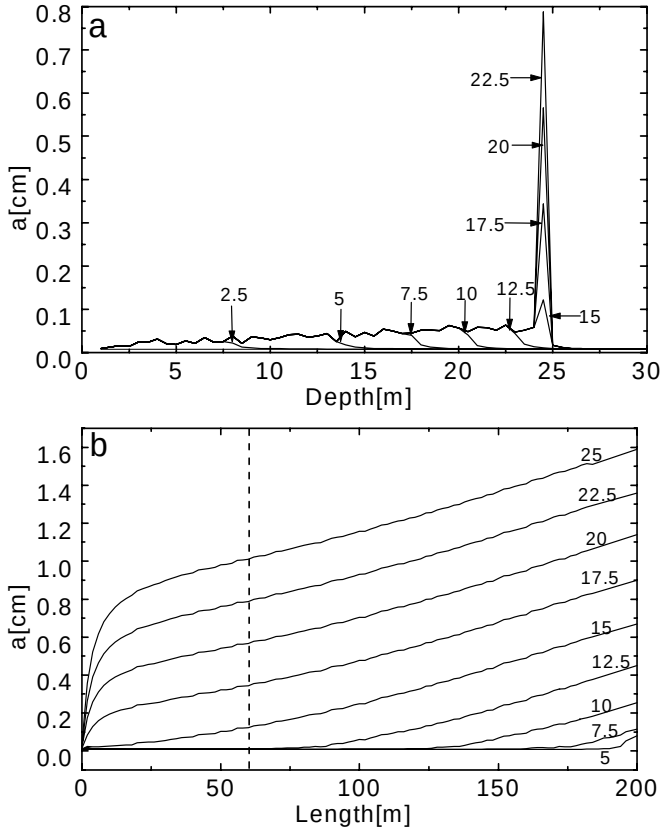

Figure 5.4: **a)** Profiles of the aperture widths of the horizontal fractures at various times along a vertical cross-section marked by an arrow in Fig.5.2c . A front of increased permeability with fracture widths of several hundreds of a cm penetrates downward. This front is marked by arrows. Numbers give the time in ky. **b)** Evolution of the aperture widths of the conduit at base level (cf. Figs.5.2c,d). Numbers at the curves denote time in ky. Initial width is $7 \cdot 10^{-3}$cm. The conduit starts to grow headwards at 7.5ky and shows a linear increase of its width in time. The dashed vertical line marks the position of the vertical profile shown in Fig.5.4a.

fractures) that the flow is restricted close to the water-table. Dissolution rates shown in Fig.5.3b also exhibit a maximum close to the water-table and drop significantly below. As the water-table drops dissolution becomes active in the lower parts of the aquifer. Once the water-table has reached a stationary position dissolution stays active close to it and large conduits can grow. This corresponds to the ideal water-table cave in the model of Swinnerton (1932) and Rhoades and Sinacori (1941) which requires a high and even fissuring of the rock.

To illustrate the distribution of fracture widths in the net Fig.5.4a shows the aperture widths of the horizontal fractures in relation to the distance from the top of the aquifer for various times. The distribution of fracture

widths, taken along column 30, as indicated by an arrow in Fig.5.2c is shown in Fig.5.4a. At time zero all fractures show initial widths of $0.007\,cm$. Since dissolution occurs only close to the water-table a region of widened fractures with an average width of about $0.03\,cm$ propagates into the rock down to the position of the actual water-table.

This high permeability characterizes the vadose zone. Further dissolution by water trickling down this zone is not considered in our model. After 10ky the zone of widened fractures has dropped further until after 15ky the water-table has reached the lowest horizontal fracture at the seepage face (cf. Fig.5.2d). From then on this fracture widens continuously as depicted by the curves. A similar behaviour is observed for the vertical fractures, not shown here.

Fig.5.4b shows the evolution of the horizontal fracture widths along the final water-table. The spring is at the right-hand side. As soon as the WT has reached the spring, a conduit starts to grow headwards from the spring into the aquifer. As the intersection of the water-table and the horizontal fracture moves headwards the recharge is drained by the spring side part of the fracture, and the conduit widens at an almost constant rate. This explains the linear profiles. Finally when the water-table coincides with the entire fracture, we have the case of a one-dimensional conduit with evenly distributed recharge presented in Sec.3.6.

The presented concept of karst evolution shows that the evolution of highly permeable aquifers including large conduits at the final position of the water-table is possible even in the case of an initially evenly fractured limestone without prominent fractures. Such prominent fractures were a necessary ingredient of the models presented so far in this and also in other works.

COMBINED CONDITIONS: CONSTANT RECHARGE AND CONSTANT HEAD

Often constant head boundary conditions and those of constant recharge exist simultaneously. This for example is the case when allogenic rivers are present. Fig.5.5 shows such a case where a constant head equal to the elevation at the upper left boundary is imposed (see Fig.5.5a). Other parameters are equal to those in Fig.5.2. Constant recharge is offered to the aquifer everywhere else. Fig.5.5a shows the water-table and the distribution of the fracture aperture widths 1ky after the initial state. In the region of constant recharge the water-table drops as in the previous case. Dissolution occurs only in a small banded region close to the WT as illustrated by Figs.5.5a, b, c. In the constant head region, the water-table cannot drop below the surface, therefore the head difference along the WT increases. A permeable fringe along the WT offers an effective pathway draining the

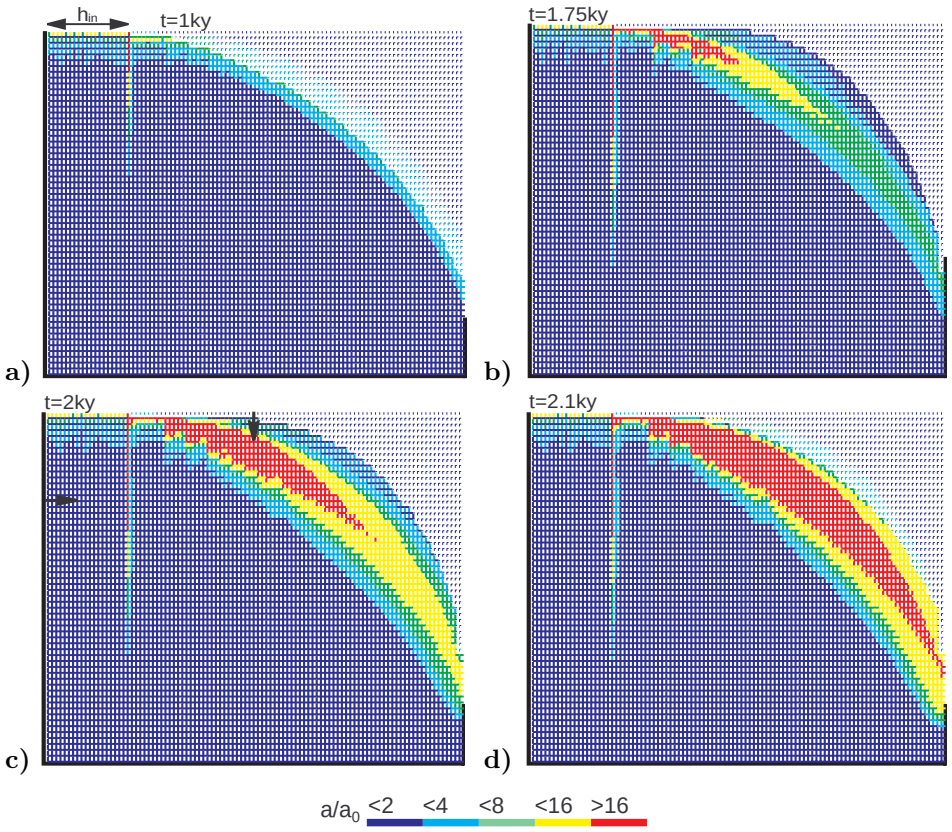

Figure 5.5: Evolution of a fine fracture system with combined constant recharge and constant head conditions at the top. The constant head region is marked in figure a. The WT is fixed due to the constant head. Dissolution is mainly active in the fringe close to the water-table. The arrows on figure c denote the position of the profiles presented in Fig.5.6.

water from the constant head region to the output. The feedback mechanism along this pathway leads to the breakthrough at 2.1 ky. A wide zone of high conductivity has been created which carries flow from the constant head area. Fig.5.7 shows the total discharge as a function of time. The arrows indicate the flow rates at the timesteps from Fig.5.5.

This resembles a typical breakthrough behaviour such as observed for one-dimensional conduits or for nets under constant head conditions as presented in Chaps.3 and 4. To obtain same quantitative information on the widths of the fractures Fig.5.6 exhibits the distribution of widths along a vertical and horizontal cross section through the aquifers as indicated in Fig.5.5c for various times.

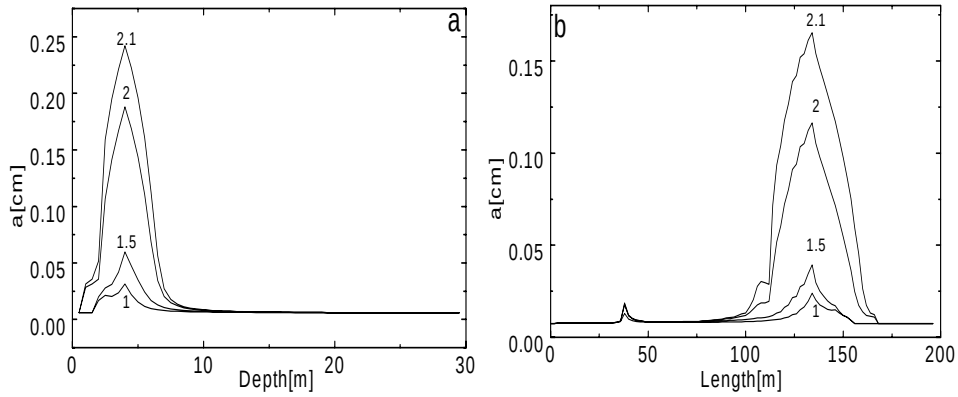

Figure 5.6: Distribution of the fracture widths for a horizontal and vertical cross-section of the aquifer as indicted by arrows in Fig.5.5a. **a)** Widths of the vertical fractures in the vertical cross section for various times indicated in ky. The region of maximal widths corresponds to the red area in Fig.5.5. **b)** Widths of the horizontal fractures in the horizontal cross-section for various times. The small peak at about 30m corresponds to the vertical channel which develops at the border between constant head and constant recharge regions. Note that the increase of aperture widths accelerates in time.

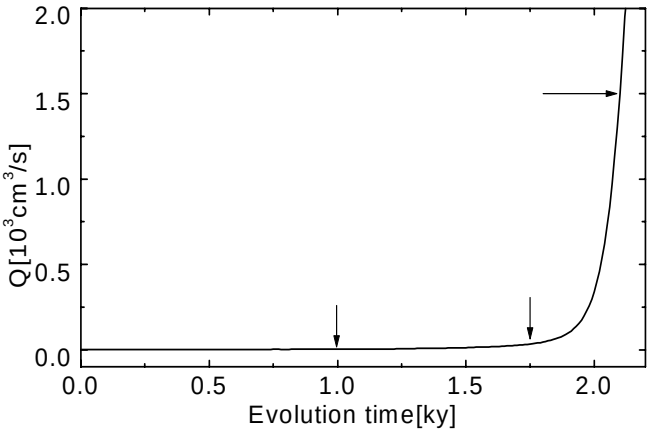

Figure 5.7: Flow through the aquifer of Fig.5.5 as a function of time. Typical breakthrough behaviour is observed. The arrows indicate the times of Fig.5.5a,c and c.

5.3.2 AQUIFERS WITH PROMINENT FRACTURES

Although we pointed out that the conduits can grow also without prominent fractures, it is well known that caves in natural karst are guided along the prominent bedding planes and joints (Ford and Williams, 1989). Therefore we will extend the model by first adding a single prominent fractures into the "matrix" and later introducing a network of prominent fractures.

MATRIX WITH A PROMINENT FRACTURE UNDER CONSTANT RECHARGE CONDITIONS

We first include one prominent bedding plane, with a width of 0.025cm into the aquifer of at base level. Fig.5.8 illustrates the position of the water-table at various times. The bedding plane indicated by a grey line extends along the entire length of the aquifer. In comparison to Fig.5.2a a significant drop of the initial WT below the surface of the aquifer is observed, since the prominent horizontal fracture receives vertical flow and conducts it to the exit.

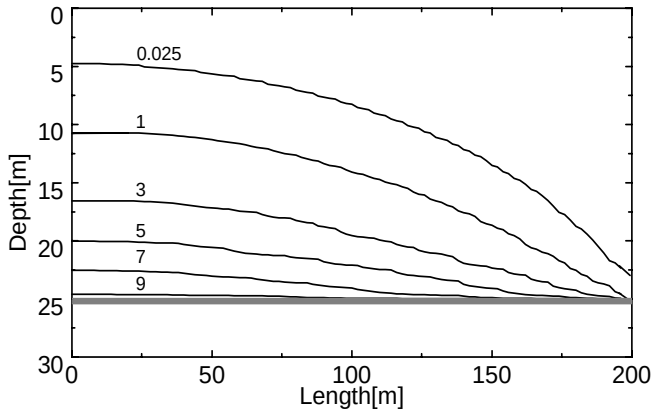

Figure 5.8: Position of the water-table at various times for an aquifer with one prominent fracture with an aperture width of 0.025cm. The position of fracture is marked by the grey line. The numbers on the curves indicate time in ky.

After 5ky the WT has reached this fracture and at 10ky it coincides completely with it. The evolution of the aquifer is generally similar to that in Fig.5.2 but much faster. We have also modelled a case where a vertical fracture of 0.025 cm aperture width is added to the aquifer so that it intersects the horizontal one. This does not have any significant influence on the evolution of the aquifer.

A SIMPLE PATHWAY OF PROMINENT FRACTURES

Now a pathway of few prominent fractures with widths of $0.04\,cm$ is added to the matrix. It penetrates below base level and is terminated there after a loop as shown in Fig.5.9. The pathway does not connect inputs to the outputs.

Initially the WT is high as depicted by the dashed line in Fig.5.9a, which illustrates the aquifer at 5ky. A relatively high hydraulic head acts along the pathway, which widens similarly as under constant head conditions. As the WT drops the head and the effective length of the pathway drop, since the upper part is becoming vadose. These two effects partially compensate each other. Water leaking from the pathway into the the matrix at the right-hand end of the loop creates a permeable region spreading in the direction of the output. It takes about 10ky until the WT reaches the base level (Fig.5.9b).

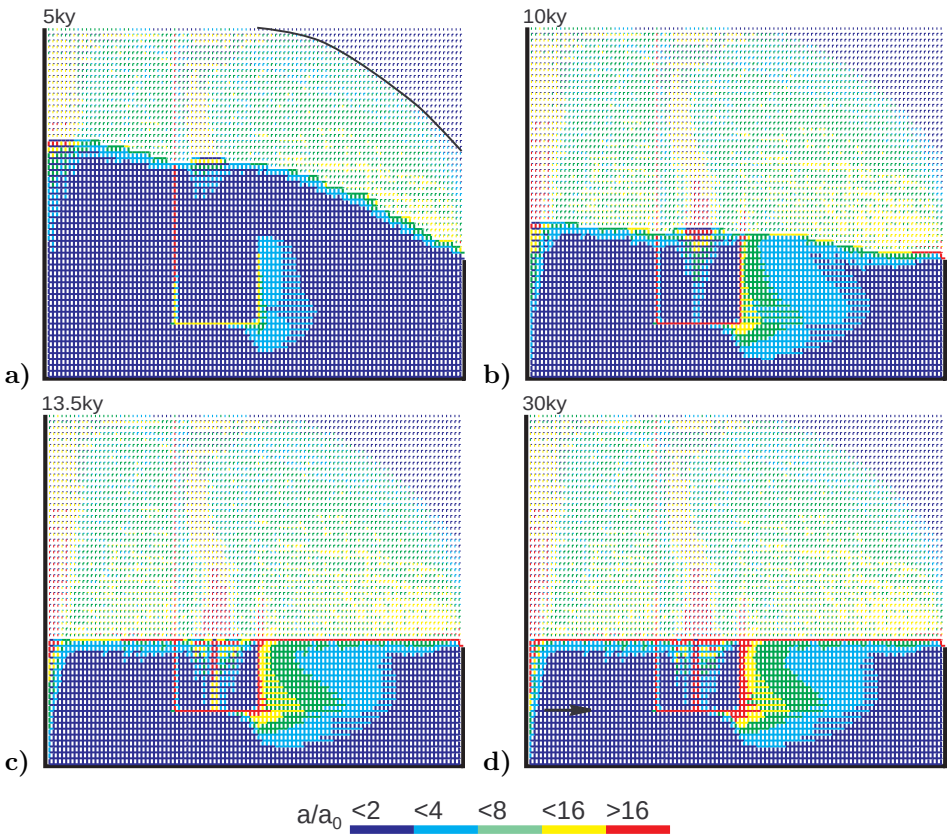

Figure 5.9: Evolution of an aquifer including a pathway of prominent fractures ($a_p = 0.04cm$). The pathway is composed of two vertical and one horizontal part and can be well seen on the figures. It does not connect the inputs to the ouputs, since it terminates in the matrix.

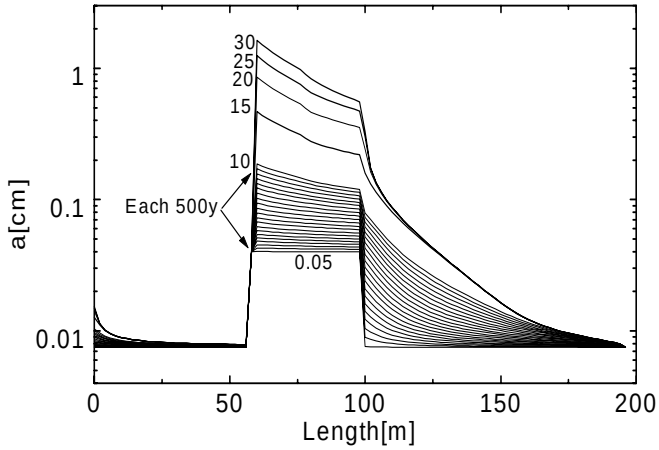

Figure 5.10: Aperture widths along the horizontal cross-section marked by the arrow in Fif.5.9c. The cross section contains the horizontal part of prominent fracture between $60\,m$ and $100\,m$.

Fig.5.10 shows at various times the distribution of fracture aperture widths of the horizontal fractures along the cross-section containing the horizontal part of the prominent pathway. Until 10ky the prominent horizontal fracture widens in time similar as under constant head conditions. After 10ky, when the WT is at the base level, it widens linearly in time. The breakthrough behaviour for this case is quite complex. Since the pathway ends in the matrix, breakthrough could occur if the permeable zone right to the pathway reaches the output. This could happen only if the high hydraulic head conditions last long enough, i.e. if the WT is kept above the base level for longer time. Increasing permeability causes the drop of the WT and annihilates its own progress.

After 13ky a conduit has propagated at the base level headwards from the spring (Fig.5.9c). At the left-hand side of the vertical fracture another conduit grows headwards also at the base level (Fig.5.9b). Since the loop of the prominent fracture below base level has evolved to a width of about 3mm, this loop effectively drains water flowing along base level from the left hand side. After about 15ky years (not shown here) the entire flow is directed along the water-table at the left side. From there it flows through the short-circuiting loop and then again along the water table to the spring. A conduit continues to grow along this stable flow path.

A PROMINENT FRACTURE IN THE CONSTANT HEAD REGION

If prominent fractures connecting the region of constant head to the output are present, the evolution of such fractures is close to the evolution of

a single fracture under constant head. On the other hand a breakthrough behaviour along the water-table is also present (see Fig.5.5), thus a competition between these two pathways is to be expected.

Such a situation is shown in Fig.5.11, where a vertical and horizontal fracture of $0.03\,cm$ aperture widths connects the region of constant head to the spring.

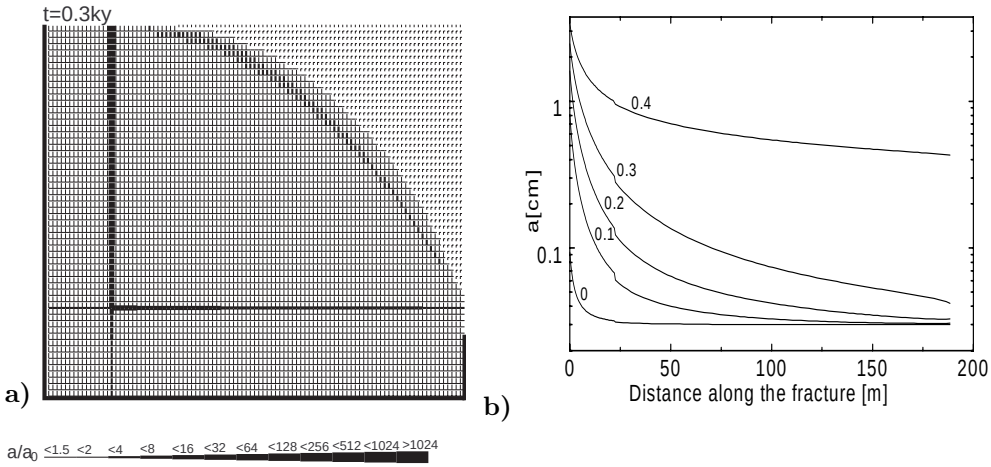

Figure 5.11: **a)** Distribution of fracture widths at breakthrough for the matrix with two additional prominent fractures with an aperture width of $0.03\,cm$ connecting the region of constant head to the output at base level (t=300 years). **b)** Profiles of the aperture along the prominent fracture in the aquifer for various times indicated by the numbers on the curves (given in ky). Input at $0\,m$, spring at $190\,m$.

The other parameters are equal to those shown in Fig.5.5. Fig.5.11a illustrates the distribution of aperture widths after $300\,y$ when breakthrough through the prominent fractures occurs. The small fringe of enlarged fractures close to the water-table indicates that the evolution of this pathway needs a much longer time (cf. Fig.5.5). Fig.5.11b depicts the width profiles of the single conduit along the prominent fracture for various times. After the breakthrough, constant recharge conditions must be assumed for the prominent fracture, draining all the recharge in the former area of constant head. Correspondingly the water-table will decline in a similar manner to the situation in Fig.5.2, leaving a vadose zone of increased conductivity. The further evolution of the conduit will be determined by a constant recharge to it.

5.3.3 AQUIFERS WITH A NET OF PROMINENT FRACTURES

Up to now we have added only a few simple prominent fractures into the matrix represented by the dense fracture system. To create a more realistic karst aquifer we now superimpose a net of prominent fractures to the matrix. The following procedure is used:

- Divide the net of fine fractures into a coarse net of 5 by 5 dense fractures
- With a random procedure assign to each fracture of the coarse net an aperture width of a prominent fracture a_p. If the random number chosen for each fracture is smaller than p, the fracture has an aperture width a_p, else its aperture is that of the fine net fractures.

This initial scenario is similar to the approach of a double continuum model of Clemens et al. (1997a),(1997b), (1999) but it avoids calibration parameters, which are difficult to specify. It is also close to the approach of Kaufmann and Braun (1999b) who model the initial aquifer by a superposition of a prominent fracture net to a rock matrix with homogeneous initial conductivity.

The most important difference in our approach is that dissolutional widening is regarded in both parts of the aquifer, whereas Clemens et al. and also Kaufmann and Braun disregard dissolution in the dense fractures or matrix respectively.

CONSTANT HEAD AND CONSTANT RECHARGE CONDITIONS

The boundary conditions for the case in Fig.5.12 are the same as in Fig.5.5: constant head at the left-hand upper side and constant recharge on its right-hand side. Fig.5.12a shows the widths close to the onset of the evolution after 200 years. After 1ky a complex net of conduits has developed along the prominent fractures. The region of constant head becomes connected to the area of constant recharge by increasing conductivity, caused by both, widening of the fine fractures and also connection to the prominent ones. Consequently the water-table rises. Close to the water-table a region of higher conductivity connects the prominent fractures to the seepage face. This change of conductivity and hydraulic heads enhances the evolution of the conduits along the prominent fractures.

After 1.2 ky breakthrough occurs, with prominent fracture widths in the order of a few millimetres. To illustrate the distribution of fracture widths as they evolve in time, Fig. 5.13 depicts these along a horizontal cross-section as indicated by an arrow in Fig.5.12c. The widening of the fracture accelerates by feedback and consequently the discharge through the aquifer shows the characteristic breakthrough behaviour. This event

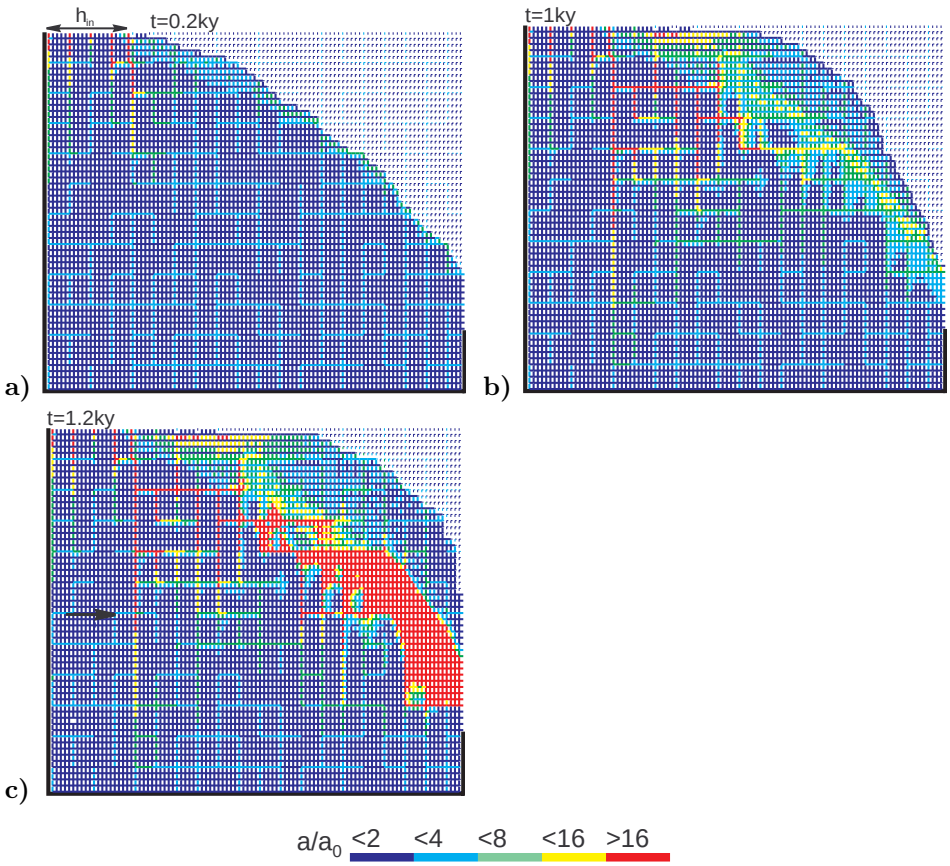

Figure 5.12: Evolution of an aquifer with a percolation network of prominent fractures appended to the dense fracture network. The initial aperture width of prominent fractures is 0.02cm (light blue). Other parameters are the same as in Fig.5.5. **a)** 0.200ky, **b)** 1ky, **c)** 1.2ky.

terminates the early evolution of the aquifer. The constant head condition breaks down and must be replaced by constant recharge. Flow becomes turbulent. Nevertheless, the complicated pattern of vertical and horizontal conduits and a high permeability region close to the spring will design the future structure of the mature karst aquifer. It should be stressed at that point, that constant head conditions are crucial for the evolution of such complicated structures as shown in Fig.5.12.

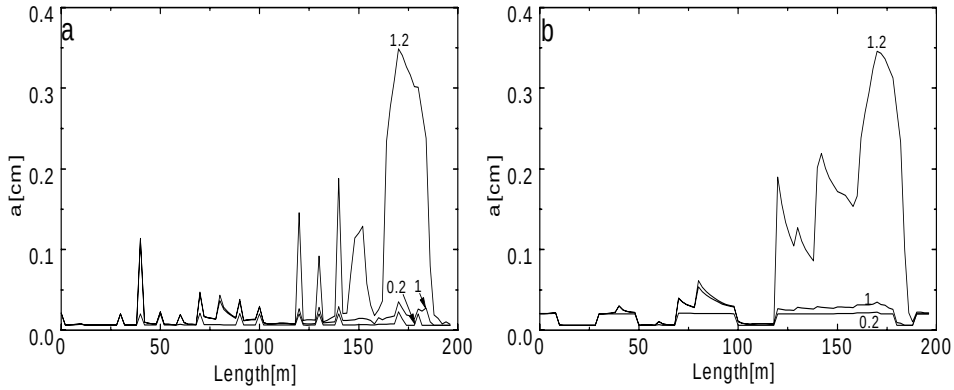

Figure 5.13: 11 **a)** Profiles of horizontal fracture widths along a horizontal cross-section as marked by the arrow in Fig.5.12c. **b)** Profiles of vertical fracture widths along this cross-section. Times in ky are given by the numbers on the curves.

THE CONDITIONS OF CONSTANT RECHARGE

Another case with a percolation net of prominent fractures is one with a constant recharge solely. The WT drops to base level as in all other cases of constant recharge. What makes the case interesting are the complex loops below base level evolving during the drop of the WT . The basic mechanism is similar to that for a simple pathway with a loop below the base level in Fig.5.9. The only difference is that in this case there are more loops, creating a more complex flow pattern. This is shown by Fig.5.14. It shows an aquifer with a network of prominent fractures (p=0.8) with aperture widths of $0.04\,cm$. To get a more pronounced pattern, recharge is increased to $700\,mm/year$. Fig.5.14a represents the fracture widths after $30\,ky$. Fig.5.14b depicts the flow rates and consequently the flow path at that time. These conduits which continue to grow below the water table are similar to those in Fig.5.9, but more complex.

TIME DEPENDENT BOUNDARY CONDITIONS: DOWNCUTTING OF THE CLIFF

In nature the boundary conditions are changing during the evolution of a karst aquifer. The precipitation rate Q, the chemical parameters of the inflowing solution and also the hydrological boundary conditions may alter. All these variations can also be applied to the model presented. We are going to leave most of this for the future, and present a few cases where the base level of an aquifer is downcut during the evolution.

In a first scenario we assume that a "sudden" incision of a valley lovers

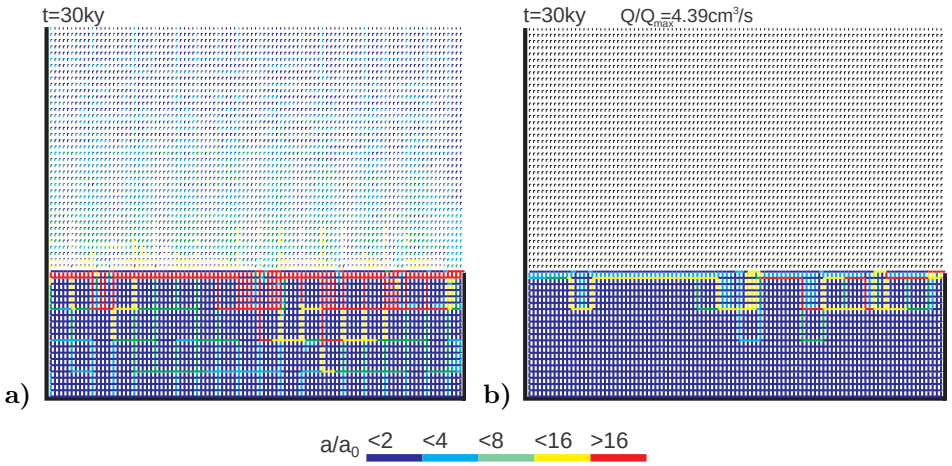

Figure 5.14: Aquifer with a percolating net of prominent fractures ($a_p = 0.04cm$). Annual precipitation is 700 mm/year. **a)** Distribution of fracture widths after 30ky. Conduits grow along the base level and along the phreatic loops. Note the change in the colour code with respect to other figures. The widths designated by red are above 0.5cm. The dashed line depicts the initial WT. **b)** Distribution of flow rates at 30ky.

the base level. This is presented by Fig.5.15. The model is the same as used in Fig.5.14 but the position of base level is kept at 15m during the first 10ky and than it is downcut to 25m immediately. In Fig. 5.15a, which shows the situation at 9.8ky, a water-table cave has developed and as in Fig.5.14 the system of conduits evolves below the base level.

After the downcutting the WT adopts to the new base level in a short time. This is presentes in Fig.5.15b. After 11ky (Fig.5.15b) a new water-table cave is already evolving. Between both base levels the conductivity is relatively small since the WT has dropped fast due to the phreatic loops which have evolved prior to downcutting.

Probably more realistic than the step downcutting is a gradual downcutting. Such a scenario is shown on Figs.5.16. The initial base level is almost at the top of aquifer and is being lowered in steps of two nodes (1m) every 5ky. The mechanisms are similar to those for the step downcutting. The formation of phreatic conduits below base level forces the WT to adapt promptly to the temporary base level. Fig.5.16a and b show the aquifer at 6ky and 12ky, respectively. The vadose zone exhibits a relatively high permeability[6] since the region of fast widening at the WT was gradually lowered together with the slow downcutting. A slower downcutting produces higher permeability in the vadose zone.

[6]Note (once more) that permeability of the vadose zone is only the relict of dissolution when the zone was still saturated and that the dissolution in vadose region is not considered

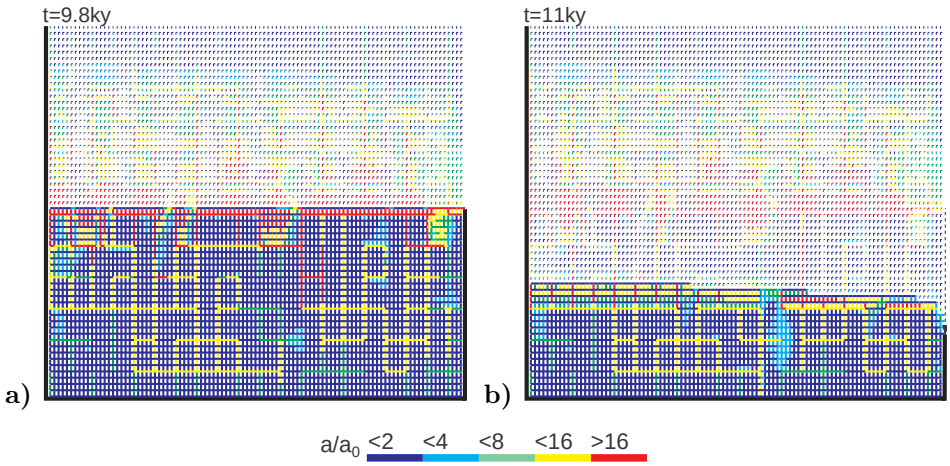

Figure 5.15: Evolution of an aquifer with a net of prominent fracture under constant recharge condition with step downcutting of the base level.

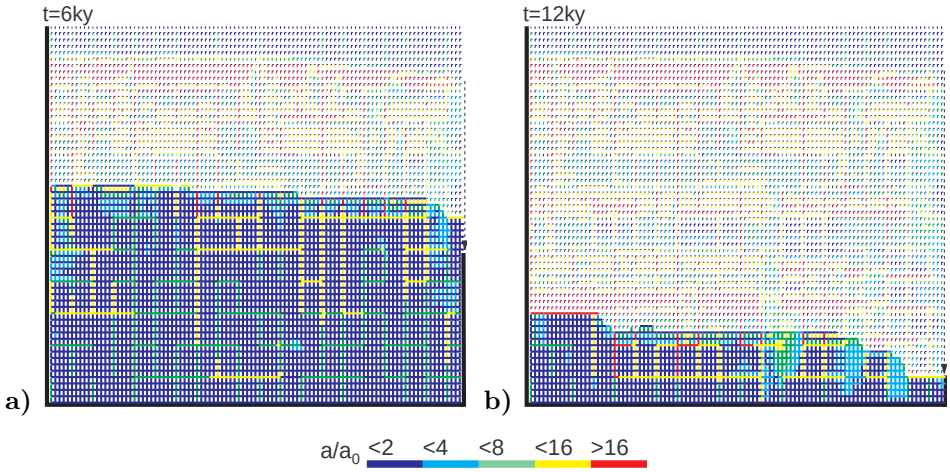

Figure 5.16: Evolution of an aquifer with a net of prominent fracture under constant recharge condition with gradual downcutting of the base level.

THE CASE OF LINEAR KINETICS

When discussing the evolution of a single fracture we have stressed the difference between non-linear and linear dissolution kinetics. The question arises, how does the aquifer we have just presented evolve if only linear kinetics acts? First we have to note, that the approximation with the widening by the exit rate is questionable here. In Sec.3.1.4 we stressed the importance of diffusion in the calculation with linear rate law. We also showed that the approximation with the exit rates gives wrong results.

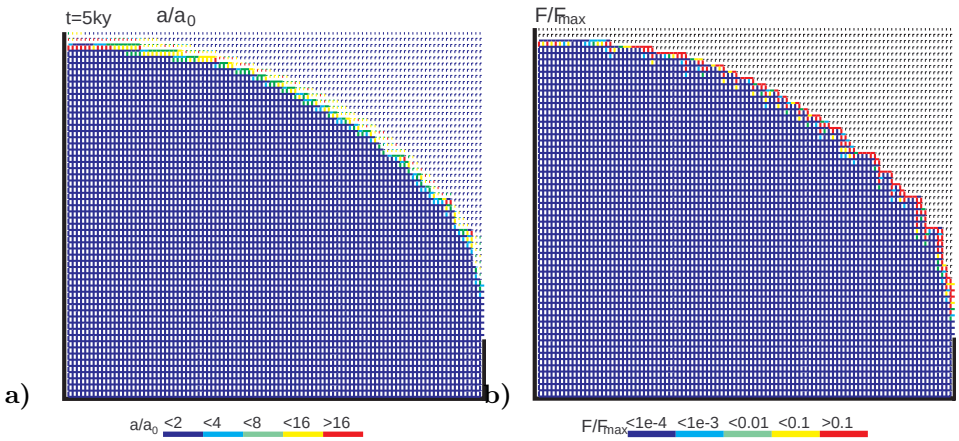

Figure 5.17: The case of linear kinetics. Fracture widths (**a**) and dissolution rates (**b**) at 5ky. The region of widening is restricted only to the WT.

Nevertheless, we present an example where only a linear rate law is applied, since it nicely demonstrates what happens if the penetration lengths are short.

This is also shown in Fig.5.17. The narrow fringe of high dissolution rates is even more bound to the water-table, so the fractures below the WT practically do not experience any widening. Therefore the drop of the water table is very slow, caused only by widening of fractures at the WT. In other words we can say that the result of linear kinetics is "surface denudation" of limestone at the water-table. The water-table drops very slowly in time and becomes steep close to the seepage zone. The steep water-table causes the failure of the algorithm which searches its position. For this reason the later stages are not shown - one more task for the future.

6 CONCLUSION AND FURTHER PERSPECTIVES

6.1 SOME BASIC RESULTS OF THIS WORK

Half of this work deals with the evolution of a single fracture under constant head conditions. This topic has been well discussed in literature, but it appeared that some important scenarios were not considered or were underestimated in the models presented so far. The evolution of the fracture changes dramatically if the parameters defining the dissolution rates change within the fracture. A change of the kinetic order or CO_2 inputs cause a considerable effect on breakthrough times. These effects are not only dependent on the magnitude of these changes, but also on the position in the fracture where they take place. Mixing of solutions with different chemical composition also belongs to this context; it is shown that mixing corrosion can contribute considerably to the initial karstification.

A deep understanding of the evolution of a single fracture is crucial for understanding the results of model runs on 2D fracture networks. In these, the chemically and mechanically most favourable pathway (the one with the lowest breakthrough time) wins the breakthrough race. The breakthrough behaviour of pathways in 2D networks is similar to that in single fractures. Nevertheless, the winning pathway is hard to predict once additional parameters like mixing corrosion and CO_2 sources are added to the model.

Chap.5 presents the evolution of a karst aquifer in its length and depth. Although most difficult to model, the basic results of these simulations are clear and easy to interpret. An absence of prominent fractures results in the evolution of water-table caves. In the presence of prominent fractures the competition between these and the fractures close to the water-table occurs. The results of the model support the empirical theories presented in the introduction.

6.2 FUTURE WORK

There is still a wide gap between the presented models and real karst systems. The difference between Fig.1.3 and Fig.1.1 in the introductory chapter points to this gap and to the main tasks for the future. With regard to our models these are:

1. To extend the model to turbulent flow conditions. This has already been done by the other modellers (see Howard and Groves (1995), Kaufmann and Braun (1999a), Clemens et al. (1997a)). After turbulent flow sets in, the head distribution changes within the fracture network. According to Groves and Howard Howard and Groves (1995) and Kaufmann and Brown Kaufmann and Braun (1999a), evolution under the turbulent flow conditions results in a more maze-like pattern of conduits.
2. To develop 3D models. The models presented are 2D sections of karst aquifers. The next step is to add a third dimension to the model presented in Chap.5.
3. To introduce more realistic and time-dependent boundary conditions. These should include uplifting, downcutting, variation of precipitation rates, hydraulic heads, geochemical conditions etc.
4. To introduce flow and dissolution in the vadose zone.

By **gradually** adding these new elements, one could "construct" a numerical karst aquifer from the basic principles **and** understand its nature and behaviour. One could numerically investigate the properties of such aquifers and compare them to field results obtained on the real aquifer.

More complex models could also reveal the the evolution of karst surface landforms such as solution dolines, cone and tower karst etc., since the evolution of these features is closely connected with the evolution of subsurface flow in karst aquifers.

6.2.1 A QUICK LOOK INTO THE FUTURE: DYE TRACING IN NUMERICAL AQUIFERS

For a "taste" we present the results of "dye tracing" in a 2D percolation network. We will perform a numerical tracing experiment in the network presented on Figs.4.3-4.6 in Sec.4.1. To put this in the frame of this work the tracing will be done at three different stages of the evolution; at 1ky, at 3ky and at the breakthrough.

We are solving the following problem. Consider a pulse of a dye introduced into the network at some point at time $t = 0$ (note that this is local time at some stage of the evolution of the network and not the time from the onset of the evolution). What we are looking for is the appearance of

the dye at some other point in the network, i.e. its time distribution there. In the case presented here the dye is introduced at input A as denoted on Fig.6.1 and observed at the inputs A*, B*, C*.

We apply a particle tracking technique to calculate the response to the tracer input. A similar procedure was used by Moreno et al.Moreno et al. (1988) and Moreno and Tsang Moreno and Tsang (1991) to simulate the tracer transport in a single fracture with statistical distribution of the aperture widths. The procedure is done the following way: at input A, a pulse comprising a large number of particles is introduced at time $t = 0$. The pathway of each particle is determined statistically according to the distribution of flow; at each node a particle enters one of the fractures draining the flow from the node. The probability that a particle enters some fracture i is given by:

$$P(i) = Q(i)/\sum_j Q_j, \tag{6.1}$$

where Q_i is the flow from the node to the fracture i and $\sum_j Q_j$ is the whole flow from the node.

Each particle comes to one of the outputs A*, B* or C*, depending on

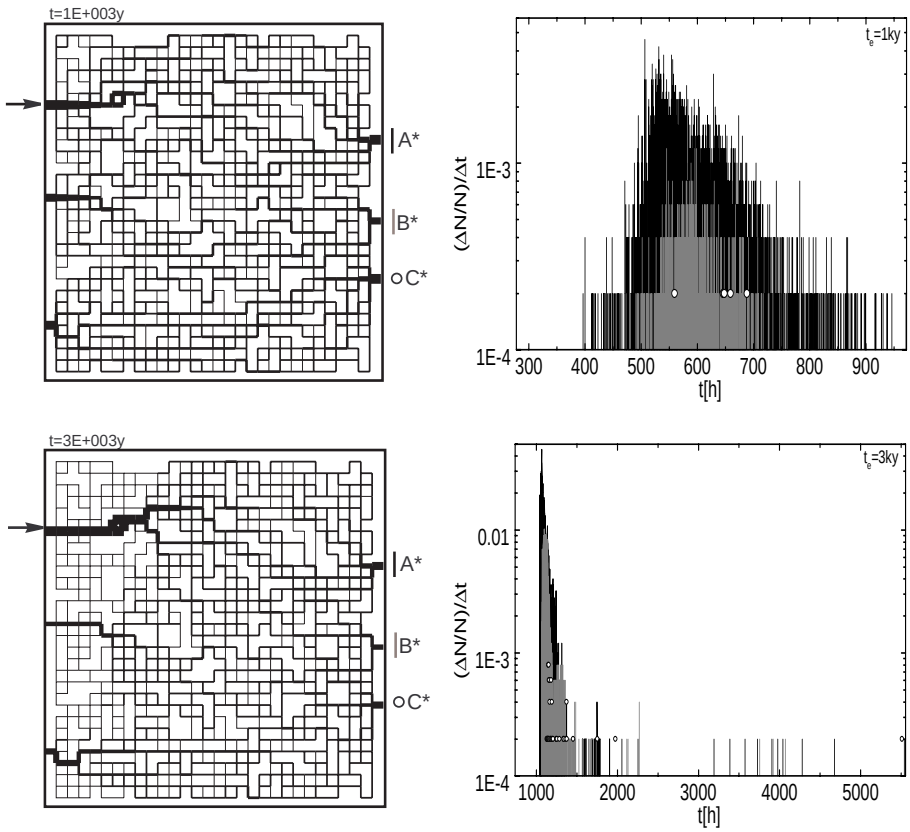

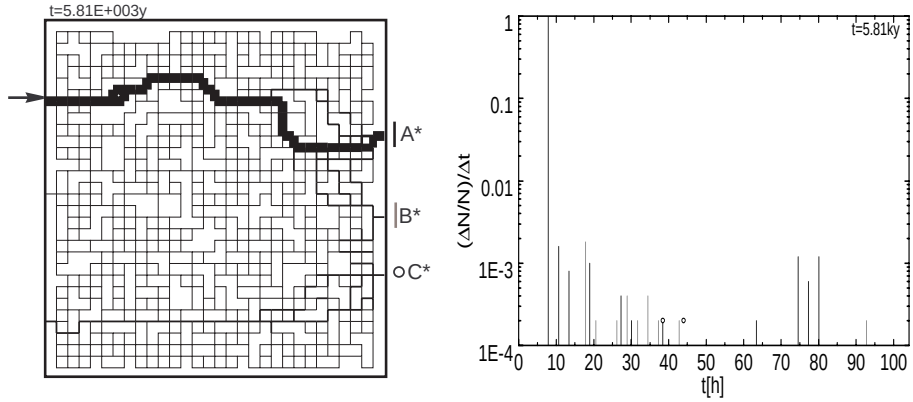

c)

Figure 6.1: Particle tracking on a 2D percolation network at various stages of its evolution. On left hand side is the flow distribution in the network presented in units Q/Q_{max} where Q_{max} corresponds to the fracture with the highest flow rate. Arrow on figure a denote the input point for the "dye". The evolution of this net is discussed in Sec.4.1 and presented on Figs.4.3-4.6. The graphs on the righ hand side represent the distribution of particles as they arrive to the outputs A* (black lines), B* (gray lines) and C*(open circles). Note the logarithm scale for the number of particles.

its pathway. The residence time in the net for a particle also depends on its pathway and is given by

$$T_n(in \rightarrow out) = \sum_i t_i = \sum_i L(i)\bar{A}(i)/Q(i), \tag{6.2}$$

where t_i is the transit time for the fracture i, defined by the length of the fracture $L(i)$, its average cross-section $\bar{A}(i)$ and flow rate. The sum over i goes along all the fractures which belong to the pathway. At each output a certain distribution of particle arrivals $\Delta N/\Delta t$ is recorded.

Fig.6.1 shows the flow distribution in the network at three stages of its evolution (as in Fig.4.4). Graphs on the right show the time distribution of particles at the outputs for the network at this stages. Arrivals at output A* are denoted by black lines, arrivals at B* by gray lines and arrivals to C* by open circles.

At 1ky the flow is quite evenly distributed, therefore particles take many pathways of comparable probability. The first particles arrive at the outputs after 400h, the peak of arrivals is between 500 and 600h and the last particles arrive after 1000h. At 3ky the flow on the lefthand side concentrates to the winning pathway but remains quite evenly distributed on the righthand side. Distribution of particles at the outputs is more cumulative, since most of the particles take the most probable - winning - pathway on the lefthand side, but are spread to different pathways after the flow becomes more evenly distributed. At breakthrough more than 99% of the particles are travelling along the winning pathway AA*. Therefore they have the same resident time.

The net can be considered as a linear filter and results presented by the graphs on Fig.6.1 as its kernel functions. A response to any input function $f(t)$ can be obtained by convolving the kernel function and the function $f(t)$.

Even a simple case like the one presented gives a complex "tracing" results. Further work on more complex model is required, so that the results could be compared with the one obtained in nature. An question arises whether the tracing results could be used to estimate the state of maturity of karst aquifer.

6.3 NEED FOR COOPERATION

Future work demands a close cooperation between modellers, field hydrologists and speleologists. The latter can provide realistic geologic scenarios to the modellers who can transform these into results which help to understand processes in karst systems.

An extremely important job for the future is further investigation of dissolution rates in karst environments. As shown, the parameters of the rate equation play a crucial role in the evolution of karst aquifers. Data on dissolution rates are limited with respect to temperature and p_{CO_2} and also with respect to the presence of foreign ions and other aggressive agents. Further knowledge on dissolution kinetics for other karst rocks is also required - recent laboratory experiments on gypsum reveal non-linear dissolution rates also for this mineral giving a new view on karst evolution in gypsum areas.

A THE TRACING OF CONCENTRATION IN 2D NETWORKS

In Chap.4 the numerical procedure for the calculation of 2D networks was briefly discussed. Here we present an important technical detail. We discuss how the Ca^{2+} concentration and, when required, also the CO_2 concentration is traced in 2D models presented in this work.

To calculate the widening of each fracture at any timestep, the concentration of Ca^{2+} at its input node is required. Suppose that a fracture is draining the water from the node i. If complete mixing is assumed, the concentration at the node is given by

$$c_i = \frac{\sum_j Q_j c_j^{out}}{\sum_j Q_j}. \tag{A.1}$$

Q_j is the flow rate of the fracture carrying the water to the node i and c_j^{out} its concentration at the exit. As we see, the exit concentrations of all the fractures draining the water into the node is required, before widening of the fractures leading from the node starts. Therefore it is important to chose the right sequence of calculation. In the models presented here the following procedure was used:

1. Order all the nodes according to their hydraulic heads.
2. Start at the nodes with the highest hydraulic head. These are at the input boundary of the net where the concentration is given as an input parameter.
   - Search for the fractures which drain the solution from these nodes.
   - Do the transport-dissolution procedure (widening) on these fractures.
3. Go to the node which follows in the head sequence.
   - Search for the fractures which drain the solution into the node and those leading the solution from the node. Fractures leading into the node have all been widened in step 1, so their output concentrations are known.

- Calculate the concentration at the node using Eq.A.1.
- Widen all the fractures leading from the node.

4. Continue down the head sequence to the next node.
   - The same procedure and the same reasoning as in step 2 is valid also for this node and all the nodes which follow in the head sequence.
5. Terminate the procedure when the nodes with the lowest hydraulic heads at the output boundary are reached.

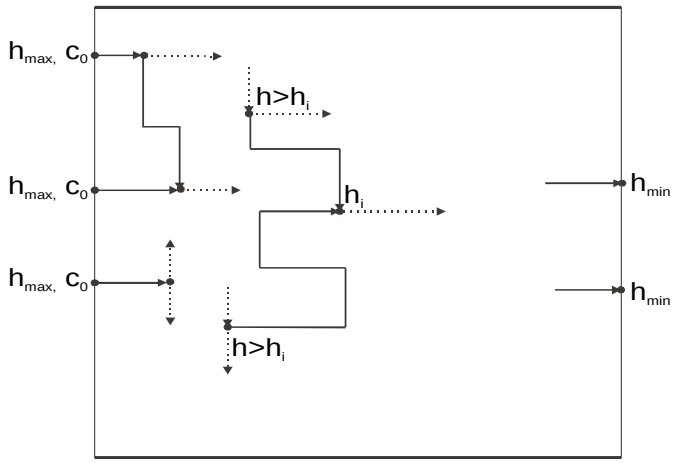

Figure A.1: A schematic presentation of a 2D net with few nodes and fractures connecting them. Widening sequence follows the sequence of the hydraulic heads at the nodes. In this way the concentration at each node is defined at the time when the widening of the fractures leading from it starts.

Bibliography

J. Bear. *Hydraulics of groundwater*. McGraw-Hill, New York, 1979.

J. Bear and A. Verruijt. *Modeling groundwater flow and pollution*. D.Reidel publishing company, Dodrecht, 1987.

W. J. Beek and K. M. K. Mutzall. *Transport Phenomena*. Wiley, New York, 1975.

R. Bird et al. *Transport phenomena*. Wiley, New York, 1960.

A. Bögli. Mischungskorrosion: Ein beitrag zum verkarstungsproblem. *Erdkunde*, 18: 83–92, 1964.

A. Bögli. *Karst hydrology and physical speleology*. Springer, Berlin, Heidelberg, New York, 1980.

D. Buhmann and W. Dreybrodt. The kinetics of calcite dissolution and precipitation in geologically relevant situations of karst areas: 1. open system. *Chemical Geology*, 48: 189–211, 1985a.

D. Buhmann and W. Dreybrodt. The kinetics of calcite dissolution and precipitation in geologically relevant situations of karst areas: 2. closed system. *Chemical Geology*, 53: 109–124, 1985b.

T. Clemens et al. A combined continuum and discrete network reactive transport model for the simulation of karst development. In *Calibration and reliability in groundwater modeling*, volume 237, pages 309–318. IAHS, 1997a.

T. Clemens et al. Modelling the genesis of karst aquifer systems using a couple reactive network model. In *Hard rock geosciences*, volume 241, pages 3–10. IAHS, 1997b.

T. Clemens et al. Simulation of the development of karst aquifers: The role of epikarst. *Int. Journal of Earth Sciences*, 88:157–162, 1999.

W. Dreybrodt. Mixing corrosion in $CaCO_3 - CO_2 - H_2O$ systems and its role in karstification of limestone areas. *Chemical Geology*, 32:221–236, 1981a.

W. Dreybrodt. *Processes in karst systems-Physics, Chemistry and Geology*. Springer, Berlin, New York, Heidelberg, 1988.

W. Dreybrodt. The role of dissolution kinetics in the development of karstification in limestone: A model simulation of karst evolution. *Journal of Geology*, 98:639–655, 1990.

W. Dreybrodt. Principles of early development of karst conduits under natural and man-made conditions revealde by mathematical analysis of numerical models. *Water Resources Research*, 32(9):2923–2935, 1996.

W. Dreybrodt. Limestone dissolution rate in karst environments. In *Proc.12th Int. Congress of Speleology: Modelling in karst systems*, volume 2, pages 45–52. IUS, Swiss Speleological Society, 1997.

W. Dreybrodt. The eqilibrium chemistry of karst water in limestone terranes. In A. Klimchouk, D. Ford, A. Palmer, and W. Dreybrodt, editors, *Speleogenesis: Evolution of karst aquifers*. Nat. Speleol. Soc., 2000.

W. Dreybrodt and L. Eisenlohr. Limestone dissolution rates in karst environments. In A. Klimchouk, D. Ford, A. Palmer, and W. Dreybrodt, editors, *Speleogenesis: Evolution of karst aquifers*. Nat. Speleol. Soc., 2000.

W. Dreybrodt and F. Gabrovšek. Dynamics of the evolution of a single karst conduit. In A. Klimchouk, D. Ford, A. Palmer, and W. Dreybrodt, editors, *Speleogenesis: Evolution of karst aquifers*. Nat. Speleol. Soc., 2000.

W. Dreybrodt, J. Lauckner, Z. Liu, U. Svensson, and D. Buhmann. The kinetics of reaction $CO_2 + H_2O \rightarrow H^+ + HCO_3^-$ as one of the limiting step for the dissolution of calcite in the system $H_2O - CO_2 - CaCO_3$. *Geochimica et Cosmochimica Acta*, 60: 3375–3381, 1996.

W. Dreybrodt and J. Siemers. Cave evolution on two-dimensional networks of primary fractures in limestone. In A. Klimchouk, D. Ford, A. Palmer, and W. Dreybrodt, editors, *Speleogenesis: Evolution of karst aquifers*. Nat. Speleol. Soc., 2000.

L. Eisenlohr, B. Madry, and W. Dreybrodt. Changes in the dissolution kinetics of limestone by intrinsic inhibitors adsorbing to the surface. In *Proc.12th Int. Congress of Speleology*, volume 2, pages 81–84. IUS, Swiss Speleological Society, 1997.

O. Erga and S. Terjesen. Kinetics of the heterogenous reaxtion of calcium bicarbonate formation, with special reference to copper inhibition. *Acta Chem Scand*, 10:872–875, 1956.

R. Ewers. *Cavern development in the dimension of length and breadth*. PhD thesis, Mcmaster University, 1982.

D. Ford. Perspectives in karst hydrogeology and cavern genesis. In A. Palmer, M. Palmer, and I. Sasovsky, editors, *Karst modeling*, pages 17–29. Karst Waters Institute, 1999.

D. Ford and R. Ewers. The development of limestone caves in the dimensions of length and depth. *Can. J. Earth Sci.*, 15:1783–1798, 1978.

D. Ford and P. Williams. *Karst geomorphology and hydrology*. Unwin Hyman, London, England, 1989.

R. Freeze and H. Cherry. *Groundwater*. Prentice-Hall, Englewood Cliff, 1979.

F. Gabrovšek and W. Dreybrodt. The role of mixing corrosion in calcite aggressive $H_2O-CO_2-CaCO_3$ solutions in the early evolution of karst aquifers. *Water Resources Research*, In print, 1999b.

S. Ge. A governing equation for fluid flow in rough fractures. *Water resources Research*, 33:53–61, 1997.

C. Groves and A. Howard. Minimum hydrochemical conditions allowing limestone cave development. *Water Resources Research*, 30:607–615, 1994a.

C. Groves and A. Howard. Early development of karst systems. 1. preferential flow path enlargement under laminar flow. *Water Resources Research*, 30:2837–2846, 1994b.

T. Halihan, J. Sharp, and R. Mace. Interpreting flow using permeability at multiple scales. In A. Palmer, M. Palmer, and I. Sasovsky, editors, *Karst modeling*, pages 82–95. Karst Waters Institute, 1999.

B. Hanna and H. Rajaram. Influence of aperture variability on dissolutional growth of fissures in karst formations. *Water Resources Research*, 34:2843–2853, 1998.

A. Howard and C. Groves. Early development of karst systems 2. turbulent flow. *Water Resources Research*, 31:19–26, 1995.

C. L. Hull and K. N. Koslow. Streamline routing through fractures junctions. *Water Resources Research*, 22:1731–1734, 1986.

P.-Y. Jeannin, F. Zwahlen, and N. Doefliger. From a conceptual model of karst hydrological systems to water -vulnerability mapping. In A. Palmer, M. Palmer, and I. Sasovsky, editors, *Karst modeling*, pages 65–69. Karst Waters Institute, 1999.

A. Jeschke, K. Vosbeck, and W. Dreybrodt. *Personal communication*, 2000.

G. Kaufmann and J. Braun. Karst aquifer evolution in fractured, porous rocks. *Water Resources Research (in print)*, 1999a.

G. Kaufmann and J. Braun. Karst aquifer evolution in fractured rocks. *Water Resources Research (in print)*, 1999b.

E. L., K. Meteva, F. Gabrovšek, and W. Dreybrodt. The inhibiting action of intrinsic impurities in natural calcium carbonate minerals to their dissolution kinetics in aqueous $H_2O - CO_2$ solutions. *Geochimica et Cosmochimica Acta*, 63:989–1002, 1999.

S. Lauritzen, O. N., and J. Petersen. Modeling the evolution of channel networks in carbonate rocks. In J. Hudson, editor, *ISRM Symposium: Eurock'92*, pages 57–62. Thomas Telford, 1992.

C.-H. Lee and I. Farmer. *Fluid flow in discontinuous rocks*. Chapman & Hall, London, Glasgow, 1993.

D. Lowe and J. Gunn. Carbonate speleogenesis: an inception horizon hypothesis. *Acta Carsologica*, 38:757–788, 1997.

B. Menne. Carbonatolyse und biokonservierung als mechanism der verkarstung und speleogenese. *Beiträge zur Gydrogeologie*, 49, 1998.

L. Moreno et al. Flow and tracer transport in a single fracture: A stochastic model and its relation to some field observation. *Water Resources Research*, 24(12):2044–2048, 1988.

L. Moreno and C. Tsang. Multiple peak response to tracer tests in single fractures: A numerical study. *Water Resources Research*, 27(8):2143–2150, 1991.

I. Motyka and Z. Wilk. Hydraulic structure of karst-fissured triasic rocks in the vicinity of olkusz (poland). *Kras Speleologia*, 14(5):11–24, 1984.

A. N. Palmer. Recent trends in karst geomorphology. *J. Geol. Educ*, 32:247–253, 1984.

A. N. Palmer. Solutional enlargement of opening in the vicinity of hydraulic structures in karst regions. In *2nd Conference on Environmental Problems in Karst Terranes and Their Solutions*. Assoc. of Groundwater Sci. and ENg., 1988.

A. N. Palmer. The origin and morphology of limestone caves. *Geol. Soc. of America Bull.*, 103:1–21, 1991.

J. R. Philip. The fluid mechanics of fracture and other junctions. *Water Resources Research*, 24:239–246, 1988.

L. Plummer, T. Wigley, and D. Parkhurst. The dissolution of calcite in CO_2-water systems at 5^oC to 60^oC and 0.0 to 1.0atm CO_2. *American journal of science*, 278: 179–216, 1978.

R. Rhoades and M. Sinacori. The pattern of ground-water flow and solution. *Journal of Geology*, 49:785–794, 1941.

J. Siemers. *Simulation von Karst-Aquiferen*. PhD thesis, Universität Bremen, 1998.

J. Siemers and W. Dreybrodt. Early development of karst aquifers on percolation networks of fractures in limestone. *Water resources research*, 34:409–419, 1998.

D. Staufer. *Introduction to percolation theory*. Taylor and Francis Ltd., London, Philadelphia, 1960.

D. Stewart and Z. Leyk. *Meschach: Matric computation in C*. Centre for Mathematics and it application, ANU, Cannberra, Australia, 1994.

U. Svensson and W. Dreybrodt. Dissolution kinetics of natural calcite minerals in CO_2 -water systems approaching calcite equilibrium. *Chemical Geology*, 100:129–145, 1992.

A. Swinnerton. Origin of limestone caverns. *Geological Society of America Bulletin*, 34: 662–693, 1932.

Y. Tsang and C. Tsang. Flow channeling in a single fracture as a two dimensional strongly heterogenous permeable medium. *Water Resources Research*, 25(9):2076–2080, 1989.

P. Weyl. The solution kinetics of calcite. *Journal of Geology*, 66:163–176, 1958.

W. White. Role of solution kinetics in the development of karst aquifers. In J. Tolson and F. Doyle, editors, *Karst hydrogeology*. UAH, 1977.

W. White and J. Longyear. Some limitations on speleogenetic speculation imposed by hydraulics of groundwater flow in limestone. *Nittany Grotto Newl.*, 10:155–167, 1992.

Z. Wilk, I. Motyka, and I. Jozefko. Investigations of aome hydraulic properties of karst solution openings and fractures. *Ann.Soc. Geologorum Poloniae Rocznik Polskiegotowarystwa Geologicznego*, 43(1/2):15–43, 1984.

S. Worthington. A comprehensive strategy for understanding flow in carbonate aquifers. In A. Palmer, M. Palmer, and I. Sasovsky, editors, *Karst modeling*, pages 30–37. Karst Waters Institute, 1999.

List of piblications

Parts of this work have been published or submitted to the following publications:

1. Dreybrodt, W. and Gabrovšek, F., Dynamics of the evolution of a single karst conduit. In Klimchouk, A., Ford, D.C., Palmer, A.N., and Dreybrodt W., editors, *Speleogenesis: Evolution of karst aquifers.* Nat. Speleol. Soc.,2000.

2. Dreybrodt, W. and Gabrovšek, F., Influence of fracture roughness on karstification times. In Klimchouk, A., Ford, D.C., Palmer, A.N., and Dreybrodt W., editors, *Speleogenesis: Evolution of karst aquifers.* Nat. Speleol. Soc.,2000.

3. Gabrovšek, F. and Dreybrodt, W., A model of early evolution of karst conduits affected by subterranean CO_2 sources. *Environmental Geology*, 39: 531-543,2000.

4. Gabrovšek, F. and Dreybrodt, W., The role of mixing corrosion in calcite aggressive $H_2O - CO_2 - CaCO_3$ solutions in the early evolution of karst aquifers. *Water Resources Research*, 36:1179-1189,2000.

5. Gabrovšek, F. and Dreybrodt, W., A comprehensive model of the early evolution of karst aquifers in limestone in the dimension of length and depth. *Accepted for publication in Journal Of Hydrology* .

6. Eisenlohr L., Meteva, K., Gabrovšek, F., Dreybrodt, W., The inhibiting action of intrinsic impurities in natural calcium carbonate minerals to their dissolution kinetics in aqueous $H_2O - CO_2$ solutions. *Geochimica et Cosmochimica Acta*, 63:989-1002,1999.

Presentations at the scientific meetings:

1. *Enhancement of early karstification by subterranean sources of carbon dioxide.* Poster presentation at the symposium **Karst Modeling**, Charlotesville, USA, February 1999.

2. *Subterranean sources of CO_2 accelerate early karstification.* Oral presentation at the symposium **Karst 99**, Mende, France, September 1999.

Abstract

Basic processes governing the early evolution of karst aquifers are discussed by use of numerical models based on field observations on properties of karst aquifers. Basically three different models are presented and discussed: a single fracture, a two-dimensional fracture network and a model of a vertical cross-section of a limestone plateau.

The time-scale of early karst evolution is discussed by a model of a single fracture in limestone under constant head conditions. The flow and dissolution rates are coupled by a feed-back mechanism which leads to breakthrough, an abrupt increase of widening in a short time span. The breakthrough time is taken as a measure of intensity of subsurface karstification. Assuming an even widening of the fracture by the dissolution rates at its exit, an analytical approximation for the breakthrough time is given which defines all basic parameters governing the karstification. The approximation and the numerical models give the same dependence of breakthrough time on these basic parameters. It is shown that the breakthrough time is inversely proportional to the dissolution rates at the bottleneck, the point, where the dissolution rates are minimal.

Few scenarios where the geochemical conditions in the fracture vary are presented. Change of the kinetic order at the lithology boundary or change of the equilibrium concentration due to the CO_2 inputs affect the breakthrough time considerably. The magnitude of these changes and their position in the fracture determine the change of the breakthrough time.

A junction of two fractures joining into a third one is presented to discuss the effect of mixing corrosion on early karstification. Different chemical compositions of the solutions at the confluence trigger mixing corrosion and accelerate karstification. Mixing corrosion is most active if the flow rates through both affluent fractures are comparable and solutions at the junction are close to equilibrium. This is particularly valid at the very early stage of conduit development. Mixing corrosion reduces the breakthrough time up to a few times.

The models of two-dimensional fracture networks give additional information on the spatial development of karst conduits. Siemers and Dreybrodt Siemers and Dreybrodt (1998); Siemers (1998) showed that the breakthrough times in 2D percolation networks show essentially the same dependence on the basic parameters as in a single fracture. A system of competing conduits connecting inputs and outputs evolves. The evolution is most progressive along the pathways which exhibit the shortest breakthrough times.

Similar geochemical scenarios as for the single fracture are discussed also

for the 2D networks. The discussion is focused on the pattern development. Mixing corrosion arising from the different p_{CO_2} at the inputs, induces the growth of isolated conduits in the mixing zones. This conduits cause the redistribution of hydraulic heads and initiate the formation of new preferential pathways. Similar effects are observed in the models where the sources of CO_2 are introduced into the network.

A model of a vertical cross-section of a limestone massif is presented to discuss karst evolution in the dimensions of length and depth. The initial aquifer consists of a network with evenly spaced fine fissures ($\approx 50\mu m$ aperture widths). A constant recharge (450mm/y) is applied to the to the plateau on the top. The aquifer is unconfined, thus a water-table dividing the vadose and the phreatic zone is present. Most of the flow and highest dissolution rates are located close to the the water-table. Due to the increasing permeability in the water table drops leaving a region of highly permeable vadose zone behind. Once the water-table reaches the base level, a conduit start propagate from the spring into the aquifer. Additionally a simple pathway or a percolation network of prominent fractures (several $100\mu m$) can be added. Feed-back mechanism is active along the conduits growing along these fractures, but becomes suppressed due to the dropping water-table. If constant head conditions are also present, the breakthrough occurs either along the highly permeable zone close to the water-table or along the prominent fractures. The results of the various models are discussed also from the view of speleogenetic theories derived from field observation.

Povzetek

Voda v kraškem vodonosniku topi matično kamnino. Posledica tega so specifične lastnosti kraških vodonosnikov, kot so velika nehomogenost, različni režimi pretakanja vode itd. Izraz "razvoj kraških vodonosnikov" označuje razvoj sekundarne poroznosti v vodonosniku zaradi korozijskega širjenja razpok. V okvir tega štejemo tudi speleogenezo oziroma razvoj jam.

Pričujoče delo skuša na osnovi numeričnih modelov odgovoriti na vprašanje: **Kateri mehanizmi oblikujejo kraški vodonosnik in kateri parametri določajo časovni in prostorski razvoj kraških kanalov ?**

Delo obravnava zgolj zgodnjo fazo razvoja vodonosnika, do vzpostavitve turbulentnih tokov. Zastavljeno je v smislu od enostavnega h kompleksnemu. Prvi del obravnava korozijski razvoj enostavne razpoke oziroma kraškega kanala, drugi del razvoj dvodimenzionalne razpoklinske mreže, v tretjem delu pa je predstavljen model vertikalnega razvoja odprtega vodonosnika. Vsak od teh modelov z določenega vidika odgovarja na zgoraj zastavljeno vprašanje. Ta povzetek zajema nekatere ključne rezultate, ki so predstavljeni v delu.

- **Razvoj enostavne razpoke: enodimenzionalni model:** Izraz "enostavna razpoka" (angl. single fracture) označuje eno samo razpoko oziroma zaporedje razpok, ki prevajajo isti tok. Rezultate modela razvoja enostavne razpoke lahko strnemo v naslednjih nekaj točk:

  - Ob konstantnem hidravličnem potencialu med pritočno in odtočno točko, pretok s časom narašča zaradi korozijskega širjenja razpoke. Pretok in hitrost reakcije vzdolž razpoke sta preko ohranitvenih zakonov povezana tako, da rast pretoka povzroči rast hitrosti reakcije in obratno. Pretok skozi razpoko pospešeno narašča do preboja (angl. breakthrough), ko v kratkem času naraste za nekaj redov velikosti. Preboj označuje konec začetne faze speleogeneze. Po preboju in vzpostavitvi turbulentnega toka kanal raste enakomerno po vsej dolžini. Prebojni čas, čas od začetka razvoja do preboja, lahko vzamemo kot merilo za intenziteto speleogeneze v določenih pogojih.
  - Prebojni čas je potenčna funkcije osnovnih kemičnih in fizikalnih parametrov, ki določajo pretok in reakcijsko hitrost v razpoki ob začetku razvoja in je obratno sorazmeren s hitrostjo raztapljanja pri iztočni točki ob začetku širjenja razpoke.
  - Analitična obravnava razvoja razpoke je relativno enostavna ob predpostavki, da je širjenje enakomerno, določeno s hitrostjo reakcije ob

iztočni točki. Analitični približek za prebojni čas se funkcijsko ujema z numeričnimi rezultati.

– Kemični parametri vzdolž razpoke se lahko spremenijo zaradi različnih vzrokov. Kot primera sta navedena spremembe litologije in izvori CO_2 v freatični coni. Te spremembe, četudi relativno majhne, močno vplivajo na prebojni čas. Sprememba prebojnega časa je odvisna od relativne spremembe parametrov in položaja spremembe v razpoki. Analitična obravnava je podobna kot pri osnovnem modelu; prebojni čas je obratno sorazmeren z začetno hitrostjo reakcije v grlu - točki, kjer se razpoka širi najpočasneje .

- **Pomen mešalne korozije v zgodnji speleogenezi:** Mešalna korozija je posledica nelinearnosti ravnotežne krivulje med Ca^{2+} in CO_2. Do mešalne korozije pride ob mešanju vod z različnimi ravnotežnimi koncentracijami. Danes je splošno sprejeto dejstvo, da mešalna korozija ne igra ključne vloge v speleogenezi, saj je nelinearna kinetika raztapljanja apnenca zadostna za razvoj dolgih kraških kanalov. Prisotnost mešalne korozije pa lahko močno vpliva na prostorski in časovni razvoj razpok. Kot primer vpliva mešalne korozije na zgodnjo speleogenezo je prikazan model stika dveh dotočnih in ene odtočne razpoke. Dinamika razvoja takega sistema je ob prisotnosti mešalne korozije precej bolj kompleksna, prebojni čas pa se skrajša tudi več kot za polovico.

- **Razvoja dvodimenzionalne razpoklinske mreže:** Dvodimenzionalna razpoklinska mreža je nadgradnja modela enostavne razpoke. Osnova predstavljenega modela je pravokotna mreža, v kateri so razpoke statistično razporejene med mrežnimi točkami. Tako mrežo imenujemo perkolacijska mreža. Razvoj mreže določajo geometrični parametri razpok, geokemični parametri, prostorska razporeditev razpok ter razporeditev pritočnih in odtočnih točk. Razvoj poteka vzdolž različnih poti, ki povezujejo pritočno in odtočno stran. Če je začetna širina vseh razpok enaka in če se geokemični parametri v mreži ne spreminjajo, se prvi preboj dogodi vzdolž najkrajše poti. Razvoj je s časovnega vidika podoben razvoju enostavne razpoke. Sprememba geokemičnih parametrov v mreži (litologija, izvori CO_2, mešalna korozija) lahko močno vpliva na prostorski vzorec razvitih razpok. Bolj ko je pritočna voda nasičena, bolj enakomeren je razvoj mreže. Mešalna korozija v razpoklinski mreži povzroči rast izoliranih kanalov v območju mešanja vod z različno ravnotežno koncentracijo c_{eq}. S časom vse več vode v mreži izvira iz dotokov z višjo c_{eq}, zato se območja mešanja krčijo in rast izoliranih kanalov zamre. Kljub temu pa ti kanali močno vplivajo na razvoj mreže in na razporeditev kanalov ob preboju.

- **Vertikalni razvoj odprtega vodonosnika** Model temelji na vertikalni mreži pribl. $50\mu m$ širokih razpok. V modelu je pomembna prisotnost vodnega nivoja oziroma freatične površine (v tem primeru gre za krivuljo).

Ta predstavlja mejo med freatično (nasičeno, prežeto) in vadozno (nenasičeno, neprežeto) cono. Predpostavljen je konstanten dotok vode v mrežo na površini. Voda skozi vadozno cono na vodnem nivoju vstopa v freatično cono.

V freatični coni je voda najagresivnejša ob vodnem nivoju, kjer je širjenje razpok najhitrejše. To povzroči, da velik del vode odteče skozi dobro prepustni pas vzdolž vodnega nivoja. Vodni nivo s časom pada zaradi naraščanja hidravlične prepustnosti v freatični coni. Za seboj pušča pas vadozne cone z do nekaj redov velikosti večjo hidravlično prepustnostjo, kot jo ima vodonosnik ob začetku zakrasevanja. Ko se vodni nivo spusti do nivoja erozijske baze, tam tudi ostane. Pri tem raste kanal vzdolž nivoja erozijske baze, od izvira v notranjost vodonosnika.

Raztapljanja v vadozni coni model ne upošteva. Predpostavlja pa, da je voda ob vstopu v freatično cono nasičena glede na dolžino poti v vadozni coni, torej glede na višino vodnega nivoja na mestu vstopa v freatično cono.

Če je poleg konstantnega dotoka na robu še konstantni potencial, pride do preboja vzdolž vodnega nivoja ko ta doseže območje konstantnega potenciala. V enakomerno mrežo lahko deterministično ali statistično vključimo sistem glavnih (prominentnih) razpok z večjo začetno odprtino (npr. $200 - 400\mu m$). Ob konstantnem potencialu na robu lahko prvi preboj poteka vzdolž glavnih razpok, ob vodnem nivoju ali pa je prebojna pot kombinacije obeh.

Tudi ko na robu ni konstantnega potenciala, glavne razpoke v zgodnji fazi rastejo pospešeno zaradi povratne zanke. Padec vodnega nivoja in s tem potencialne razlike vzdolž razpok, v predstavljenih modelih še pred prebojem zaduši povratno zanko. Po padcu nivoja do erozijske baze, se lahko glavnina toka pretaka pod tem nivojem, preko zank, ki jih tvorijo razširjene glavne razpoke.

Rezultati modela se v veliki meri ujemajo z znanimi konceptualnimi modeli zgodnje speleogeneze.

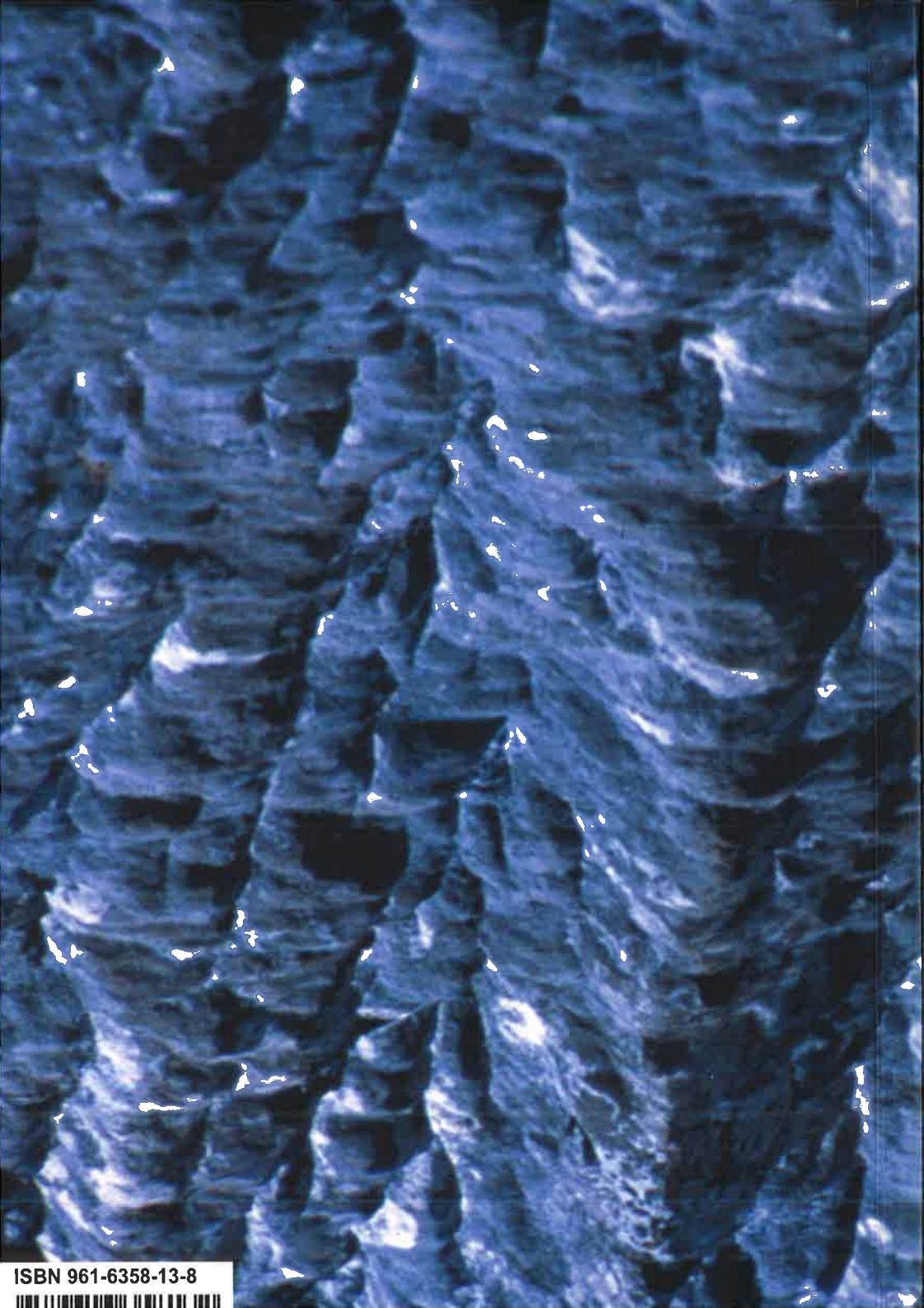

ISBN 961-6358-13-8